This is to certify that the
dissertation entitled

COHERENT CONTROL AND ITS APPLICATIONS IN MOLECULAR RECOGNITION

presented by

JOHANNA MARIE GALLARDO DELA CRUZ

has been accepted towards fulfillment
of the requirements for the

Ph.D. degree in Chemistry

Major Professor's Signature

July 12, 2006

Date

COHERENT CONTROL AND ITS APPLICATIONS IN MOLECULAR RECOGNITION

By

Johanna Marie Gallardo Dela Cruz

A DISSERTATION

Submitted to
Michigan State University
in partial fulfillment of the requirements
for the degree of

DOCTOR OF PHILOSOPHY

Department of Chemistry

2006

ABSTRACT

COHERENT CONTROL AND ITS APPLICATIONS
IN MOLECULAR RECOGNITION

By

Johanna Marie Gallardo Dela Cruz

The fundamental design of this dissertation involves the use of the laser as a tool to recognize molecules. The work presented here has relevance to a variety of fields, including nonlinear optics and spectroscopy, coherent control of laser-matter interactions, biomedical imaging and analytical chemistry. My work involves a series of experiments utilizing a femtosecond laser system and an instrument known as a pulse shaper. It entails new applications of coherent laser control, where tailoring the shape of laser pulses by phase modulation causes changes in the impact of the excitation field on different processes such as multiphoton excitation and photoionization.

The application of coherent control methods to biomedical imaging hinges on the possibility that phase-modulated femtosecond laser pulses can propagate through biological tissue. The approach used in this dissertation corrects spectral phase distortions introduced by imaging optics, maintains laser pulse optimization throughout the experiment and initiates phase manipulation in order to gain selectivity that is analogous to that which can be achieved by tuning a longer laser pulse. This capability is used to demonstrate functional imaging by selective two-photon excitation. Furthermore, phase modulation is exploited as a means to curtail the damaging effects of multiphoton excitation in biomedical applications, thus increasing the prospect for cellular and molecular identification, including cancer detection.

The use of phase modulation of femtosecond laser pulses is also shown here as a means to recognize isomeric molecules based on their ionization and fragmentation patterns. The selectivity that is attainable with shaped pulse technology is coupled with the inherent sensitivity of mass spectrometry to not only distinguish between isomers, but to quantify them in isomeric mixtures. Although chemical identification is carried out quite efficiently with standard mass spectrometry, the dilemma involving the identification of isomeric compounds is addressed here by laser control. The environmental, pharmaceutical and analytical chemistry fields could stand to benefit from this "customized" mass spectrometry approach. Additionally, the concept of utilizing chiral femtosecond pulses as a tool for enantiomeric resolution is introduced.

ACKNOWLEDGMENTS

I am indebted to my advisor, Prof. Marcos Dantus, who has given me so much guidance, insight and encouragement throughout this work. I am grateful to the members of my committee, Profs. Gary Blanchard, James McCusker, and Greg Swain, who offered me their time, advice and support. My colleagues in our research group have also been of great assistance during my research. I thank the following past and present members of the Dantus group: Dr. Vadim Lozovoy, Dr. Igor Pastirk, Dr. Matthew Comstock, Dr. Tissa Gunaratne, Bingwei Xu, Michael Kangas, and Jess Gunn. Many thanks to Trish Miller who has taken time to read my drafts and make comments. Thanks to the College of Natural Sciences for awarding me a Dissertation Completion Fellowship, providing me with the financial means to complete this project. My heartfelt appreciation to the Department of Chemistry for supporting me as a teaching/research assistant so that I could complete my graduate studies. Finally, I would like to thank my husband and my children who have endured this long process with me, always offering support, patience and confidence.

TABLE OF CONTENTS

LIST OF TABLES

LIST OF FIGURES

KEY TO ACRONYMS/ABBREVIATIONS

BME	α-methyl-benzenemethanol
BP	Binary phase
BPS	Binary phase shaping
CD	Circular dichroism
CPA	Chirped pulse amplification
CPL	Circularly polarized light
CW	Continuous wave
DI	Dissociation followed by ionization
EI	Electron ionization
FROG	Frequency resolved optical gating
FWHM	Full width at half maximum
GA	Genetic algorithm
GC	Gas chromatography
GVD	Group velocity dispersion
HPTS	8-hydroxypyrene-1,3,6-trisulfonic acid trisodium salt
ID	Ionization followed by dissociation
IMS/MS	Ion mobility spectrometry/mass spectrometry
IR	Infrared
KLM	Kerr lens mode locking
LC/MS	Liquid chromatography/mass spectrometry
LCPL	left circularly polarized light
LIF	Laser induced fluorescence
LPL	Linearly polarized light
LQ	Liquid crystal
m/z	Mass to charge ratio
MCP	Multichannel or microchannel plate
MII	Multiphoton intrapulse interference
MIIPS	Multiphoton intrapulse interference phase scan
MP	4-methyl-2-pentene
MRI	Magnetic resonance imaging
MS	Mass spectrometry
NA	Numerical aperture
Nd:YLF	Neodymium: yttrium lithium fluoride
$Nd:YVO_4$	Neodymium: yttrium vanadate
NIST	National Institute of Standards and Technology
ORD	Optical rotatory dispersion
PDT	Photodynamic therapy
PMMA	Polymethylmethacrylate
QWP	Quarter waveplate
RCPL	Right circularly polarized light
SHG	Second harmonic generation
SLM	Spatial light modulator

SPIDER	Spectral interferometry for direct electric field reconstruction
TOF	Time of flight
Ti:S	Titanium:sapphire
TL	Transform-limited
TMP	Turbomolecular pump
UV	Ultraviolet

INTRODUCTION

When this research project was conceived, the idea of teaching lasers to produce photons that are smart enough to recognize molecules seemed implausible. The full potential of lasers had barely been realized and questions as to whether the utility of lasers could be expanded from sheer spectroscopic tools to photonic tools for probing molecules had yet to be answered. Since the first caveman learned to control fire, researchers have shaped and used laser light in a constantly expanding array of technologies. Yet "smart lasers" could do much more. This dissertation focuses on our quest to transform the cutting-edge science of ultrafast laser technology into a versatile tool that can be used by the biomedical research community on the one hand, and, on the other hand, open up possibilities for applications in real-time chemical sensing and detection that will benefit a wide range of disciplines. It is our hope that smart lasers will find a niche not only in the research laboratory but in the real world. The key to these aspirations is molecular recognition by coherent laser control.

While in the past, lasers had mainly been used to investigate given physical systems, currently scientists are exploiting the coherent properties of lasers to manipulate or control matter. The field of coherent control explores the ability of a coherent laser source to manipulate the dynamics at various stages of a process. Its rapid development has been stimulated by the objectives of selective bond breaking and formation. The first concepts for controlling chemical reactions in the time domain with ultrashort laser pulses were developed theoretically by Tannor, Rice and Kosloff[1, 2] and realized experimentally by Gerber[3] and Zewail.[4] However, the applications of coherent control are by no means limited to controlling chemical reactions. This research explores coherent

control as a tool for the selective recognition of molecular components, which could provide benefits in the biomedical and analytical chemistry fields.

Ultrafast laser technology involves the use of femtosecond (1 fs=10^{-15} seconds) lasers to study the properties of matter. The extremely short pulse duration allows one to create, detect and study short-lived chemical reaction intermediates and transition states. For the analytical chemist, femtosecond lasers can be used to monitor transient chemical species in solution or in the gas phase, to image living cells with sub-micrometer resolution, for laser ablation, and micromachining applications.

Ultrafast pulses consist of a broad range of phase-locked frequency components. They can be represented as a coherent superposition of several monochromatic light waves within a range of frequencies that is inversely proportional to the duration of the pulse. The ultrashort time duration of ultrafast pulses results in a very broad spectrum; this allows one to access a wide range of different frequencies. Possibilities for manipulating ultrafast coherent broadband sources in addition to technological developments in ultrafast lasers have just begun to unleash the potential of the exciting field of ultrafast pulse shaping.

Pulse shaping involves either the simultaneous or exclusive control of the amplitude and phase of different frequency components in the spectrum of a femtosecond laser pulse. This has led to a surge of activity in coherent control. The time–bandwidth profile, in conjunction with the phase characteristics of the pulse, is commonly referred to as pulse shape. Many of the frequencies constituting the ultrafast pulse can simultaneously excite many coherent transitions to the excited states, and the capability to manipulate them with shaped pulses leads to interesting results. In 1984, Warren

suggested a theoretical application of shaped pulses in the time domain for nonlinear optical applications such as population transfer.[5] The role of the spectrum of the shaped pulse was found to be indispensable in the choice of the optimal temporal shape that would influence whether or not population transfer occurs. Warren tested his proposal experimentally in 1987[6] using phase and amplitude shaped nanosecond (100-200 ns) laser pulses to control I_2 fluorescence . A year after this, Weiner, Nelson and co-workers investigated the effect of pulse shaping on impulsive stimulated Raman scattering with the objective of mode-selective vibrational amplification in an alpha-perylene molecular crystal.[7, 8] Following this breakthrough, Broers et. al. introduced binary amplitude modulation to demonstrate spectral focusing of second harmonic generation (SHG) and two-photon absorption of Rydberg states in Rubidium.[9, 10] In 1992, Judson and Rabitz suggested the use of learning algorithms to optimize the phase and amplitude of femtosecond pulses to control optical processes.[11] Computer feedback algorithms based on genetic or evolutionary strategy techniques have made it possible for an experiment itself to select an optimal optical waveform to enhance a particular process. This was experimentally implemented in 1997,[12] and since then, the use of feedback optimized genetic algorithms (GA) has gained a tremendous following from several research groups,[13-31] while paving the way towards a number of valuable applications.[32-58] In 1998, Meshulach and Silberberg demonstrated that femtosecond laser pulses can be tailored to control two-photon absorption in cesium.[59] They soon after showed that the effect of shaped pulses in exciting sharp transitions in small molecules was absent when large molecules in solution are involved.[60] In 1999, variations in chirp conditions of the laser pulses were applied to control the fluorescence yield of molecules in different micro-

environments.[61] Silberberg and co-workers[62, 63] later demonstrated the constructive or destructive nature of interferences between resonant and nonresonant contributions in two-photon excitation. They revealed that amplitude control and phase modulation with step-functions could amplify two-photon fluorescence from Rb atoms several times. Leone and co-workers used feedback and evolutionary algorithms with a phase shaper to optimize the interference between resonant and nonresonant contributions to multiphoton excitation of Li_2.[64] Motivated by the work of Silberberg, the Dantus group began its pursuit of the laser pulse requirements for controlling multiphoton excitation of large organic molecules in solution. This effort subsequently resulted in the development of a new approach to coherent control[65, 66] which had a direct influence on the experiments covered in this dissertation.

By appropriately controlling the arrival time of different frequency components of an ultrashort excitation pulse, one can readily control ground state and excited state dynamics, or cause chemically selective molecular excitation or ionization, without having to resort to wavelength tuning by tweaking the laser, using filters or moving optics. The creation of tailored pulses and their use in attempts to control atomic and molecular events is an innovative research area. Recent successes in molecular control have resurged hopes towards bond-selective chemistry. As pulse-shaping technology matures further, it will open up exciting new applications in areas as diverse as biomedical research (imaging, diagnostics and therapeutics) and quantum computation. Furthermore, computer technology has advanced at a pace that allows us to take full advantage of progress in optical technology.

In the following chapters, the essential principles (Chapter 1) that governed this research and the major experimental tools (Chapter 2) that were crucial to the success of the experiments will be presented. Chapters 3 and 4 discuss the experimental demonstration of selective two-photon excitation as a tool for the identification of molecules based on their chemical environment. The last two chapters discuss the analytical implementation of coherent control in qualitative and quantitative molecular identification of geometric and structural isomers (Chapter 5) and of optical isomers (Chapter 6), including the setbacks encountered when exploring enantiomeric resolution with chiral laser pulses. These impediments, however, do not necessarily suggest the impossibility of enantiomeric discrimination by chiral pulses. This is just the beginning of converting this seemingly unattainable dream into reality.

The only way of discovering the limits of the possible is to venture a little way past them into the impossible."

- Arthur C. Clarke's Second Law

CHAPTER 1

PRINCIPLES

When considering laser control of large molecules, the large numbers of degrees of freedom where energy can flow imply that the control field must be complex enough to track the evolution of the wave packet in a multidimensional potential. The complexity arises because different frequencies are required to interact with a sample at specifically coordinated times. Based on this representation, coherent laser control of large molecules seems extremely difficult. However, the Gerber group showed the capability of certain shaped pulses obtained from learning algorithms for inducing selective photochemistry in isolated molecules.[32, 53] Gerber and Motzkus have published adaptive control experiments on large molecules in condensed phase.[45, 51] They have both argued that the molecules are under coherent control during the pulse, which in both cases extends for a couple of picoseconds. These results contradict the measurement of electronic coherence time by the group of Shank, where it was determined that the electronic coherence time in large molecules in solution decays within the first 70 fs.[67] The experiments of Shank were carried out using the photon echo method, which cancelled the contributions from inhomogeneous broadening. If inhomogeneous dephasing is taken into account, as it should for a single pulse experiment, then dephasing occurs faster than 10 fs. This would imply that the mechanism involved discounts coherent control of the intramolecular dynamics of the sample molecule.

In the condensed phase, both homogeneous and inhomogeneous broadening, which affect both the clarity and location of absorption lines, make it virtually impossible

to consider excitation of a specific vibronic transition. Such processes preclude the creation of pulses that can address a specific vibronic transition in all the molecules in the bulk sample. Consequently, the perception of coherent control of molecules in the condensed phase calls for a new paradigm.

1.1 Multiphoton Intrapulse Interference (MII)

The MII approach of coherent control is based on the delivery of small packets of energy to molecules by means of an ultrafast laser pulse. Its main advantage lies in its ability to control the order of a transition (two-photon, three-photon or higher) while maintaining a constant and intense photon flux. Controlling excitation consequently allows control over the details of how molecules interact with light pulses.

The underlying concept of the MII method is shown in Figure 1.1. Multiphoton transitions are optimized when the central bandwidth of the laser pulse, ω_0, is some proportion (1/2 for two-photon, 1/3 for three-photon, etc.) of the total energy of the transition. The large bandwidth of ultrashort pulses permits interference between the different frequency components.[9] The phase of each of the frequencies within the bandwidth determines how photons combine to achieve multiphoton excitation. Figure 1.1 shows the spectrum of an ultrashort pulse, with amplitude plotted as a function of detuning from the central frequency. A phase mask, $\phi(\Omega)$, can be imprinted on the pulse such that the phase of each frequency component, Ω, acquires a specific value. MII requires phase functions that are comparable to the homogeneously broadened absorption spectrum and the spectral width of the pulse.[65] The phase function depicted here is defined by the following equation,

$$\phi(\Omega) = \alpha \cos(\gamma\Omega - \delta) \qquad 1.1$$

to consider excitation of a specific vibronic transition. Such processes preclude the creation of pulses that can address a specific vibronic transition in all the molecules in the bulk sample. Consequently, the perception of coherent control of molecules in the condensed phase calls for a new paradigm.

1.1 Multiphoton Intrapulse Interference (MII)

The MII approach of coherent control is based on the delivery of small packets of energy to molecules by means of an ultrafast laser pulse. Its main advantage lies in its ability to control the order of a transition (two-photon, three-photon or higher) while maintaining a constant and intense photon flux. Controlling excitation consequently allows control over the details of how molecules interact with light pulses.

The underlying concept of the MII method is shown in Figure 1.1. Multiphoton transitions are optimized when the central bandwidth of the laser pulse, ω_0, is some proportion (1/2 for two-photon, 1/3 for three-photon, etc.) of the total energy of the transition. The large bandwidth of ultrashort pulses permits interference between the different frequency components.[9] The phase of each of the frequencies within the bandwidth determines how photons combine to achieve multiphoton excitation. Figure 1.1 shows the spectrum of an ultrashort pulse, with amplitude plotted as a function of detuning from the central frequency. A phase mask, $\phi(\Omega)$, can be imprinted on the pulse such that the phase of each frequency component, Ω, acquires a specific value. MII requires phase functions that are comparable to the homogeneously broadened absorption spectrum and the spectral width of the pulse.[65] The phase function depicted here is defined by the following equation,

$$\phi(\Omega) = \alpha \cos(\gamma\Omega - \delta) \qquad 1.1$$

where α refers to the phase amplitude, γ is the modulation in the frequency domain ($2\pi N/(\Omega\max-\Omega\min)$, with period N) and δ is the position of the phase mask with respect to the center of the spectrum of the laser pulse.

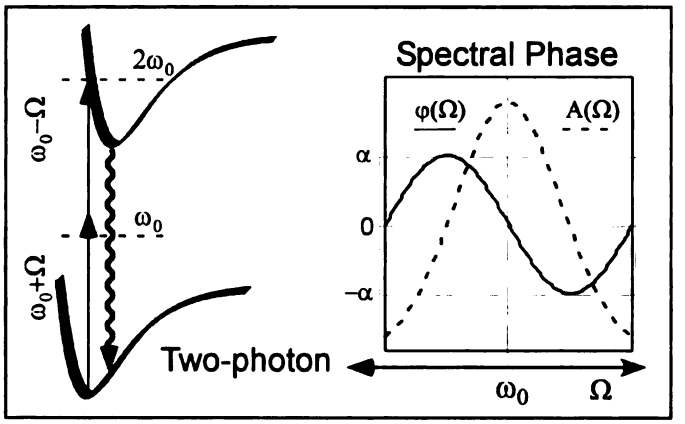

Figure 1.1. MII concept for two-photon transitions.

MII was inspired by the work of Silberberg[59] who demonstrated control of two-photon excitation of a sharp atomic transition using initially a step function, and then a sinusoidal phase function. Figure 1.2 shows how the fundamental spectrum of a pulse in the frequency domain is unaffected when a given spectral phase function is used. On the contrary, the phase changes the pulse in the time domain and may significantly affect the frequency-doubled spectrum. The addition of a linear phase function across the bandwidth of the pulse in the frequency domain results only in the delay in time of the pulse and has no effect on its nonlinear interaction with the molecules. A quadratic phase modulation (Figure 1.2B) advances or delays the pulse in time, but leads to broadening. The frequency-doubled spectrum is basically unaffected, except for a substantial decrease in intensity. Consequently, a correspondingly reduced cross-section to nonlinear

processes is expected. Large changes in the nonlinear excitation processes are expected to occur when odd-order phase functions such as cubic (Figure 1.2C) and higher components are used.[66] A simple sinusoidal phase function (Figure 1.2A) focuses the energy in a narrower spectral region. The wavelength where the frequency-doubled spectrum is maximized can be controlled by shifting the sine function.

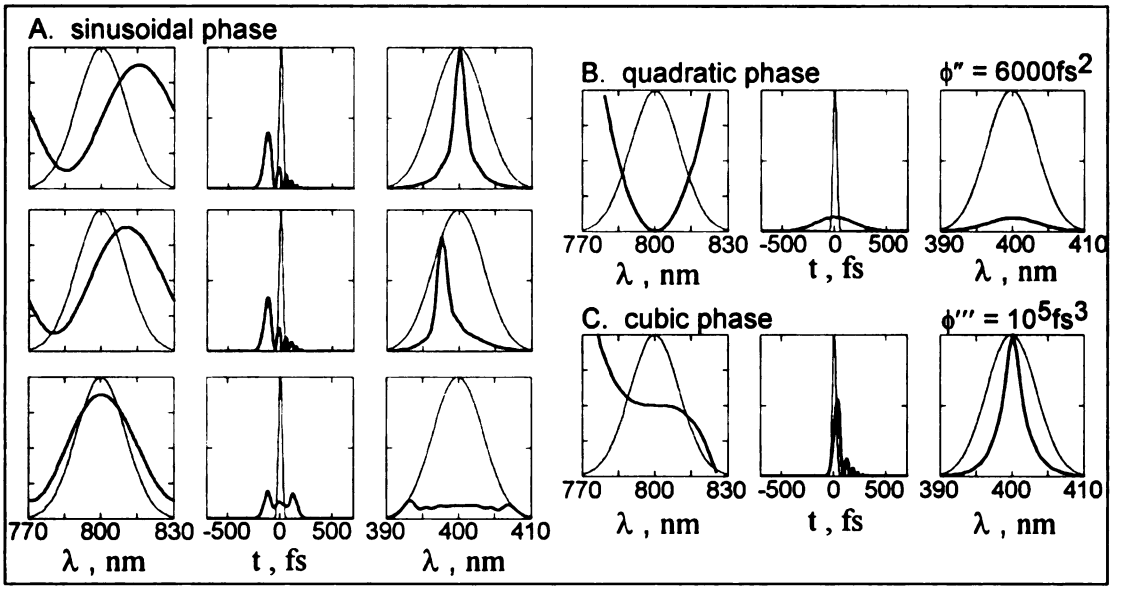

Figure 1.2. Calculated time and frequency domain representation of shaped pulses using sinusoidal (A), quadratic (B) and cubic (C) phase functions. The introduction of spectral phase modulation causes the amplitude in the frequency-doubled spectrum of the pulse (with frequencies near $2\omega_0$) to change. The first column under each phase shows the spectrum of the pulse and the spectral phase modulation that is introduced by the pulse shaper. The second column shows the time dependent electric field. The third column depicts the effects of phase modulation on the frequency-doubled spectrum of the laser.

To illustrate how MII takes place, consider a two-photon process such as SHG. Assuming that the fundamental pulse is centered at frequency ω_0, maximum SHG then takes place at $2\omega_0$. Silberberg[59] first realized that the intensity of SHG at $2\omega_0$ not only depended on the intensity of the ultrashort laser pulse at ω_0, but more importantly on the entire bandwidth of the pulse. He further observed that the relative phase between the

blue-shifted frequencies ($\omega_0 - \Omega$) and the red-shifted frequencies ($\omega_0 + \Omega$) determined the intensity at $2\omega_0$ according to

$$I_{SHG}(2\omega_0) \propto \int_{-\infty}^{\infty} E(\omega_0 + \Omega)E(\omega_0 - \Omega)\exp[i\{\phi(\omega_0 + \Omega) + (\omega_0 - \Omega)\}]d\Omega \qquad 1.2$$

In this expression, the interference terms in the brackets imply that there can be constructive interference when the sum of the phases is zero, or destructive interference when the sum of the phases is π. Even functions lead to a decrease in signal while odd functions increase signal intensity at $2\omega_0$. This has led to the formulation of an equation that could be used to calculate the *n*th order transition probability to a frequency that is detuned from the central wavelength of the laser pulse by an amount Δ. The expression:

$$S_n \propto \int_{-\infty}^{\infty} g^{(n)}(\Delta)\left|A^{(n)}(\Delta)\right|^2 d\Delta, \qquad 1.3$$

correlates the *n*th-order spectral amplitude of the laser pulse $A^{(n)}$ with the *n*th-order absorption spectrum of the system, $g^{(n)}(\Delta)$. With these equations as basis, the effect of phase modulation from all multiphoton transitions, not only at $n\omega_0$, but through the entire bandwidth of the pulse $n(\omega_0+\Delta)$, can be calculated. This in turn allowed the application of MII to multiphoton transitions of large organic molecules, including proteins, in the condensed phase.[65, 66] The first order spectrum of the field (one-photon excitation) is not affected by the phase function because of the absence of an interference term at this order. The introduction of phase functions has been shown to achieve much more than simple attenuation of the laser peak intensity. The *n*th order spectrum (*n*-photon transitions) can be tuned to specific resonances, and phase can be used to attenuate third-order processes.[66]

Through MII, modest phase modulation can be used to manipulate nonlinear transitions. This capability can initiate the development of techniques that would enable shaped femtosecond lasers to selectively excite molecular reactions and alter the course of biological processes. Accordingly, coherent control through MII can be employed as an initial step towards molecular identification.

1.2 Pulse Characterization and Compensation

Ultrashort pulse laser technology has advanced remarkably over the past two decades, expanding its niche in the research community from home-built sub-picosecond dye systems to contemporary commercial turn-key sub-50 fs amplified systems to the generation of exceedingly short pulses. Most researches have concentrated on pulses in the visible or near infrared (IR) part of the light spectrum. At these wavelengths, an optical wave takes about 3 fs to complete one oscillation, so that state-of-the-art 5-fs laser pulses correspond to less than two optical cycles. Optical pulses much shorter than this require substantial effort to produce, and since light propagates as an oscillating electromagnetic wave, they are fundamentally limited to the single-cycle duration (time taken for the propagating optical wave to complete one full oscillation) of about 3 fs. Huge advances in the generation and manipulation of ultrashort laser pulses have also led to the generation of pulses with attosecond time resolution,[68-70] where pulses are in the UV/XUV spectral range, and are orders of magnitude weaker and spectrally much broader than femtosecond pulses. These types of pulses, however, are beyond the scope of this discussion.

Femtosecond pulsed lasers have provided unprecedented insights into molecular processes such as reaction dynamics. In the last several years, femtosecond lasers (~50-100 fs) have been indispensable tools in scientific and development laboratories, including several industrial, communication, and medical applications. Consequently, a whole new set of more stringent requirements and constraints for the everyday use of ultrashort laser sources needs to be addressed.

The characteristics and quality of ultrashort pulses play a crucial role in the fields or processes they are used for or applied to. As the pulses get shorter, however, they become more prone to spectral phase distortions that take place in the process of their generation and their subsequent delivery to the target. Every interaction of an ultrashort pulse with an optical surface such as a dielectric mirror, lens, optical fiber, or microscope objective leads to spectral phase distortions. These distortions will consequently lead to increased pulse duration, loss of peak intensity and, in some cases, loss of information. Shorter pulses suffer more significant distortions as a consequence of group velocity dispersion (GVD, see Appendix A), whereby different frequency components of the short pulse travel at different speeds, causing the pulse to eventually fall apart. For this reason, the characterization and correction of these spectral phase distortions, especially at the location where the laser meets the sample, are extremely important. These distortions, which are either intentional or caused by experimental imperfections, are generally addressed on a case-to-case basis. Careful characterization of the laser pulse's temporal profile, bandwidth, intensity, and spectral and temporal phase are essential for successful application. Due to the uncertainty principle, the time-bandwidth product is a natural limit and has persistently been an ultimate goal in many applications. The pulses that are

at or very close this limit are referred to as transform-limited (TL), which means that they are shortest for a given bandwidth. The atomic and molecular processes initiated and driven by TL pulses can be relatively easily simulated and understood.

Traditional ways of basic pulse characterization involve measurement of a pulse's bandwidth and time profile by means of intensity autocorrelation, where a pulse is split and measured against itself by nonlinear interaction. The corresponding spectral phase of the pulse, unfortunately, stays undetermined using these methods. Current established spectral phase measurement methods include frequency resolved optical gating (FROG)[71, 72] and spectral phase interferometry for direct electric filed reconstruction (SPIDER)[73, 74]. These methods, including their variants, depend upon the measurement of autocorrelations or cross-correlations between two pulses to characterize the spectral phase of a pulse. In FROG, the frequency and time-resolved signals are used to retrieve spectral phase. SPIDER requires that the laser pulse be split into two beams that are then upconverted by a heavily chirped pulse. The interference of the upconverted pulses in the frequency domain is used to reconstruct the spectral phase in the original pulse. These methods have been implemented for more than a decade, but they suffer from either complex or demanding set-ups (SPIDER) or cumbersome and approximate phase-retrieving algorithms (FROG) that prevent them from being used without the aid of a laser expert. The first attempts to achieve TL pulses based on feedback dependent on spectral phase used a GA-controlled shaper for adaptive compression.[15, 16, 19, 23, 25, 26, 28, 30, 75] Others implemented time-domain interferometry with an acousto-optic programmable filter.[76] These indirect methods are limited by the lack of sensitivity of the total nonlinear

optical signals to phase deformations outside the full width at half maximum (FWHM) of the pulse.

The use of fully characterized ultrashort pulses in the experimental setting should not be disregarded. In this research, the multiphoton intrapulse interference phase scan (MIIPS) method is used for pulse characterization and compensation of spectral phase distortions. This technique combines spectral phase characterization and pulse shaping in one simple set-up. MIIPS takes advantage of the influence that phase modulation has on the probability of nonlinear optical processes at specific frequencies.[65, 66] It is a single beam method that does not require beam splitters, interferometry, autocorrelation or global maximization. The spectral phase across the pulse can be obtained analytically with this method. Within a few minutes, the pulses are characterized and compensated to yield TL or user-specified shaped pulses at the sample. This capability is extremely practical and can be incorporated in any laser setup. Consequently, this method has proven to be extremely powerful for the accurate and reproducible demonstration of the experiments discussed in this work - selective microenvironment probing, multiphoton microscopy, functional imaging and discrimination between isomeric compounds - using ultrashort shaped pulses.

The principle of the measurement involves comparing an unknown phase against a calibrated phase. The active component of the MIIPS system is a computer-controlled spatial light modulator (SLM) located at the Fourier plane of a pulse compressor. The computer introduces a reference phase function and records changes in the frequency-doubled spectrum of the pulses. To make a precise and accurate measurement of the spectral phase using MIIPS, the known phase requires an accurately calibrated pulse

shaper. The pulse shaper essentially behaves as two back-to-back spectrometers. The pulse is dispersed with a prism or grating and collimated with a cylindrical mirror. At the Fourier plane, where all the frequencies are isolated, their phases are manipulated by a computer-controlled liquid crystal (LQ)-SLM. The SLM applies the reference phase function to the input pulse, and the resulting pulse is then reconstituted to the time domain by a second cylindrical mirror and prism/grating. The SLM has a 250-ms response time. The output beam is analyzed by placing a 0.01-mm-thick beta barium borate SHG crystal in its path, usually at the place where optimum pulses are required. For each reference phase function that is introduced by the computer-controlled SLM, the output spectrum from the SHG is dispersed in a spectrometer and recorded. The reference phase function is programmed into the SLM and scanned for different values of δ ranging from 0 to 4π. For each value of δ, the spectrum of the frequency-doubled pulse changes, achieving a maximum in the spectral region over which the SLM compensates for the phase distortions.

The MIIPS data consist of a two dimensional collection of SHG spectra as a function of δ(as shown in Figure 1.3). For TL pulses, the data show equally spaced parallel linear features. Deviations from these parallel lines indicate distortions in the spectral phase. The spacing between the lines indicates the degree of quadratic phase distortions. The slope that the maximum SHG features makes in the λ–δ plane determines the cubic phase modulation.

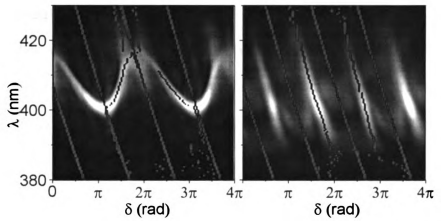

Figure 1.3. Characterization (left) and compensation (right) of spectral phase modulation in femtosecond pulses using the MIIPS method. MIIPS-generated traces (wavelength, λ, as a function of δ) show changes in the SHG spectrum of the laser. As a general rule, quadratic phase distortions are determined from differences in the distances between the four SHG features in the MIIPS scans. Cubic phase distortions are determined by differences between the slopes of these SHG features. Computer analysis of the trace retrieves the spectral phase of the input pulse. After a few iterations of characterization and compensation, the output pulses are TL as evidenced by the parallel, equidistant features in the MIIPS data (right). Notice that after compensation, large differences in the distances and slopes of uncompensated pulses are greatly diminished.

Once the MIIPS system has characterized the pulse and retrieved the phase distortions inherent to the pulses, it can use this information to drive the SLM such that it compensates for the distortions. The first step in compensation is to take the phase determined from the first scan and program it into the SLM with a negative sign so that it subtracts the distortions. The system then carries out a new phase scan to determine the remaining spectral phase modulation (usually about 10% of the original). A few such iterations will typically eventually yield TL pulses.

1.3 Phase Modulation

Complete control over multiphoton transitions entails reaching the maximum limited by TL pulses at some interesting frequencies and suppressing effects at different unwanted frequencies, as illustrated in Figure 1.4. The realization of this task lies in the accurate manipulation of either the phase or amplitude of a laser pulse.

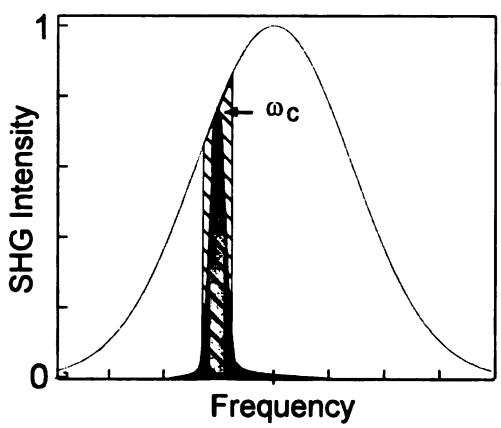

Figure 1.4. Cartoon representation of the goal of phase modulation. The broad bandwidth frequency-doubled spectrum from TL pulses is represented by a Gaussian (thin line). The objective is to introduce phase modulation to cause the two-photon spectrum to be intense only inside the window defined by frequency 2ωc, and to minimize all other regions of the spectrum outside the window.

Amplitude modulation only affects multiphoton transitions by decreasing pulse energy and consequently decreasing multiphoton effects (see Figure 1.5). In effect, control over which frequencies should be maximized or minimized is basically nonexistent. For a spectral width that is about 10% of the available bandwidth, amplitude restriction produces 100 times less second harmonic intensity than TL pulses.[77] Although the suppression of a large range of frequencies is possible, the low intensity obtained at the desired wavelength makes this control route experimentally unpractical. Conversely, phase modulation does not change the overall energy of the pulse. Interference between

fields with different phases, which can be constructive or destructive, allows targeted regions of the second harmonic spectrum to either be maximized or minimized, as was shown in Figure 1.2. Finding the specific phase modulation of a fundamental pulse to control the amplitude of the multiphoton spectrum is crucial for MII control experiments.

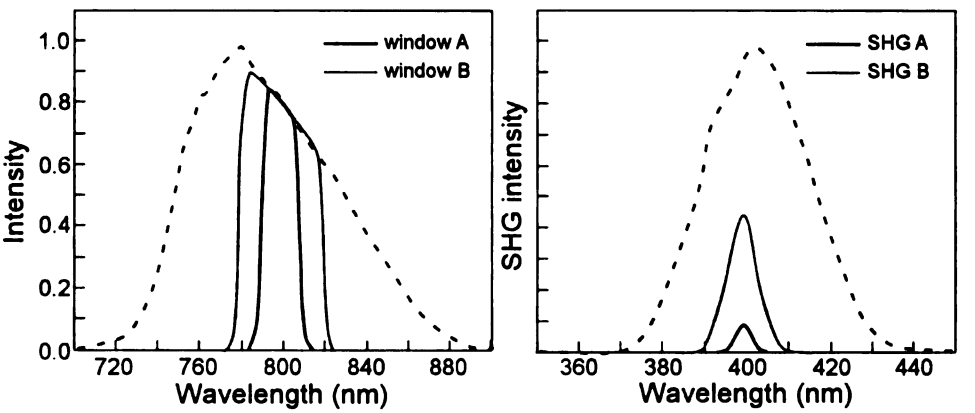

Figure. 1.5. Effect of spectral amplitude restriction on SHG. Left: Experimental spectrum of the laser before (dotted lines) and after filtering with windows of width 20 nm (window A) and 40 nm (window B). Right: Experimental SHG of TL (dotted lines) and spectrally filtered pulses, A and B, as indicated in the right panel.

The question on which pulse shape among numerous alternatives is optimal to produce a desired outcome is also a matter of concern. The number of different pulse shapes that can be generated with a 128-pixel phase-only pulse shaper scales as the number of phase values P that a pixel can introduce raised to the number N of pixels (P^N). If coarse phase steps are taken and the number of phases is reduced to 100, the search space would be of size 10^{256}. This is an infinitely large search space, compared to the number of atoms in the universe (~10^{81} atoms), which, in all respects, is quite a huge number. One of the challenges of pulse shaping technology has been to figure out how to effectively explore such a vast search space. Although the efficiency of computer

learning algorithms, such as GAs, in exploring large spaces for the most favorable pulse shape is highly regarded, the practicability of this approach in the laboratory setting needs to be considered. Since the number of experiments that can be carried out with a femtosecond laser is usually limited to less than 1000 per second, only a small fraction (~3.6 million pulses) of the huge search space can be tested in an hour. Only in very special cases or with great luck could one find the optimum pulse shape among the hundreds of orders of magnitude of alternatives.

A recent study by Rabitz affirms that the continuous control of both the phase and amplitude of all frequencies within the bandwidth of a pulse by a GA leads to several excellent, but no intermediate solutions.[78] This entails a markedly large search space that cannot be sampled experimentally. Consequently, all experimental endeavors require some strategy to reduce the search space by limiting the phases to a specific function (for example, sinusoidal or polynomial). These approaches have been quite successful but setting drastic limitations on the search space may not always prove to be valuable. Other groups have reduced the number of pixels by binning contiguous pixels[32, 37] although the possibility that much better solutions may have been missed by such a reduction in the search space is an issue that one needs to be aware of. Efficient search space reduction is presently one of the most important goals in shaped pulse coherent control.

Initial MII experiments from the Dantus group involved the use of a simple sinusoidal function because it offered the ability to create desired regions of constructive and destructive intrapulse interference with a minimum number of control parameters[65] (see Figure 1.2). The realization that the most important parameter involves controlling the relative phase between the frequencies that combine to achieve the excitation

consequently led to the generation of binary phase (BP) functions with 0 or π phase retardation[77] (see Equation 1.2). The implication of this realization in terms of search space reduction allows one to use many more active pixels. In addition, the redundancy of phases that are allowed to take on arbitrary values is eliminated. Phase modulation with BP functions is exploited in this research to initiate selective responses from different molecules as a means for identification. Chapters 3 to 5 involve experimental applications of phase modulation. Chapter 6 involves a variation of phase modulation, whereby binary functions are used to control the degree and direction of polarization of a laser pulse. Polarization shaping with femtosecond laser pulses, which is explored as a prospective scheme for chiral recognition, will be discussed in greater detail in the final chapter of this work.

CHAPTER 2

EXPERIMENTAL TOOLS

The experiments covered by this dissertation were carried out on two different laser systems. The first system was a Titanium:sapphire (Ti:S) oscillator system (Kapteyn-Murnane Labs) pumped by a neodymium: yttrium lithium fluoride or Nd:YLF laser (Spectra Physics: Millenia), capable of producing 10 fs pulses tunable from 780 nm to 840 nm at 87 MHz repetition rate. The pulse energy from this oscillator is ideally suited for liquid phase experiments and for biological imaging. This system was the primary laser source for the experiments in Chapters 3 and 4.

The second was a regeneratively amplified Ti:S laser system. The output from a continuous wave (cw) neodymium: yttrium vanadate or Nd:YVO_4 laser (Spectra Physics: Millenia) pumps a femtosecond Ti:S oscillator (Kapteyn-Murnane Labs), capable of producing ~15 fs pulses at 80 MHz. This output is amplified by a regenerative amplifier (Spectra Physics: Spitfire) pumped by a 1 KHz Nd:YLF laser (Spectra Physics: Evolution X). The amplified pulses centered at 800 nm have a maximum energy of 0.8 mJ/pulse and time duration ranging from 35-50 fs. The high photon flux in this system was essential for the ionization experiments carried out in Chapters 5 and 6.

Each of these laser systems was interfaced with a 128-pixel double mask pulse shaper. In each of the following chapters, the laser system and pulse-shaping apparatus used will be re-introduced in the experimental section.

2.1 Femtosecond Laser

2.1.1 Ti:S Laser Oscillator System

The generation of ultrashort pulses implies the amplification of a broad frequency spectrum. A new era in the solid state laser field was born with the characterization of a laser material based on the titanium doped sapphire crystal, Ti:Al_2O_3.[79] Shortly after the characterization of the optical parameters, the successful cw lasing action in this material was demonstrated.[80] The broad gain bandwidth, large energy storage density, and excellent thermal properties of the Ti:S crystal make it an excellent material for femtosecond laser and amplification systems. Ti:S has an energy level diagram (see Figure 2.1), which is typical for solid laser materials (four-level lasers). The bandwidth over which this laser can be obtained is wide enough to allow for 3-fs long pulses. The absorption band has its peak at around 500 nm and the emission spectrum is peaked around 800 nm. Since the absorption and emission bands are well separated, losses due to reabsorption of the laser radiation are minimized.

Two conditions determine the frequency components available to build up a wide frequency spectrum. The first is the approximately resonance condition for a standing wave: $n\lambda/2=L$, where L is the length of the cavity. The second is the spectral bandwidth of the laser, which is mainly limited by the gain profile of the amplifying medium.

In a cavity consisting only of a gain medium, end mirror and output coupling mirror, all modes are oscillating in random phase. By introducing additional components in the cavity, it is possible to phase-lock these modes to each other. The generation of ultrashort laser pulses implies that all the frequency modes should have a well-defined

phase relation with respect to each other. In this sense, the concept and implementation of mode-locking techniques in laser sources has been crucial.[81]

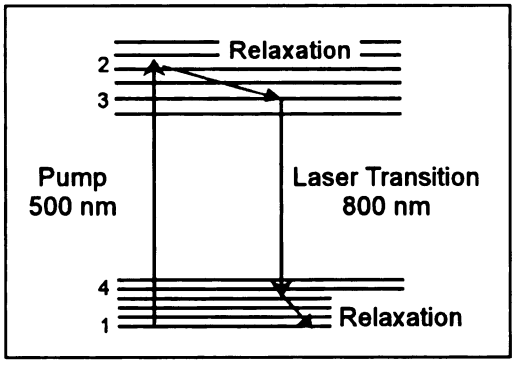

Figure 2.1. Four-level scheme of a typical solid-state laser. The photons are first excited to a state higher in energy than the upper laser state. They then quickly decay down by relaxation or radiationless decay into the upper laser state. It is important for the pumped state to have a short lifetime for spontaneous emission compared to the upper laser state. The upper laser state should have as long a lifetime (for spontaneous emission) as possible, so that the photons live long enough to be stimulated and thus contribute to the gain. The fourth step involves depopulation of the lower laser level by a fast decay (relaxation) process. This greatly decreases the loss of laser photons by stimulated absorption processes since the photons in the lower laser level have a short lifetime for spontaneous emission.

When the phase difference between the modes is constant, the modes are oscillating in phase and interfere constructively. If we add the electric fields from the standing modes, the sum as a function of time will be a short pulse propagating back and forth in the cavity.

At low intensities, the refractive index for a given wavelength is constant. At high intensities (I), the refractive index varies by $n = n_1+n_2I$. Due to the fact that the laser has a spatial intensity variation, the refractive index will be larger in the center of the beam, where the intensity is the highest. This makes the crystal behave like a lens (referred to as a Kerr lens). A major breakthrough in the femtosecond laser field was established by

Sibbett et al. in 1991, with the discovery of the action of self-mode-locking.[82] Also referred to as Kerr-lens mode-locking (KLM), the method relies on the non-linear refractive index properties (n_2) of the Ti:S crystal. The self-focusing action in the crystal in combination with an intracavity aperture results in intensity dependent losses and causes the mode-locking of the laser. This is shown in Figure 2.2. It is common that Kerr lensing in the amplifying medium is used to obtain both gain and mode-locking.

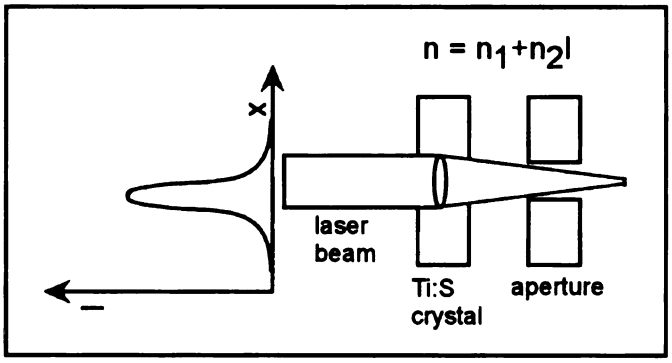

Figure 2.2. The spatial profile of the laser beam creates the "Kerr lens".

Implementation of the KLM scheme and accurate control over GVD allow the generation of short femtosecond pulses. These features are characteristic of the Ti:S laser oscillator system used in the first half of this thesis, shown in Figure 2.3.

Pulse durations in prism-controlled Ti:S oscillators are limited to 10 fs, as a result of the inherent presence of uncompensated higher order dispersion terms used. With the introduction of KLM lasers, the design of an oscillator that generates femtosecond optical pulses has reached a stage of remarkable simplicity and robustness. The ability of the Ti:S solid-state oscillator to generate 10 fs pulses[83, 84] as well as its excellent reliability,

makes it an attractive ultrafast light source in the laboratory. Not surprisingly, the class of lasers based on Ti:S has rapidly gained ground in the field of ultrafast spectroscopy.

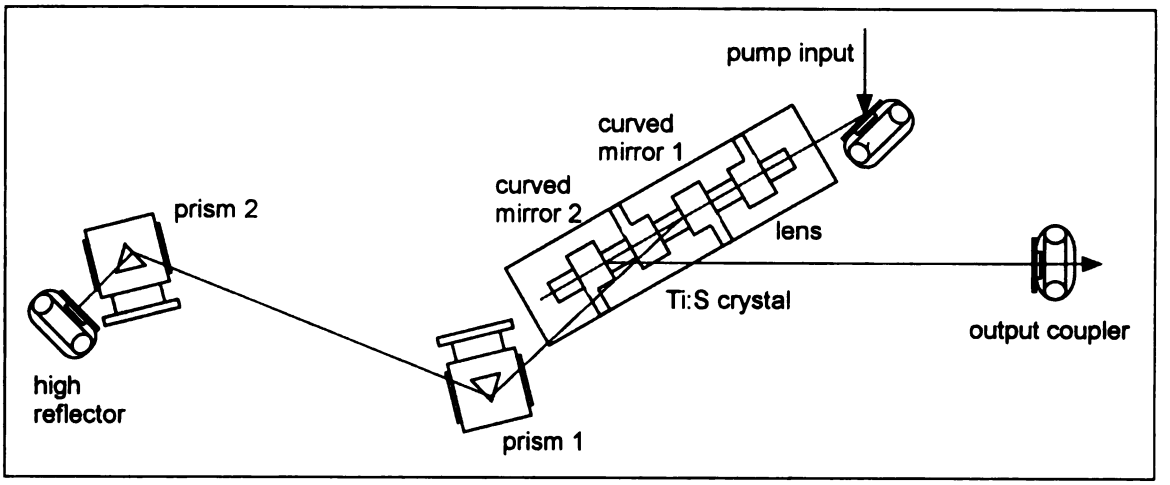

Figure 2.3. Ti:S laser oscillator system.

2.1.2 Regeneratively Amplified Ti:S Laser System

High energy laser systems are generally classified by their method of amplification as regenerative or multi-pass. Regenerative amplification, which describes the system in our laboratory, provides a more efficient use of the gain and better stability, but results in greater phase distortions in the output pulse. Multi-pass amplification avoids some of these phase distortions by operating with fewer optical elements through which the laser beam transmits several times. Although shorter pulses can usually be achieved by multi-pass amplification,[85] difficulties with alignment and lower pulse to pulse stability make regenerative amplification systems more practical.

The KHz laser system in our laboratory comprises four parts: an oscillator that produces femtosecond pulses in the near IR, a stretcher that lengthens the pulses to a few

hundred ps, an amplifier stage that increases the pulse energy and a compressor that reduces the pulses to about 50 fs.

The oscillator of the KHz laser system delivers laser light pulses of 15 fs with energy of 2 nJ. Since this power is not sufficient for the applications described in Chapters 5 and 6, the laser pulses are amplified using the Chirped Pulse Amplification (CPA) technique.[86, 87] In CPA (Figure 2.4), an ultrashort laser pulse is stretched out in time prior to introducing it to the gain medium using a pair of gratings that are arranged so that the low-frequency component of the laser pulse travels a shorter path than the high-frequency component does. After going through the grating pair, the laser pulse becomes positively chirped, that is, the high-frequency component lags behind the low-frequency component, and has longer pulse duration than the original by a factor of 10^3 to 10^5. The resulting stretched pulse is then safely introduced to the gain medium and amplified by a factor of approximately 10^6. Finally, the amplified laser pulse is recompressed back to the original pulse width through the reversal process of stretching (compression), achieving orders of magnitude higher peak power than laser systems could generate before the invention of CPA.

Most of the spectral phase distortions accumulated by the laser pulse inside the regenerative amplification cavity can be compensated by a pulse shaper. For this reason, a pulse shaper was introduced between the oscillator and regenerative amplifier to compensate these distortions and offset spectral narrowing in the amplifier. The result is a very stable source with a pulse duration of ~30 fs (33 nm bandwidth).

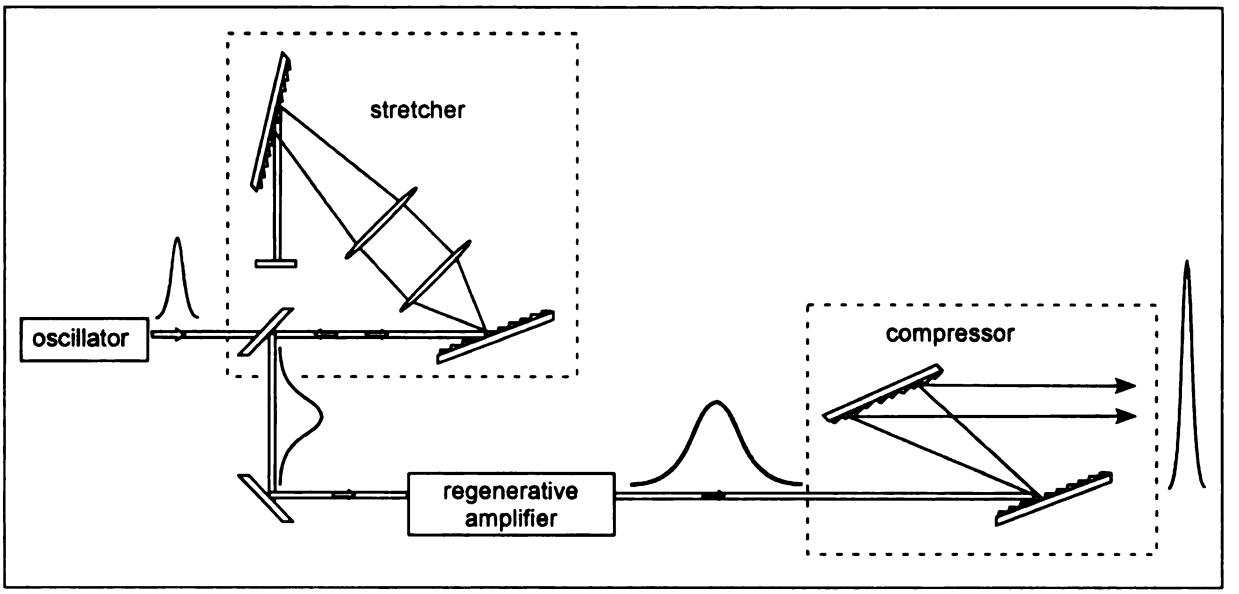

Figure 2.4. Chirped pulse amplification

2.2 Pulse Shaper

Many approaches in femtosecond pulse shaping are dedicated to the synthesis of laser waveforms by spectral filtering of a spatially dispersed frequency spectrum. The earliest available pulse modulation scheme still in use is frequency chirping, where frequency components in a laser pulse are arranged with a certain phase ordering. This can be easily achieved by dispersing the ultrafast pulses through a pair of gratings or through propagation in an optical fiber. As a consequence, an otherwise bandwidth-limited ultrafast pulse is stretched in time. Most practical applications of shaped pulses require a pulse shaping device that can be used to construct desired pulses with appropriate amplitude and phase modulations. The idea of pulse shaping entails the modulation of the incident electric field of the laser by a mask in the frequency domain. This results in an outgoing shaped spectral electric field.

Femtosecond laser pulses can not be directly shaped in the time domain because of their short duration. There are currently no electronic devices which work with such speeds. For this reason, the indirect technique for shaping ultrafast laser pulses involves splitting the pulse into its frequency components, modulating these in the required manner and recombining them to obtain the shaped pulse. This requires the use of modulators like LQ modulators. The method we used in this work – pulse shaping with an SLM at the Fourier plane – is described below. A pulse shaper is implemented to manipulate the electric field that interacts with the molecules.

2.2.1 SLM

The femtosecond pulse shaper using a LQ-SLM was pioneered by Heritage and Weiner.[7, 88] The LQ-SLM used in this research is a commercially available device (Cambridge Research Institute, Inc.) – a double mask SLM unit[89, 90] which consists of two linear LQ arrays of 128 pixels each, separated by 2.2 mm, with independent control of each pixel. Figure 2.5 (A and B) illustrates the front face and side view of the SLM. The two LQ arrays are perpendicular to each other and are oriented 45° to the incoming light. They are placed between two silica substrates coated with indium tin oxide, an optically transparent material which is electrically conductive. One substrate is the ground plate and the other is patterned with a linear array of 128 electrodes (width of 100μm each) that define the pixels. The 3 μm spacing between the electrodes cannot be controlled. Each pixel in the first array is superimposed directly in front of the corresponding pixel in the second array. These arrays allow the independent or simultaneous control of phase and amplitude. The LQ components in each array are

birefringent. Depending on the polarization of the incoming light, a voltage can initiate pure phase retardation (delay) or a combination of phase retardation and polarization rotation.

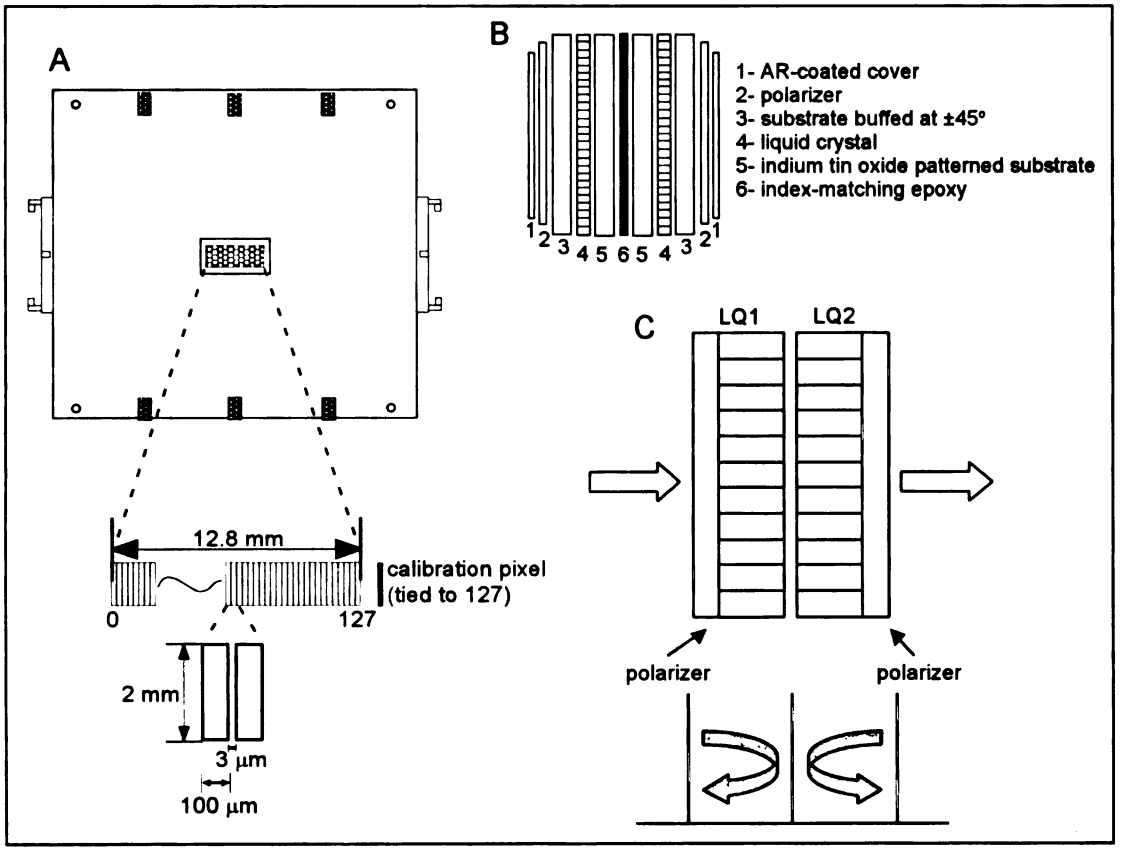

Figure 2.5. The LQ-SLM. A. Front view with pixel dimensions. B. Side view showing components of the SLM. C. Direction of polarization as laser pulse goes through each LQ mask.

Figure 2.5 C depicts how this SLM unit operates. Light incident on the SLM first goes through a polarizer and transmits to the first LQ array where its phase undergoes retardation and polarization is rotated in one direction. As the light hits the second LQ array, it undergoes more retardation in phase and is polarized in the opposite direction. On average, LQ-SLM systems provide retardance equal to 4π. The second polarizer is

utilized for amplitude modulation. Polarization rotated away from the incident, horizontal direction causes the attenuation of light by this second polarizer. Rotation by 90° results in zero transmission. This dependence on polarization is employed in the calibration of the SLM.

Control over the retardance introduced by each pixel is established from the voltages introduced in the SLM. The basic factor is determining the overall differences between pixels and the changes in retardance. Calibration of the SLM is accomplished by obtaining a frequency-dependent calibration curve of the laser spectrum. Increasing the voltage, V, of one of the LQ masks while keeping the other mask at a constant voltage generates a transmission function, T, which can be used to calibrate the dependence of retardance on voltage.

$$T = \cos^2[\frac{\pi(R_A(V_A) - R_B(V_B))}{\lambda}] \qquad 2.1$$

$R(V)$ refers to the retardance as a function of voltage for each LQ array, A and B. The total phase retardation, ϕ, obtained from changes in T, can then be calculated by

$$\phi = \pi[R_A(V_A) + R_B(V_B))/\lambda \qquad 2.2$$

Needless to say, the accuracy by which phase can be controlled by the pulse shaper is contingent on a well-calibrated SLM.

2.2.2 Pulse Shaping Apparatus

The operation principle of a pulse shaper is based on optical Fourier transformations from the time domain into the frequency domain, and vice versa. This section focuses on the two pulse shaping setups used in this work. All the optical elements in the pulse shaping apparatus are symmetrically separated by the focal length

of the lenses, f, so that the pulse leaving the setup has the same characteristics as the pulse entering the setup ($4f$). The collimating lenses and grating pair are set up in a $4f$ configuration[90], with the SLM being placed at the center. The whole pulse shaping setup, without the SLM, introduces no dispersion if the $4f$ condition is met, and is called a zero-dispersion compressor. This dispersion-free condition takes into account that the lenses are thin and free of chromatic aberrations. A grating spreads the pulse, so that different spectral components map onto different spatial positions.

2.2.2.1 The Linear Setup

The linear $4f$-setup (Figure 2.6) uses two gratings and two lenses. The first grating spectrally disperses the femtosecond pulse. The frequencies are collimated by the first lens, which Fourier transforms the pulse from the time domain into the spectral domain. In the Fourier plane of the lens, the spectral components are spatially separated along one dimension. They are focused by the second lens onto the second grating. An inverse Fourier transform into the time domain takes place after passing the second lens. Cylindrical lenses are required in order to avoid damaging the polarizers in the SLM. If the lenses are not separated by $2f$, the beam is divergent and a temporal chirp leaves the setup. If the gratings are not situated exactly in the focal plane of the lenses, an additional spectral chirp, where the frequencies are spatially separated within the laser beam profile, is generated. This distorts the temporal phase of the pulse and cannot be compensated.

This setup was used for the experiments on selective ionization and photofragmentation described in Chapters 5 and 6, with the amplified femtosecond laser

system described in Section 2.1.2, which provides laser pulses with a spectral bandwidth of up to $\Delta\lambda = 27$ nm at FWHM. The intensity of the laser beam after passing through this configuration decreases by about 40%.

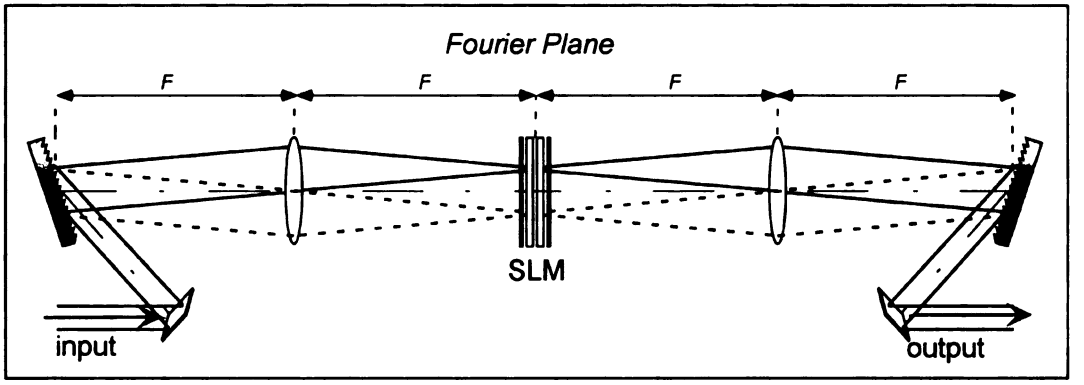

Figure 2.6. Schematic design of a linear 4f pulse shaper using diffraction gratings and an SLM

2.2.2.2 The Folded Setup

For pulses with larger bandwidths, provided by the femtosecond laser oscillator system described in Section 2.1.1, the folded pulse shaping system was used. The shorter pulses make gratings too dispersive, so a setup that is less dispersive is more advantageous. In this setup, prisms, which are about an order of magnitude less dispersive than gratings, were used to disperse the frequency components of the pulse. Instead of cylindrical lenses, we used cylindrical plane concave mirrors where their inner concave sides were covered with a dielectric layer, leading to a reflectivity of 99%. The overall intensity losses of the folded setup are about 25%. The off-axis aberration caused by the diffraction of the spectrum by the prism onto the cylindrical mirrors is minimized

by two folding mirrors. Figure 2.7 shows the folded pulse shaping setup, which was used for the experiments on selective two-photon excitation described in Chapters 3 and 4.

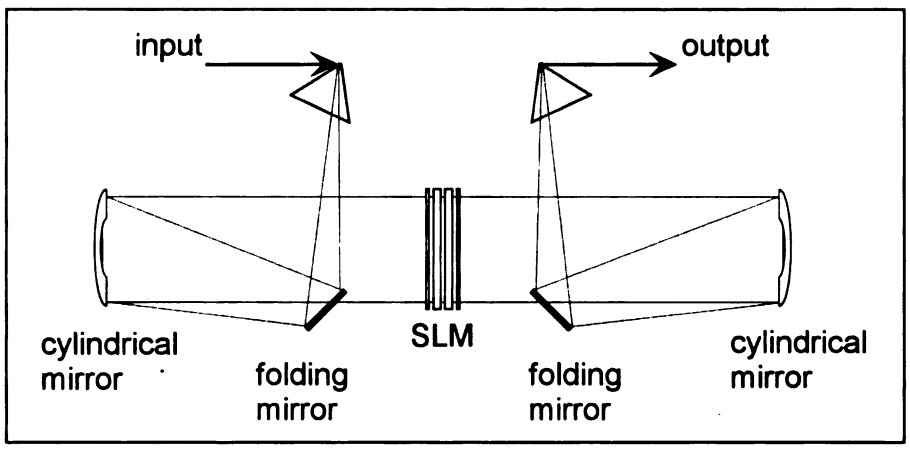

Figure 2.7. Schematic design of a folded pulse shaper using prisms in lieu of gratings.

2.2.3 Phase Modulation with the LQ-SLM

The programmable LQ-SLM used in this work is capable of both phase and amplitude modulation. The incident light that enters the pulse shaper is horizontally polarized. This ensures parallel polarization with the extraordinary axis of the LQ (*x*-axis) at the input face of the SLM. At the output face, a polarizer selects only the horizontally polarized light. As the input light field passes through the first LQ array, its polarization is rotated in one direction according to the phase retardance $\Delta\phi^A$. As it passes through the second array, a voltage-dependent phase retardance $\Delta\phi^B$ occurs and polarization is rotated in the other direction. The polarization can also be rotated in such a way that the attenuation is compensated while the phase shifts. The average phase

retardance is given by $\exp[i(\Delta\phi^A + \Delta\phi^B)/2]$. The amplitude is altered according to the cosine of the differential retardance $\Delta\phi^A - \Delta\phi^B$.

The output electric field E_n^{output} of the nth pixel after leaving the SLM is given by,

$$E_n^{output} = E_n^{input} \cdot \cos((\Delta\phi^A - \Delta\phi^B)/2) \cdot \exp(i(\Delta\phi^A + \Delta\phi^B)/2) = E_n^{input} R_n, \qquad 2.3$$

where $\cos((\Delta\phi^A - \Delta\phi^B)/2)$ is the amplitude modulation term, and $\exp(i(\Delta\phi A + \Delta\phi B)/2)$ is the phase modulation term. $R_n = \exp(i\psi(\omega))$; $\sqrt{T_n}(\omega)$ is the filter function applied to the nth pixel; $T_n(\omega)$ is the transmission and $\psi_n(\omega)$ is the phase filter of each element. For $\psi(\omega)=0$ the spectral filter function allows amplitude-only modulation, while for $T_n(\omega)=1$ the filter function can modulate only the phase mask.

Pure phase modulation is achieved when the cosine in the expression is equal to 1, a condition that is achieved by keeping $\Delta\phi^A = \Delta\phi^B$. Amplitude modulation is also accompanied by phase modulation. As the SLM possesses two LQ arrays, the second one compensates for the unwanted phase modulation so that pure intensity attenuation of the optical waveform is obtained. Neither of the two masks alone is able to modulate phase or amplitude, but their combination allows independent phase and amplitude modulation.

2.2.4 Limitations of the SLM

The number of pixels in LQ modulators limit the resolution of the modulation. The finite width covers a range of wavelengths, reducing the fidelity of shaping. The optical setup, particularly the focal spot size that is projected across the lens towards the

SLM, if not given careful attention, can further reduce spectral resolution. The dead spaces or gaps between electrodes also add artifacts to the pulse train. Although typical LQ-SLM systems provide 4π retardance, in theory, only 2π retardance is required since the phase can be folded (distributed into separate 0-2 π segments) to produce any type of total retardance. Folding the phase can, however, introduce additional unwanted modulation into the pulse because of the abrupt phase changes required for folding.[91] In addition, the limited resolution of the shaper prevents clean phase jumps from one pixel to the next. Nonetheless, the excellent agreement between experimental and theoretical predictions obtained for most nonlinear optical experiments implies that these shortcomings are quite trivial.

CHAPTER 3

SELECTIVE TWO-PHOTON EXCITATION

Multiphoton excitation draws on an old idea in quantum theory and, in the course of its infusion in microscopy, is currently being applied to a number of modern scientific problems. This chapter dwells on the possibility of utilizing MII to attain selective excitation of fluorophores without the need for wavelength tuning, optical setup modifications, and selective visualization with filters. The basic idea is to exploit the high peak intensity of the femtosecond laser to attain multiphoton excitation, and to make use of its wide spectral bandwidth to access a wide range of frequencies that could be manipulated through intrapulse interference to bring about selective two-photon excitation. Fluorescence selectivity through multiphoton excitation with shaped femtosecond laser pulses could have large implications in terms of the ability to recognize and monitor the environment and dynamics around a fluorophore in a complex biological system.

The most commonly used type of multiphoton excitation is two-photon excitation (described by Göppert-Mayer in 1931), where simultaneous absorption of two low-energy photons leads to a single quantum event. The powerful advantages of two-photon excitation microscopy[92] arise from the basic physical principle that absorption depends on the square of the excitation intensity. In practice, two-photon excitation is generated by focusing a single pulsed laser through a microscope. As the laser beam is focused, the photons become more crowded, but the only place at which they are crowded enough to generate an appreciable amount of two-photon excitation is at the focus. Photons are not

only crowded spatially (by focusing) but also temporally (by using mode-locked laser pulses). This gives the needed excitation intensities for multiphoton absorption, but limits the average power at the focus to less than 10 mW. The limited excitation region reduces phototoxicity because photodamage is largely confined to the focal volume.

In two-photon fluorescence microscopy, the excitation wavelength is in the near IR, a region of the spectrum in which there is virtually no absorption in cells or most chemical systems. The most widely used light source for multiphoton microscopy is the Ti:S laser which normally has a pulse width of ~100 fs and a repetition rate of ~ 80 MHz, allowing the high photon density and flux required for two photon absorption and is tunable across a wide range of wavelengths. The use of longer wavelength excitation light slows the rate of photobleaching of the sample, allowing the use of higher magnification objectives. In addition, longer wavelength light can penetrate deeper into a specimen. In fluorescence microscopy, excitation light incident on the specimen can be scattered (Rayleigh scattering) to various degrees before it reaches the focal plane, and the resulting fluorescence can also undergo scattering as it returns through the specimen toward the detector. These scattering effects combine to reduce the collected fluorescence signal. The simplest approximation of Rayleigh scattering shows that the amount of scattered light is inversely proportional to the fourth power of the light's wavelength. Thus 400 nm light (one-photon) light would be expected to undergo several times more scattering than 800-nanometer (two-photon) light.

Successes associated with two-photon microscopy have also created interest in exploring applications based on three-photon excitations. For a three-photon process, a longer excitation wavelength such as those common in optical communications can be

used. The cubic dependence of the three-photon process on the incident light intensity provides a stronger spatial confinement, so that a higher contrast in imaging can be obtained.

The notion that phase modulation can be used to attain selectivity in two-photon excitation is motivated by the need to keep the laser characteristics constant throughout the excitation process. Tweaking the laser or moving optical elements to attain the desired excitation wavelength for a particular fluorophore can be averted by controlling the phase of a laser pulse. The following Sections show how the use of a pulse shaper for two- or three-photon microscopy provides the flexibility of selective probe excitation or maximum signal enhancement by controlled modulation of the spectral phase of femtosecond pulses.

3.1 Probing a Molecule's Microenvironment[a]

3.1.1 Introduction

This work focuses on the design of tailored femtosecond pulses to achieve control of nonlinear optical excitation in large molecules based on the concept of MII.[65, 66] The goal is to elucidate well-defined and reproducible pulse shapes that can be used to enhance or suppress particular nonlinear optical transitions in large molecules such as laser dyes and proteins in solution. The use of MII to probe the local and microscopic environment of molecules by selective two-photon laser induced fluorescence (LIF) is discussed in this section.

There has been much interest in the use of tailored ultrafast laser pulses to control the excitation of large molecules in condensed phase.[45, 51, 93, 94] Coherent control of large molecules in condensed phase has been considered very challenging because of the large numbers of intra and intermolecular degrees of freedom involved.[95] Further complications arise from the extremely fast homogeneous (< 100 fs) and inhomogeneous (< 10 fs) electronic dephasing in these systems.[96] Many of these studies have been based on the concept of pulse shaping, whereby a learning algorithm optimizes the spectral phase of the laser field.[11] These methods have the advantage of convergence to an optimal pulse shape. However, because of the sensitivity of high-intensity multiphoton excitation to a large number of experimental parameters (for example pulse intensity fluctuations, saturation, transverse-mode quality, pulse bandwidth, and spectral phase which is affected by transmission through lenses and windows and reflection from dielectric mirrors), it is difficult to ascertain principles from the results of these

[a] Reproduced in part with permission from J.M. Dela Cruz, I. Pastirk, V.V. Lozovoy, K.A. Walowicz, M. Dantus, Multiphoton Intrapulse Interference 3: Probing Microscopic Chemical Environments *J. Phys. Chem. A* 2004, **108**, 53-58. Copyright 2004 American Chemical Society.

experiments. Furthermore, it has never been shown that results from these types of experiments can be reproduced.

The influence of phase on two-photon excitation was explored by Broers et al., who proposed that certain phase functions could focus the second harmonic spectrum in the frequency domain like a Fresnel lens focuses light in the spatial domain. They demonstrated this principle by controlling the two-photon excitation of Rb atoms.[10] Meshulach et al. used the same principle to demonstrate coherent control on the two-photon excitation of Cs atoms.[59] Their work focused on the narrow two-photon absorption resonance; they showed that the coherent two-photon enhancement was absent in the broadband excitation of large molecules in solution.[59] Work from the Dantus group demonstrated that the changes introduced by pulse shaping on two- and three-photon transitions arise from destructive interference, not on focusing in the frequency domain.[66] The theoretical framework that was conceived as a result of this observation led to the development of MII for controlling multiphoton excitation in large molecules in solution.[65, 66] The fundamental advantage of this method was the early realization that very short pulses, with concomitant large bandwidths, would be needed to control the nonlinear excitation of complex systems. Unlike in the gas phase, the existence of inhomogeneous broadening in the condensed phase prevents the coherent manipulation of vibronic levels. MII could control the delivery of energy to the molecule with little or no dependence on intramolecular dynamics.

The first application of phase tailored pulses for sensing pH involved intense linearly chirped laser pulses that saturated the one-photon resonant transition of a pH-sensitive dye.[61] The ratio between the LIF signals obtained for positively and negatively chirped

pulses was found to vary from 1.9 to 1.2 for different pH values. However, this ratio did not vary monotonically, being the same for pH 7 and pH 9.

The method presented here is completely different from the early experiments of Buist et al.[61] This method involves very weak pulses inducing two-photon transitions. The samples are thus transparent at the carrier wavelength of the pulse, the transitions are not saturated, and the results are independent of probe molecule concentration. The mechanism we used for pH probing is understood and theoretical simulations are in close agreement with the data.

The probability for two-photon excitation, $S^{(2)}$, using phase-modulated pulses at frequency $\omega = \Delta + \omega_0$, where ω_0 is the carrier frequency, can be calculated from the expression[66]

$$S^{(2)} \propto \int g^{(2)}(2\omega) \left| \int E(\omega+\Omega) E(\omega-\Omega) d\Omega \right|^2 d\omega, \qquad 3.1$$

where $E(\omega) = |E(\omega)|\exp(i\phi(\omega))$ is the electric field of the laser. In this expression, we assume a broad nonlinear two-photon absorption spectrum, $g^{(2)}(2\omega)$ and ignore intramolecular dynamics to simulate our experimental results. Consequences of this assumption are addressed later.

Here we demonstrate the MII method, which couples the sensitivity of multiphoton excitation on the spectral phase of the laser pulses to probe microscopic chemical environment-induced changes in the multiphoton excitation spectrum of sensitive reporter molecules. We carry out the optimization of the required phase functions in solution and provide theoretical simulations.

3.1.2 Experimental Section

Experiments were performed using a Ti:S laser oscillator (K&M Labs) capable of producing pulses with bandwidths up to 80 nm FWHM. The output of the oscillator was evaluated to make sure there were no changes in the spectrum across the beam and was compressed with a double prism pair arrangement shown in Figure 3.1. The pulse shaper uses prisms as the dispersive elements, two cylindrical concave mirrors, and an SLM (CRI Inc. SLM-256), composed of two 128-pixel LQ masks in series. The SLM was placed at the Fourier plane.[90]

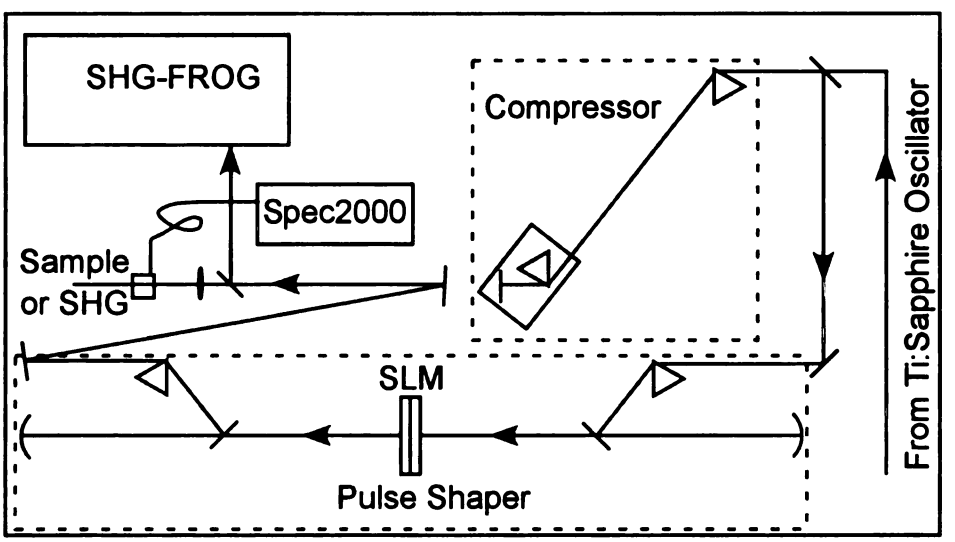

Figure 3.1. Schematic of the laser setup for MII experiments. The output of the Ti:S oscillator is compressed by the prism pair compressor before arriving at the pulse shaper. Phase and amplitude shaping take place at the SLM which incorporates a polarization optic at its input and output windows. Once shaped, the pulses are directed towards the experimental cell. Characterization of the pulses by MIIPS requires replacing the sample cell by a thin SHG crystal; alternatively, the pulses are directed to an SHG-FROG.

Because the retardance introduced by the LQ is frequency dependent, pulse shaping of ultrashort pulses (with > 100 nm total bandwidth) requires calibration of each pixel element. At the end of the calibration, our data acquisition program maps the

spectrum of our laser on the SLM in a frequency rather than wavelength scale. An algorithm has been programmed to independently control amplitude and phase at each frequency with the SLM. This allows us to define a Gaussian shape or spectrum in the frequency domain using an amplitude mask, and then to scan the phase function without affecting the spectrum of the pulse. After compression and pulse shaping, ~ 200 pJ pulses were used to interrogate the samples.

The reproducibility of pulse shaping experiments depends on accurate characterization of the phase of the laser pulses. For this task we used the MIIPS method[97] to measure both the sign and magnitude of phase distortions in the pulse. This method was described in Chapter 1.2. For the experiments in this study, we started with very broad bandwidth pulses (~80 nm FWHM). We then defined Gaussian spectra of the desired width and center wavelength by amplitude shaping. Second, we measured the quadratic and cubic phase distortions in the pulse by scanning a phase function defined by Equation 1.1, where the amplitude α was set to 1.5π rad, and γ was set to the approximate pulse duration (20 fs).

After MIIPS, the final pulse shaping step involved the controlled phase modulation of TL pulses. This step involved introducing phase functions determined by Equation 1.1. The laser was focused by a 50 mm focal length lens onto a 10 mm path length quartz cell containing the dye solution. Fluorescence perpendicular to the excitation beam was collected near the front face of the cell to minimize dispersion in the sample. We took advantage of the narrow acceptance angle of the optical fiber for spatial filtering and imaged the signal onto an Ocean Optics spectrometer (S2000). The experiment involved scanning the parameter δ and detection of the fluorescence of the

sample (spectrally integrated). Signal integration time was typically 500 msec per spectrum for each value of δ, and the data scan, with 256 different phase positions was averaged over 3 cycles of δ from 0 to 4π rad.

The samples used were 10^{-5} M aqueous solutions of 8-hydroxypyrene-1,3,6-trisulfonic acid trisodium salt (HPTS or 3sPyOH) (Sigma-Aldrich) in different pH buffer solutions. The pH 6 buffer was prepared from 0.1 M KH_2PO_4 (250 mL) in 0.2 M NaOH (14 mL); pH 8 buffer was prepared from the same solutions, but with more (115 mL) of the NaOH; while the pH 10 buffer solution was prepared from 0.025 M $Na_2B_4O_7$ (250 mL) in 0.2 M NaOH (27 mL). The buffer solutions were diluted to 500 mL with distilled water. UV-visible absorption spectra of the dye solutions at different pH environments were obtained with a Hitachi U-4001 UV-vis spectrophotometer.

3.1.3 Results

Figure 3.2 illustrates the dependence of two-photon LIF on phase modulation. These measurements were obtained using 23 fs TL pulses that were shaped to have a Gaussian spectrum centered at 842.6 nm with a bandwidth of 48 nm FWHM and spectral phase defined by Equation 1.1. Figure 3.2A shows the experimental two-photon LIF intensity from HPTS in a pH 10 solution (dots) as a function of δ. The signal shows a sinusoidal modulation. Figure 3.2B shows the experimental two-photon LIF intensity from HPTS in a pH 6 solution (dots) as a function of δ. The signal is modulated, however, there is a clear phase shift compared to pH 10. The shift comes about from pH-induced changes in the two-photon absorption spectrum. Experiments obtained for pH 8 were similar to those obtained at pH 10 but they contained a small shift that made them

distinguishable. It is crucial to underline that the laser spectrum and intensity remain unchanged throughout the experiments and that the emission spectrum from the dye is independent of pH.

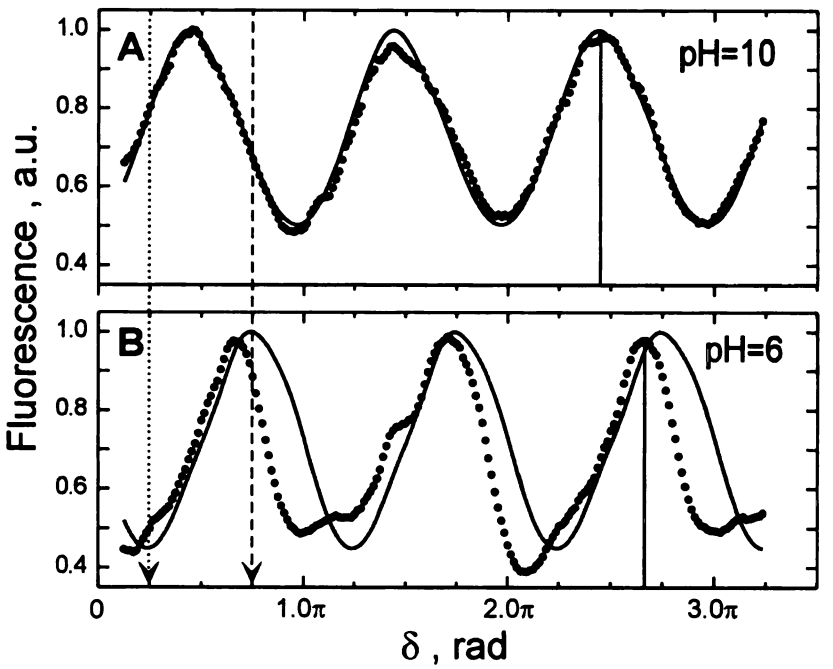

Figure 3.2. Experimental MII results and simulations for HPTS in basic and acidic solutions. Intensity of the two-photon induced fluorescence of HPTS solution at pH 10 (A) and pH 6 (B) are plotted as a function of the phase parameter δ. Simulations (continuous lines) based on Equation 3.1 are in good agreement with the experimental data (dots). The arrows at $\delta = 1/4\pi$ (dotted) and $\delta = 3/4\pi$ (dashed) represent phase functions for which the intensity of two-photon fluorescence from HPTS at pH 10 is similar but shows large differences for pH 6. The optimum two-photon excitation of HPTS is indicated by vertical lines for the acid and basic solutions.

Simulations of the experimental signal were performed using Equation 3.1 without adjustable parameters. The spectrum of the pulse and the absorption spectrum of HPTS were measured experimentally. An examination of the molecular structure of HPTS shows that it has no center of symmetry. Since parity restrictions may be relaxed in this case, the similarity between one-photon and two-photon absorption spectra is

expected. The spectral phase $\varphi(\Omega)$ imprinted by the phase mask was the same used for the simulations. Both experimental and theoretical data were normalized such that the signal intensity is unity and the background observed is zero. Generally, the experimental data (dots) agree quite well with the calculated response (continuous line) of the dyes in all pH environments (see Figure 3.2). Differences found for pH 6 are discussed below.

We repeated our experiments with 50 fs pulses centered at 760 nm. No differences in phase dependence were observed for the three different pH solutions, as expected and as corroborated by simulation. The absorption spectrum of HPTS in the three different pH environments (pH 6, 8 and 10) is relatively flat near 380 nm. These control measurements indicate that the phase dependence arises primarily from differences in the two-photon excitation spectrum and not from intramolecular dynamics.

3.1.4 Discussion

The MII method is used in this experiment to control two-photon excitation. More specifically, the interference process, which is controlled by the phase introduced in the pulse, suppresses two-photon transitions at specific frequencies within the two-photon bandwidth.[66] In other words, the interference can be used to tune multiphoton transition probability at specific frequencies. This effect can be envisioned from scanning SHG intensity using MIIPS. As δ is scanned the maximum intensity in the second harmonic signal scans as well from longer to shorter wavelengths.[65, 66] By considering this effect together with the two-photon absorption spectrum, the expected signal can be calculated with very good agreement.

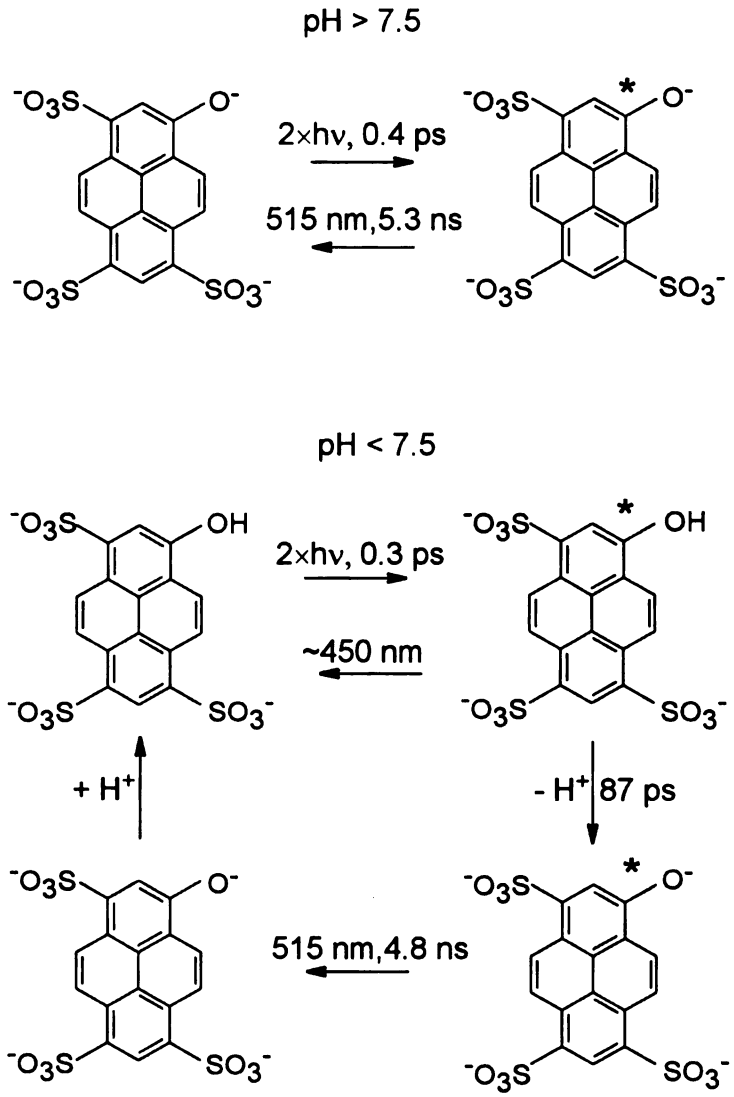

Figure 3.3. Photochemistry of HTPS in basic (pH > 7.5) and in acid solutions (pH < 7.5). Upon two-photon excitation, the equilibrium species in basic solution ($3sPyO^-$) reaches an excited state that is solvated within 0.4 ps. Fluorescence from $3sPyO^{-*}$ has a lifetime of 5.3 ns and is centered at 515 nm. The equilibrium species in acidic solution (3sPyOH), upon two-photon excitation, reaches an excited state that is solvated within 0.3 ps. Fluorescence from $3sPyOH^*$ is near 450 nm, however, deprotonation to yield ($3sPyO^{-*}$) takes place within 87 ps and is followed by fluorescence centered at 515 nm with a 4.8 ns lifetime.

HPTS is a highly water-soluble, pH-sensitive dye with a pK_a of ~7.5 in aqueous solution.[98] The photochemistry of this system is shown in Figure 3.3. When in alkaline medium, pH > 7.5, acid-base equilibrium is totally displaced toward the anion form

($3sPyO^-$) of the dye. The electronic character of $3sPyO^-$ remains unchanged after photo-excitation, and corresponds to a singlet excited state.[99] Fluorescence from this state undergoes a fast 0.4 ps Stokes shift and has a maximum at 515 nm and a lifetime of 5.3 ± 0.1 ns.[100]

In acidic medium, pH < 7.5, the conjugate acid form (3sPyOH) dominates in the ground state. Two-photon excitation yields the excited state (3sPyOH*). Fluorescence from this state undergoes a fast 0.3 ps Stokes shift and has a maximum near 450 nm. HPTS has a very high fluorescence quantum yield (almost 100% in both alkaline and acidic solution, when excited with light of wavelengths shorter than 400 nm).[101] Proton transfer in the excited state takes place in 87.5 ps[99, 100] to yield the conjugate base ($3sPyO^{-*}$) (see Figure 3.3), with a fluorescence maximum at 515 nm and a lifetime of 4.8 ± 0.5 ns. Therefore, in both acidic and basic environments, the emission spectrum is unchanged. The nature of the excited state dynamics involves a three-step mechanism of the proton transfer reaction, whereby an intermediate state (unionized acid form) with significant charge transfer character converts to the fluorescent excited anionic state.[100]

There has been speculation about the manipulation of intramolecular dynamics of large molecules in condensed phase. In Figure 3.4, we show the spectrum, phase and time profiles for the shaped pulses with $\delta = \pi/4$ (dotted line) and $3\pi/4$ (dashed line). Notice that both of the pulses show identical time structure. The periodicity of the structure has an average period of ~ 50 fs and lasts for about 200 fs. Given the similarities between the two pulses, the control mechanism does not depend on temporal differences. The typical electronic dephasing time of laser dyes in solution is shorter than ~100 fs, preventing coherent manipulation by these shaped pulses. Based on these observations and the fact

that the simulations, which neglect intramolecular dynamics, are in excellent agreement with the experimental data (especially pH 10), we conclude that intramolecular dynamics plays a minimal role in the control that is observed.

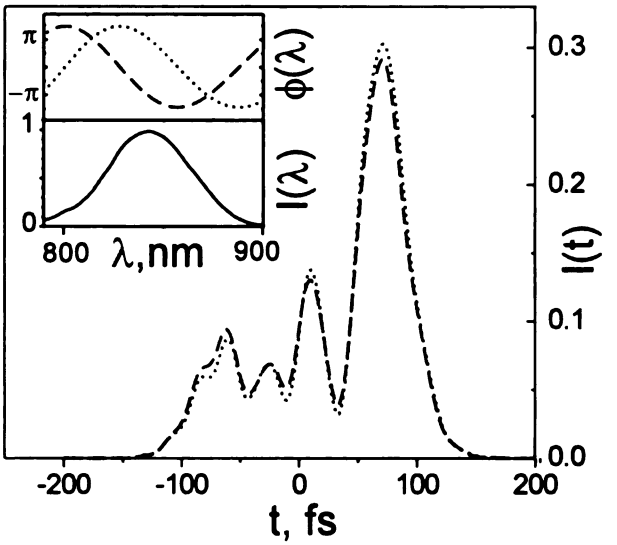

Figure 3.4. Laser pulse characteristics in the time and spectral domain. The inset shows the measured spectrum of the pulse $I(\lambda)$ and the phase $\phi(\lambda)$ programmed by the SLM. The pulses have a Gaussian shape with center wavelength $\lambda_0 = 842.6$ nm and 48 nm FWHM. The temporal profile for two pulses (dotted and dashed lines) is calculated from the experimental parameters for $\delta = 1/4\pi$ and $\delta = 3/4\pi$, respectively. Notice that the two pulses have the same temporal profile.

Some discrepancy between experiment and simulation is seen for the data obtained under acidic conditions. The simulations were obtained using the measured linear absorption spectrum of HPTS at pH 6 (see Figure 3.5). It is possible that the two-photon spectrum is significantly different from the one-photon absorption spectrum. Alternatively, fast dynamics may be causing the difference. However, the time scale for proton transfer is much slower than the shaped pulses.

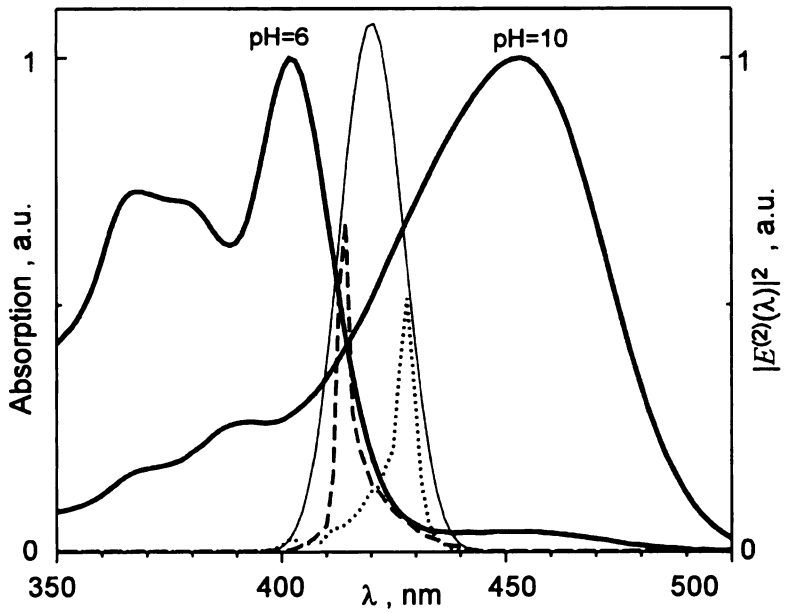

Figure 3.5. Absorption spectra of HPTS in acidic and basic solution (bold lines). The thin line is the calculated spectrum of the square of the electric field ($|E^{(2)}(\lambda)|^2$) of the laser pulse without phase modulation (TL). The square of the electric field of the laser pulse is also calculated for shaped pulses with $\delta = 1/4\pi$ (dotted) and $3/4\pi$ (dashed), respectively. The two spectra are very different because of MII. Notice that in the frequency domain, it is clear that shaped pulses with $\delta = 1/4\pi$ favor two-photon excitation of HPTS in pH 10, while pulses with $\delta = 3/4\pi$ favor two-photon excitation of HPTS in pH 6.

In Figure 3.5, we show the absorption spectra of HPTS at pH 6 and pH 10. The spectrum of the electric field $E^2(t)$ is proportional to $|E^{(2)}(\lambda)|^2$, and is shown for a TL pulse (thin line) and for phase modulated pulses with $\delta = \pi/4$ (dotted line) and $3\pi/4$ (dashed line). Notice that two-photon transitions at 410 nm take place preferentially when $\delta = \pi/4$, favoring probe molecules in a pH 10 environment. Two-photon transitions at 430 nm take place preferentially when $\delta = 3\pi/4$, favoring probe molecules in a pH 6 environment. This explanation in the frequency domain is consistent with the observed results and simulations. Note that phase shaping does not tune the wavelength of the laser

pulse. The changes in the two-photon probability for different frequencies arise from the interference, which is controlled by the spectral phase imprinted in the pulses.[65, 66]

Pulse shaping and, in particular, the use of MII provide a number of advantages for multiphoton microscopy. (a) A very short pulse laser is set up once and optimized once (no subsequent tweaking). (b) The short pulse duration has the advantages of higher multiphoton excitation efficiency and broader bandwidth. (c) As the phase is optimized for selective excitation, maximum efficiency is maintained; there is no need for tuning, realigning, tweaking, compensating for chirp, and renormalizing. (d) The system is computer-controlled and can take advantage of phase compensation at the sample using MIIPS, as described here. (e) MII can be used to control two- or three-photon excitation. (f) During the selective excitation experiments the intensity and spectrum of the laser remain constant; therefore, one-photon processes like absorption, reflection, and scattering remain constant as well. (g) Selective photochemistry can be realized through shaped pulse excitation and this can be used for selective multiphoton microlithography.

3.1.5 Conclusion

Selective excitation of large fluorescent probes is achieved by optimizing the overlap between the power spectrum of the pulse and the two-photon absorption spectrum of a molecule. Phase modulation of ultrashort pulses through MII can be used to probe chemical changes that take place within cells as they respond to external changes in their environment. The effect can be further enhanced using even shorter (larger bandwidth) femtosecond pulses. The quantification of changes in intracellular ion concentration can be accomplished with the use of fluorescent indicator dyes[102] based on

shifts in their two-photon excitation spectrum. MII has demonstrated applicability in the study of biochemical phenomena, and this is validated by its significant role in selective microscopy (discussed in Section 3.2). Practically all of the cellular processes can potentially be affected by changes in intracellular pH. The absorbance and/or emission properties of fluorescent dyes are affected by their environment, including solvent, pH, and conjugation to other macromolecules (e.g., nucleic acids). Changes in intracellular pH are often one of the responses of cells to externally applied agents, including growth factors and pathogens.[103] The principles of MII can be similarly applied to other biologically relevant local environment parameters, like sodium or calcium ion concentration.

3.2 Selective Two-Photon Microscopy[b]

3.2.1 Introduction

Two-photon microscopy has provided researchers with unique possibilities for fluorescence imaging and photochemistry. It offers attractive advantages, including higher resolution, background-free signal, lower background scattering, better penetration in thick samples, and reduced photon-induced damage,[92, 104, 105] which arise from the basic physical principle that the absorption depends on the square of the excitation intensity. Two-photon microscopy has been shown to be amenable to multiple probe staining, whereby two-photon transitions excite different probe molecules that emit at different wavelengths[105, 106] and for functional imaging of living cells.[107-110] Here, we demonstrate how phase-modulated femtosecond pulses can selectively excite one type of probe molecule only, leaving the others in their ground state. Selectivity in multiphoton excitation is achieved by MII as outlined below.[65, 66, 111] Selective excitation can be used to enhance contrast and to achieve functional imaging of samples stained with fluorescent probes sensitive to their microscopic chemical environment.

3.2.2 Experimental Section

The experiments are carried out using a Ti:S oscillator (K&M Labs) laser system capable of generating pulses as short as 11 fs after a double-pass prism compressor. The amplitude profile and spectral phase of the pulse are tailored using a computer-controlled pulse shaper of a design similar to those described by Weiner.[90] The shaper uses a pair of SF-10 prisms as the dispersion elements and 0.4 m cylindrical mirrors for collimation. A

[b] Reproduced in part with permission from I. Pastirk, J.M. Dela Cruz, K.A. Walowicz, V.V. Lozovoy, M. Dantus, Selective two-photon microscopy with shaped femtosecond pulses, *Opt. Express* 2003, **11**, 1695-1701. Copyright 2003 Optical Society of America.

schematic of the experiment is shown in Figure 3.6. Phase modulation is introduced by a computer-controlled SLM (SLM-256, CRI Inc.), located at the Fourier plane of the shaper setup. For the experiments shown here, the pulses were centered near 800 nm. The spectral phase of each pulse was calibrated using the MIIPS method, first to obtain TL pulses and then to introduce the desired phase.[97, 111] The spectral phase function used for this experiment is given by Equation 1.1.

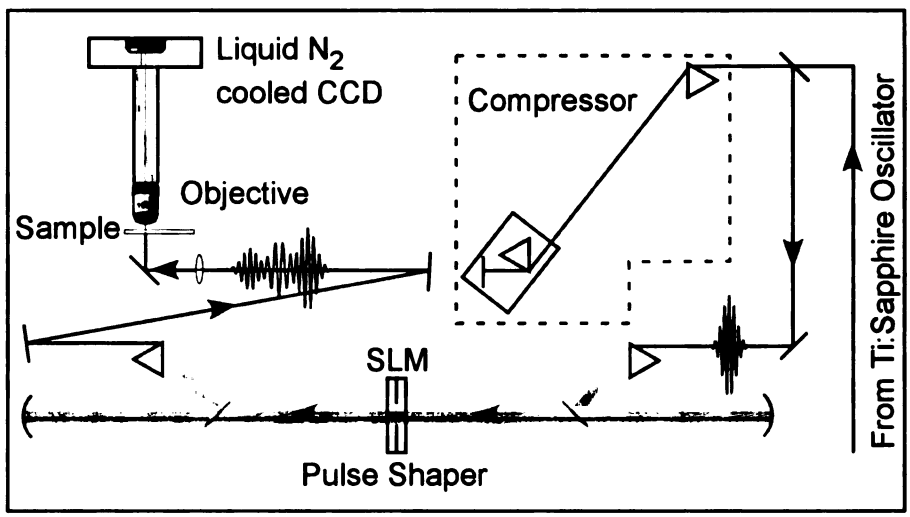

Figure 3.6. Schematic experimental setup for selective two-photon microscopy. Femtosecond laser pulses are compressed and sent to the pulse shaper. The modulated beam is then focused on the microscope slide with the specimen. The two-photon induced fluorescence is collected by a microscope objective and imaged on a CCD.

The shaped laser pulses, with energy of 0.2-1 nJ per pulse and 87 MHz repetition rate were focused mildly, to a spot size of ~ 200 microns in diameter, on the different samples. Two-photon induced fluorescence was collected by an infinity corrected apochromatic microscope objective (APO 100X, Mitutoyo) and imaged into a liquid nitrogen cooled charge-coupled device (CCD) detector using an InfiniTube (Proximity Series, Infinity Photo-Optical). Experiments were carried out on three different types of

samples. The first sample was prepared with acrylonitrile-vinylidene chloride polymer (1 mL) cured in acidic (pH 6) or basic (pH 10) buffered conditions and stained with the pH-sensitive fluorescent probe HPTS (10^{-3}M) (Sigma-Aldrich). Both acidic and basic HPTS mixtures were smeared to an approximate thickness of 0.07±0.03 mm on contiguous regions of a microscope glass slide, and then allowed to cure for 20 minutes. Some mixing of the solvent water may have occurred at the interface between the two regions. Local changes in the fluorescence intensity observed for TL pulses may reflect changes in the local sample thickness. The second sample consists of pieces of polymethylmethacrylate (PMMA) doped with coumarin (C540) and rhodamine (R6G) fluorescent probes[112] (10^{-4}M). The third sample consists of a mixture of 10 μm blue and 15 μm green fluorescent FluoSpheres (Molecular Probes). The images were captured without optical filters in the collection optics or post image manipulation. The background, detector counts when the laser is off, was subtracted.

3.2.3 Results

Figure 3.7A shows an image of acidic and basic HPTS solutions obtained with TL pulses. The spectrum of the pulse and the spectral phase (flat line) are shown in the middle panel. The right panel shows the absorption spectra of HPTS under acidic and basic conditions, including the laser spectrum corresponding to $E^2(t)$. Figure 3.7B shows an image obtained with laser pulses optimally shaped for selective excitation of HPTS under acidic environment. The spectral phase used to acquire this image is shown in the middle panel; the spectrum corresponding to this phase is shown in the right. Figure 3.7C shows an image obtained with laser pulses optimally shaped for selective excitation of

HPT

the

cont

in E

Fig
mi
sid
pu
pu
HP
las
wit
env
The
whe
pulse
locat
in a
phot
photo
d.

fluoresc

HPTS in a basic environment. The spectral phase used to acquire this image is shown in the middle panel; the right panel shows the spectrum corresponding to this phase. The contrast ratio between pH 10/pH 6 in these images varies from 1:1 in Figure 3.7A to 1:10 in B to 64:1 in C.

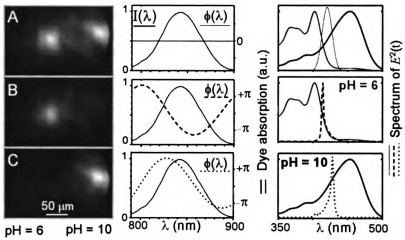

Figure 3.7. Experimental demonstration of pH-sensitive selective two-photon microscopy. The sample being imaged has an acidic (left side, pH 6) and a basic (right side, pH 10) region, both labeled with HPTS. A. Image of the sample obtained with TL pulses. The spectrum of the 21 fs laser pulses centered at 842 nm and the phase of the pulse across the spectrum are shown in the middle diagram. The absorption spectra of HPTS under acidic (dark gray) and basic (black) conditions are shown together with the laser spectrum corresponding to $E^2(t)$. B. Image of the same sample and location obtained with pulses that have been optimized for selective excitation of HPTS in an acidic micro-environment. Notice that only the left region shows significant two-photon excitation. The spectral phase function used for this experiment is given by $\phi(\Omega)=\alpha\cos(\gamma\Omega-\delta)$, where Ω is the frequency detuning measured from the center wavelength of the laser pulse. For this image $\alpha = 1.5\pi$, $\gamma = 20$ fs, and $\delta = 0.75\pi$. C. Image of the same sample and location obtained with pulses that have been optimized for selective excitation of HPTS in a basic micro-environment. Notice that only the right region shows significant two-photon excitation. For this image $\alpha = 1.5\pi$, $\gamma = 20$ fs, and $\delta = 0.25\pi$. Selective two-photon excitation from the two pH regions in the sample is observed at specific values of δ.

The experimental results in Figure 3.8 show selective excitation of different fluorescent probes. Figure 3.8A shows the data obtained using TL pulses. The two

imaged pieces of PMMA exhibit similar amounts of two-photon LIF. When the spectral phase of the pulse is modified to optimize selective excitation of the C540-doped sample, we observe that only the top fragment fluoresces, as shown in Figure 3.8B. When the spectral phase of the pulse is optimized for selective excitation of the R6G-doped sample, Figure 3.8C, we observe strong fluorescence from the bottom fragment while the other side, containing the C540 probe, does not fluoresce. Note that the spectrum and intensity of the laser remain constant during the experiment for all three cases. The only change occurring is the subtle modulation of the spectral phase of the pulse, which controls MII.[65, 66] Contrast ratios (I_{R6G}/I_{C540}) (normalized intensities corrected to background) range from 1:9 for pulses optimized for C540 to 8:1 for pulses optimized for R6G. Selective multiphoton excitation minimizes the cross talk between different fluorescent probes and does not require the use of multiple filters and detectors for imaging.

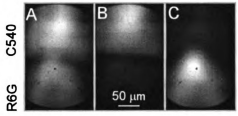

Figure 3.8. Selective two-photon microscopy of pieces of PMMA doped with different fluorescent probes. A. Image showing two-photon induced fluorescence from both pieces: C540 doped PMMA (top) and R6G doped PMMA (bottom), obtained with 17 fs TL pulses centered at 790 nm. B. Image obtained with pulses optimized for selective C540 excitation. For this image the pulses were shaped with a sinusoidal function with δ=0.31π. C. Image obtained with pulses optimized for selective R6G excitation. For this image the pulses were shaped with a sinusoidal function with δ=0.74π. Selective two-photon excitation from the two PMMA pieces is observed at specific values of δ.

The previous experiment showed selective two-photon excitation of different probe molecules. To further illustrate the potential of coherent control for functional

imaging we assessed the possibility of selectively exciting blue- and green-fluorescent microspheres, which are typically used for targeted staining of biological samples. Fluorescence observed from these microspheres is shown in Figure 3.9. The top part of the image shows the green-fluorescent microsphere (15 μm diameter) which has an absorption maximum at 450 nm, while the bottom part represents the blue-fluorescent microsphere (10 μm diameter) with an absorption maximum at 365 nm. The image in Figure 3.9A was acquired with TL pulses. Under these conditions, large two-photon induced fluorescence signal is observed from both spheres. For the image in Figure 3.9B, the phase of the pulses was modulated such that the intensity of fluorescence from the blue microsphere is maximized while minimizing fluorescence from the green microsphere. For the image in Figure 3.9C, we modulated the phase of the pulses such that the fluorescence from the green microsphere is maximized and that of the blue one minimized. The observed contrast ratios (I_{BLUE}/I_{GREEN}) are 1:3 and 4:1 for the different phases.

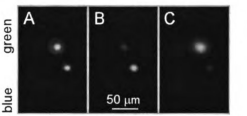

Figure 3.9. Selective two-photon microscopy of 10 μm blue and 15 μm green fluorescent polystyrene microspheres. A. Image showing two-photon induced fluorescence from both microspheres, obtained with 15 fs TL pulses centered at 790 nm. B. Image obtained with pulses optimized for selective excitation of the blue microsphere. For this image the pulses were shaped with a sinusoidal phase with δ=0.75π. C. Image obtained with pulses optimized for selective excitation of the green microsphere. For this image the pulses were shaped with a sinusoidal phase with δ=1.25π. Selective two-photon excitation from the two microspheres is observed at specific values of δ.

3.2.4 Discussion

Selective excitation with significant contrast ratios has been achieved here by optimizing the overlap between the power spectrum of $E^2(t)$ and the two-photon absorption spectrum.[65, 66] The addition of a computer-controlled pulse shaper to the multiphoton microscope provides a number of important advantages. First, the pulse shaper can be used to compensate unwanted phase distortions at the sample. Linear chirp, for example, has been shown to reduce signal intensity in two-photon microscopy.[113]. With a pulse shaper, linear, quadratic, cubic and higher order chirp can be compensated to obtain the most efficient excitation.[97] Second, the pulse shaper can be used to control the output spectrum of the laser pulses by amplitude modulation. Here, for example, we used pulses centered at 790 or at 840 nm. Third, the pulse shaper can be used for selective probe excitation. Because the spectrum of the laser remains constant, phase modulation does not affect one photon processes such as absorption, reflection and scattering. Selective excitation minimizes possible cross talk between different fluorescent probes in the sample. Finally, the pulse shaper can be used to prevent three-photon and higher order nonlinear optical processes such as continuum generation. Higher order processes usually lead to sample degradation, and in the case of living samples, to DNA damage.[114, 115] Suppression of three-photon transitions of four orders of magnitude has been achieved using the MII method[66] and this suppression can be coupled with optimization of two-photon signal from living specimens.

Recently Ogilvie et. al. adopted the sinusoidal phase modulation approach towards selective two-photon excitation microscopy to image live eGFP (green fluorescent protein) labeled Drosophila embryos. Pulse shaping, in this case, allowed

selectively excitation of eGFP or of endogenous fluorescence.[116] The ability to separate endogenous two-photon induced fluorescence, which is ubiquitous in biological samples, is an important achievement that greatly enhanced the contrast of the obtained images.

Although selective excitation can be carried out by wavelength tuning of narrower-bandwidth lasers, the more practical approach of modulating the phase of a broad-pulse femtosecond laser has a number of advantages. In wavelength tuning, spectral phase measurements at every desired excitation wavelength are required and movement of optics causes problems when trying to overlap images obtained at different wavelengths (a pixel registration problem). By phase modulation, the whole process of spectral phase measurement and compensation is carried out in advance and excitation at different wavelengths within the bandwidth of the ultrashort pulse is achieved, requiring no physical movement of optical materials.

3.2.5 Conclusion

We have demonstrated selective two-photon microscopy of fluorescent probe molecules using phase-modulated pulses as short as 15 fs. This method can be used to selectively excite either different probe molecules or identical probe molecules in different environments. In addition, this method can be used for selective excitation of luminescent probes such as quantum dots,[117] metallic nanoparticles, and single molecules.[118] The same principle can be extended to achieve functional imaging of semiconductor microchips by two-photon laser induced conductivity.[119, 120] Having a pulse shaper for multiphoton microscopy provides the flexibility of selective probe excitation or maximum signal enhancement by controlled modulation of the spectral

phase of the femtosecond pulses. Even for fluorescent labels with very similar absorption spectra, pulse shaping has the capability of selective excitation.[45] This level of selectivity and enhancement can be adapted to different modes of two-photon and three-photon microscopy.[121-124]

CHAPTER 4

COHERENT LASER CONTROL IN IMAGING

For many years, lasers in the medical field were seen primarily as surgical tools for the ablation, cutting, or coagulation of tissue. But in the last decade some of the most successful medical-laser applications have been noninvasive (e.g. skin rejuvenation, hair removal, PDT, low-level laser therapy, and, more recently, laser treatments of psoriasis, acne, cellulite, and dental bacteria). In addition, laser-based diagnostic tools such as optical coherence tomography[125] and multiphoton microscopy[92] have gained acceptance within the medical community for noninvasive imaging, while optical sensors are finding a place in the detection and monitoring of chronic and other diseases. Recent research efforts have focused on making medical diagnosis cheaper, faster and more effective by developing new physics-based imaging techniques and by using powerful computers to process and analyze biomedical information. New technological developments are being increasingly driven by the needs of the medical profession, and optics is playing an increasingly important role.

Optical spectroscopy is a standard tool in laboratory analysis that is used to detect and monitor the concentration of substances, such as oxygen, by measuring the absorption, fluorescence or Raman spectra. But performing spectroscopy in biological tissue is very different from making measurements on a solution in a test tube. Quantitative optical measurements in biological tissue are extremely difficult because tissue scatters light strongly, typically within 100 μm. Scattering within tissue results from macroscopic and microscopic constituents such as cellular membranes, refractive

index mismatching between intra- and extracellular fluids, mitochondria, ribosomes and fat globules. This limitation has prevented the widespread application of optics in clinical medicine.

If the problems associated with scattering can be overcome, optical imaging could provide a cheaper technology that would allow patients to be screened for diseases such as skin and breast cancer, osteoarthritis and diabetes, as well as revealing much more about the working processes of organs, including the brain.

In this chapter, the possibility of working around the impediment of tissue scattering to selectively excite molecules based on their chemical microenvironment is presented (Section 4.1). The sensitivity of nonlinear imaging methods to the spectral phase of the pulses is highlighted; controlling this phase can lead to significant improvements and new possibilities in functional biomedical imaging (Section 4.4). The importance of delivering accurate pulses to the sample for imaging, identification and possibly therapeutic purposes is also demonstrated (Sections 4.2 and 4.3). In addition, the advantage of spectral phase modulation in terms of minimizing the damaging effects of three-photon excitation on biological samples is discussed (Section 4.5).

4.1 Phase Modulation through Scattering Tissue[c]

4.1.1. Introduction

In the last decade a number of reports have demonstrated controlled excitation of atoms and even the controlled photochemistry of isolated molecules.[32, 37, 59] More recently these reports have included large organic molecules in solution.[12, 45, 47, 51] Phase shaped femtosecond pulses[90] have the potential for influencing the quantum-mechanical laser-molecule interactions, thereby controlling population transfer between different electronic states of large organic molecules.[11, 91, 95, 126-129] The benefits of coherent laser control of large organic molecules are beginning to permeate to the biological field through selective two-photon chemical microenvironment probing and microscopy. Here we question if coherent control methods, in particular phase shaping, can be used in situations where the laser transmits through scattering biological tissue.

Coherent control depends on the interference among multiple excitation pathways; this interference is controlled by modulating the phase of the excitation field. Control schemes therefore depend on the precise phase modulation of the laser pulses, which, through constructive and/or destructive interference, optimize the desired outcome and minimize other pathways. The dependence of coherent control on the accurate phase structure of the pulse, however, suggests that these approaches would not be applicable to situations involving transmission through scattering media.

This section presents a study that evaluates the possibility of using coherent control as the laser transmits through scattering tissue. In particular, the ability to achieve selective two-photon excitation of a pH-sensitive probe molecule using phase-shaped

[c] Reproduced in part with permission from J.M. Dela Cruz, I. Pastirk, M. Comstock, M. Dantus, Multiphoton intrapulse interference 8. Coherent control through scattering tissue, *Opt. Express* 2004, **12**, 4144-4149. Copyright 2004 Optical Society of America.

femtosecond pulses in the presence and absence of scattering tissue is evaluated. The motivation for the experiment is that coherent control schemes could enhance methods such as two-photon imaging, which has provided images with higher resolution, lower background scattering, and better sample penetration.[92, 130] Selective two-photon excitation could be used to help localize two-photon induced PDT[131], and restrict its therapeutic effects to diseased tissue, while leaving surrounding tissue undamaged.

4.1.2 Experimental Section

The setup for the experiment is shown schematically in Figure 4.1. The experiment was carried out using a Ti:S oscillator (K&M Labs) laser system. The laser spectrum was centered at about 830 nm, with a bandwidth of 90 nm (FWHM), corresponding to 11 fs pulse duration. The average energy per pulse entering the objective was 1 nJ. The laser pulses were calibrated at the sample, after the objective, using the MIIPS method.[97] The spectral phase functions used for this experiment are based on binary phase shaping (BPS), a method that assigns phase values of zero or π to frequency components of the pulse, and is ideally suited for controlling multiphoton transitions.[77] Optimization of the phase structure was achieved by accounting for the excitation spectra of probe molecule in acidic and basic environments, the characteristics of the laser pulse, and MII.[65, 66] A learning algorithm was then used to optimize excitation—maximizing the excitation of one form of the probe molecule while minimizing excitation of the other form of the probe, HPTS fluorophore in acidic or basic solution, respectively. Two optimized BP functions were introduced into the pulse shaper. The sample was scanned in the focal plane of the laser, focused by a 5x long-

working distance objective. The capillary tubes (1 mm i.d.) were filled with 10^{-3} M HPTS aqueous pH6 and pH10 buffered solutions. A fifth tube was filled with water to serve as a control to demonstrate the absence of signal due to scattered light. The tubes were placed side by side and oriented vertically in a 2 mm quartz cell filled with water. The fluorescence was focused onto a spectrometer with detection wavelength set at 515 nm (the emission wavelength of HPTS) where it was detected and averaged point by point. A 1.5-2.0 mm slice of biological tissue (raw breast of chicken) was placed between the front face of the cell and a microscope slide. The tissue was slightly compressed to a uniform thickness of about 1 mm. A drop of Nujol was used to reduce aberrations caused by index of refraction mismatch. Approximately, 1 mm of tissue is equivalent to 10 scattering lengths.

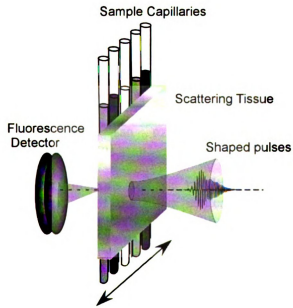

Figure 4.1. Experimental setup. The shaped laser pulses impinge on the sample where fluorescence is detected in the forward direction. The sample, with or without scattering tissue, is scanned in the focal plane of the laser while the two-photon induced fluorescence is detected at each point.

The spectral phase for TL pulses and the BP functions that were used to enhance excitation of HPTS in an acidic or a basic environment are shown in Figure 4.2. The SHG spectrum obtained from a thin nonlinear optical crystal, also shown in Figure 4.2, provides a diagnostic test of the effects of phase modulation. Unlike the TL pulses, the shaped pulses preferentially excite one of the two different pH solutions. The spectrum of the laser pulse does not change upon phase modulation, only its potential to cause two-photon excitation or generate second harmonic radiation.[65, 66] The change in the spectrum is caused by destructive interference induced by the phase mask.[77]

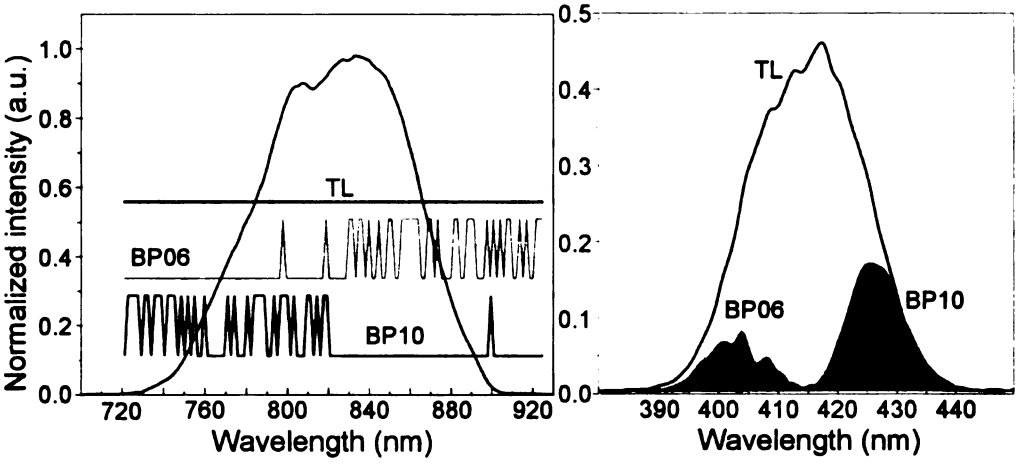

Figure 4.2. Optimized phase functions and the resulting SHG. The panel on the left shows the fundamental spectrum of the pulse centered near 830 nm and the three different pulses evaluated, TL with a flat spectral phase, and shaped pulses optimized for acidic (BP06) and for basic excitation (BP10). The panel on the right shows the experimental SHG spectrum obtained from TL pulses and SHG spectra obtained when the phase functions BP06 and BP10 were introduced by the pulse shaper. Notice that BP06 suppresses SHG at long wavelengths and BP10 suppresses SHG at short wavelengths.

4.1.3 Results

When TL pulses were used, large two-photon induced fluorescence signals at 515 nm, the peak emission wavelength of HPTS in both pH solutions, were observed. The

contrast that could be achieved was tested by recording the signal observed when the laser was focused on each of the two HPTS solutions. This test was carried out using two capillary tubes and no scattering tissue. As can be seen in Figure 4.3, BP06 preferentially excites the pH6 solution, and BP10 preferentially excites the pH10 solution.

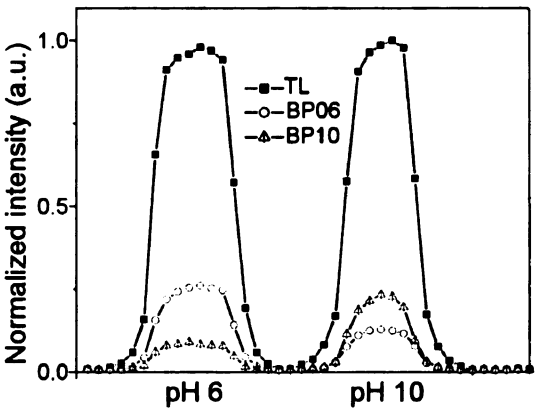

Figure 4.3. Fluorescence signal obtained from two capillaries containing HPTS in buffered solutions. The signal was obtained after excitation with TL and shaped pulses.

Figure 4.4 shows a plot of the signal obtained from the setup indicated in Figure 4.1 with and without scattering tissue. The signal from TL pulses was multiplied by –1 and plotted as a function of position. The peak height obtained from both acidic and basic solutions is essentially the same. The small variations are caused by small shifts in the position of the focal plane. The capillary containing pure water gives no signal as expected. The difference signal obtained from the two-photon fluorescence signals (optimized for acid pH minus optimized for alkaline pH) obtained using the two masks is shown in Figure 4.4 as open circles. For this measurement the signal obtained for pH 10 samples was normalized to one. Notice that the contrast, a measure of efficiency of coherent control, is quite high. In the absence of tissue the contrast ratio is 10:1. More importantly the contrast is found to survive the presence of ~ 1 mm of tissue. The

contrast obtained (6:1) has been essentially maintained, although the overall signal decreases exponentially with the tissue thickness.

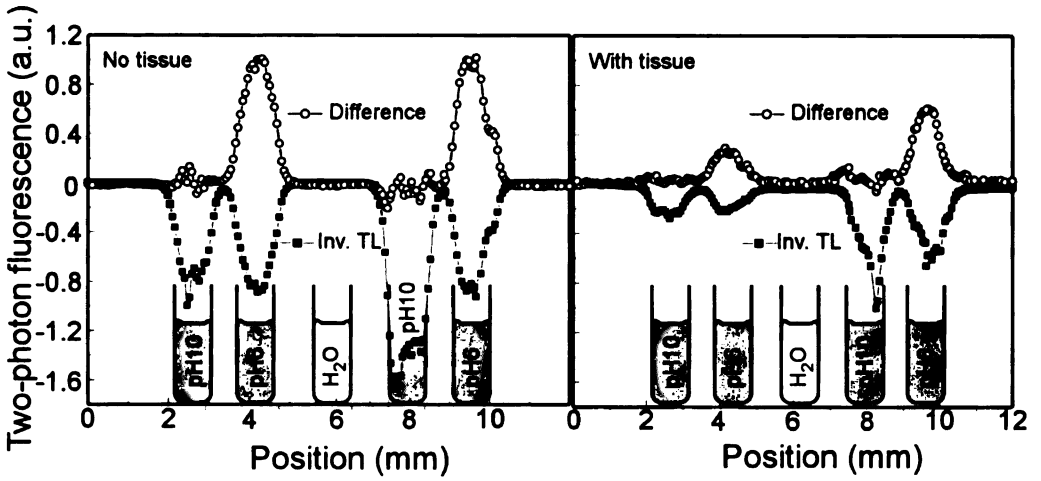

Figure 4.4. Line scan of sample without (left) and with (right) tissue. The sample, consisting of 5 capillary tubes containing acidic or basic HPTS and water (control), was scanned in the x direction. Experimental results obtained with TL (black dots) pulses are plotted in the negative axes. Difference plots obtained from the shaped laser pulses (open circles) are plotted in the positive axes. Notice that shaped laser pulses are capable of selective excitation even when the laser transmits through scattering tissue.

4.1.4 Discussion

The goal of this research was to establish if phase-shaped pulse strategies designed to control the excitation and chemistry of molecules survive transmission of the laser through scattering tissue. The results of our experiment indicate that the ballistic photons, which are the ones responsible for the two-photon fluorescence detected, retain the shaped pulse characteristics required for selective excitation. This was confirmed by experimentally measuring the SHG spectrum of the shaped pulses before and after transmission through biological tissue. Figure 4.5 shows the SHG spectrum of TL pulses and the SHG spectrum of shaped (BP06) pulses with and without tissue. The result obtained with tissue gave a much weaker signal that was multiplied by a factor of 20 for the illustration. Note that the SHG spectrum of the shaped pulses suffered little or no

change other than attenuation. SHG and two-photon excitation are achieved only by the coherent ballistic photons. This is why selective two-photon excitation is possible through the tissue.

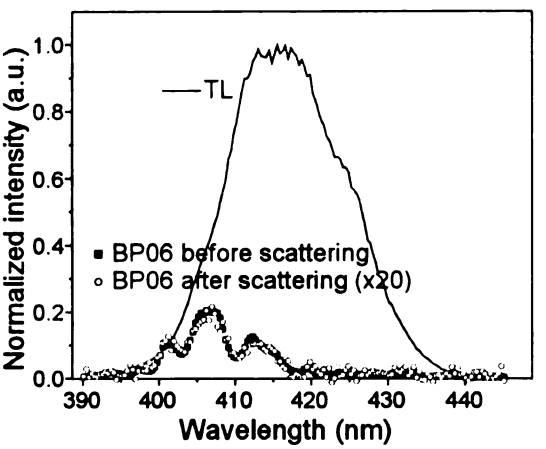

Figure 4.5. SHG spectra for TL and for shaped pulses (BP06) in the presence (open circles, intensity multiplied by 20) and absence (black squares) of biological tissue.

4.1.5 Conclusion

Coherent control methods can be used to improve biomedical applications of laser technology that presently use TL femtosecond pulses. In particular, optical coherence tomography, PDT, and functional imaging stand to gain the most from the results observed because coherent control should be able to provide better contrast and allow the use of more intense laser pulses while damage to healthy tissue is minimized by intrapulse interference. This method is useful for depths up to 3 mm. Delivery of the beam to internal organs could be achieved using optical fibers. For some imaging techniques, it isn't possible to collect fluorescent light in the forward direction, as done here, and one must collect fluorescent photons in the backward direction (epifluorescence). The method used here could be implemented in that modality; an

inverted microscope could be used for this purpose. Bringing these experiments to actual biomedical applications is a goal we hope to achieve in the future.

4.2 Phase Compensation of Imaging Objectives[d]

4.2.1 Introduction

The nonlinear properties of a pulse are very sensitive to spectral phase distortions that are either inherent to the laser system or are introduced by lenses, optical fibers, mirrors, or microscope objectives. Eliminating these distortions is especially critical in cases where reproducibility is an important criterion for femtosecond laser applicability. These distortions need to be corrected to ensure the fast progress of femtosecond laser excitation in biomedical imaging applications.

One of the greatest obstacles to fully developing the promising technique of multiphoton imaging is the significant amount of phase distortion introduced by high numerical aperture (NA) microscope objectives. To date, the characterization of such distortions has been accomplished for sub-10 fs pulses in objectives with NA up to 0.85,[132] and for up to 1.30 NA objectives if longer pulses are used.[133-136] Compensation of the quadratic term of the characterized distortions was accomplished in some cases through precompensation. However, higher order phase distortions, introduced by the objectives and even by the prisms necessary to precompensate for the quadratic phase distortions, cannot be corrected by these methods, nor can the phase distortions be quantified. In this section, the ability of MIIPS to successfully quantify and compensate

[d] Reproduced in part with permission from B. Xu, J.M. Gunn, J.M. Dela Cruz, V.V. Lozovoy, M. Dantus, Quantitative investigation of the MIIPS method for simultaneous phase measurement and compensation of femtosecond laser pulses. *J.Opt. Soc. Am. B* 2006, **23**, 750-759. Copyright 2006 Optical Society of America.

for all orders of arbitrary phase distortions introduced into a sub-10 fs pulse by high NA microscope objectives is presented.

4.2.2 Experimental Section

A periscope was used to bring the laser beam (800 nm, 10 fs, 250 mW average power) into the rear port of a Nikon TE2000-U inverted microscope. The beam was reflected upward through the objective and focused onto an SHG crystal. Three objectives were tested: a Nikon Plan Fluor ELWD 20x/0.45 NA objective, a Nikon Plan Fluor ELWD 40x/0.60 NA objective, and a Nikon Plan Apo TIRF oil immersion 60x/1.45 NA objective (Nikon immersion oil, Type NF). Phase characterization and compensation were carried out with MIIPS. To test the viability of pulse characterization and compensation on imaging, a mouse kidney section (FluoCells® prepared slide #3 mouse kidney section with Alexa Fluor® 488 WGA, Alexa Fluor® 568 phalloidin, DAPI) was imaged with either phase-corrected TL pulses or with uncompensated pulses.

4.2.3 Results and Discussion

MIIPS alone was sufficient to compensate for the phase distortions introduced by 20x/0.45 NA and 40x/0.60 NA microscope objectives. To allow for the best compensation of higher order phase distortion introduced by the 60x/1.45 NA objective, a pair of SF10 prisms was used to reduce the quadratic phase contributions ($\sim 10^4$ fs^2).

Figure 4.6 shows the compensation results for the 1.45 NA objective. In both panels, the solid line shows the average phase residue from five independent measurements. The errors bars show the standard deviation for every fifth data point.

The top panel shows the full set of acquired data; the lower panel shows the same data over the FWHM of the fundamental laser spectrum with a reduced scale. Note that the phase is compensated to within 0.1 rad over the entire bandwidth of the pulse (770-860 nm), indicating that the distortions introduced by high NA objectives are well compensated over this range. The extremely narrow standard deviation observed in the reduced range provides evidence of a very high degree of reproducibility of the MIIPS method, even when highly dispersive materials are utilized. The statistical phase error for the 60x/1.45 NA objective was calculated to be 0.026 rad over the full range of data, where the uncompensated phase distortion was ~40 rad. Considering the significant degree of distortion introduced by this high NA objective (see inset of Figure 4.6), the precision by which phase is retrieved by MIIPS is excellent.

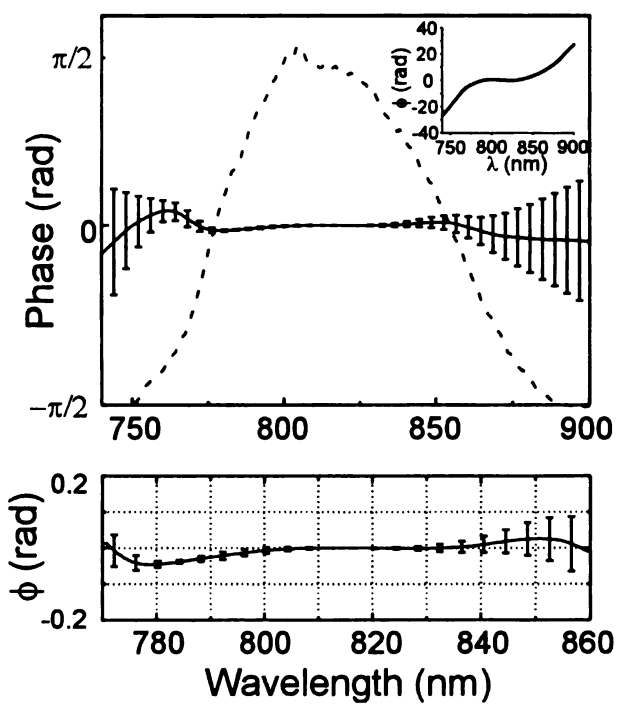

Figure 4.6. Compensation of spectral phase distortions caused by a 60x/1.45 NA objective. The error bars indicate ± 1 standard deviation. The upper panel shows the full range of data, while the lower panel shows the same data over the FWHM of the pulse, on a reduced scale. The inset (top panel) shows the phase extracted before compensation with MIIPS.

The images shown in Figure 4.7 demonstrate the importance of spectral phase compensation. The compensation, and any subsequent application of phase, is accomplished through the introduction of computer instructions. The laser beam is never tweaked or scanned, reducing the potential for error and the ease of use, as both actions require a significantly higher level of expertise and may result in changes of the phase distortions and, in some cases, diminished registration in multiple images. No fluorescence wavelength filters were used to separate contributions from the fluorescent labels in the sample. Comparing between the two images, it is clear that phase distortion leads to a significant loss of signal (Figure 4.7, right) that cannot be compensated simply by increasing the laser power. This is because phase distortions cause changes in the wavelength region where multiphoton excitation takes place.[65, 66] The benefits of pulse characterization and compensation are realized with the improvement in image quality (Figure 4.7, left).[137]

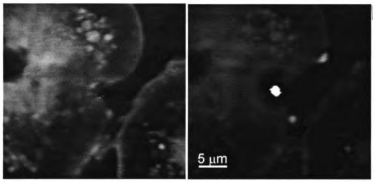

Figure 4.7. Image quality improvement with spectral phase compensation. Left: fluorescence image of mouse kidney using femtosecond laser pulses with spectral phase deformations corrected. Right: fluorescence image of the same section of the sample when pulses are uncompensated (no spectral phase correction). Both images were normalized to the same maximum intensity level. Image size is 30 μm x 30 μm.

4.3 Phase Compensation through Scattering Tissue[c]

4.3.1 Introduction

When a laser beam transmits through a scattering medium like biological tissue, the coherent component of the electric field, although maintaining its directionality, degrades exponentially with tissue depth. This occurs as a result of the heterogeneous nature of tissue structure. Although femtosecond lasers have increasingly been used for medical diagnostics and therapeutics as well as for imaging applications, an underlying uncertainty exists as to the spectral phase distortions the laser pulse experiences as it propagates through several scattering lengths of tissue. In this section, the ability of the MIIPS method to measure spectral phase deformations caused by transmission through scattering biological tissue is investigated.

4.3.2 Experimental Section

The procedure involved measuring phase distortions inherent in a sub-10 fs laser pulse, correcting for these distortions to obtain TL pulses, and then comparing the spectral phase obtained when the laser transmits through a 500-μm slice of raw chicken breast tissue or through a similar thickness of glass. Preliminary experiments using a variable scattering medium (skim milk in water) indicated that the retrieved spectral phases had very little dependence, other than on the overall intensity, on the degree of scattering. This is indicative of the ability of the coherent component of the laser or the

[c] Reproduced in part with permission from B. Xu, J.M. Gunn, J.M. Dela Cruz, V.V. Lozovoy, M. Dantus, Quantitative investigation of the MIIPS method for simultaneous phase measurement and compensation of femtosecond laser pulses. *J.Opt. Soc. Am. B* 2006, **23**, 750-759. Copyright 2006 Optical Society of America.

ballistic photons to maintain phase information as the laser penetrates a turbid, scattering medium.

4.3.3 Results and Discussion

Our results with tissue (Figure 4.8) confirm that despite the presence of inhomogeneities that significantly affect the coherence of a femtosecond laser pulse, phase distortion is minimal. As expected, a reduction in signal to noise ratio resulting from the exponential decay of ballistic photons as the pulse transmits through several scattering lengths of tissue was observed. Notwithstanding this limitation, phase information is still comparable to that obtained when light goes through an optical medium like glass. Figure 4.8A and B show the MIIPS traces obtained for glass and tissue samples, respectively. The presence of tissue slightly decreases the range of wavelengths that can be compensated by MIIPS, but phase correction is nonetheless achieved. Figure 4.8C shows the phase residue, averaged over five trials, of the pulse as it went through glass and tissue. Note that the phase is compensated to within 0.02 rad over the entire FWHM of the pulse. With additional iterations, MIIPS can fully compensate for distortions introduced by a scattering medium. More significantly, the method characterizes and corrects for distortions at the position of the sample. Consequently, the phase of a pulse can now be known at the position of the sample, even under poor signal to noise conditions, without autocorrelation or interferometry. Simulations[138] show that even for signal to noise ratios as low as one, it is possible to retrieve the spectral phase with high precision by smoothing the two-dimensional MIIPS data before analysis. The good resistance to noise and the fact that it is independent of mode quality are additional significant advantages of the MIIPS method.

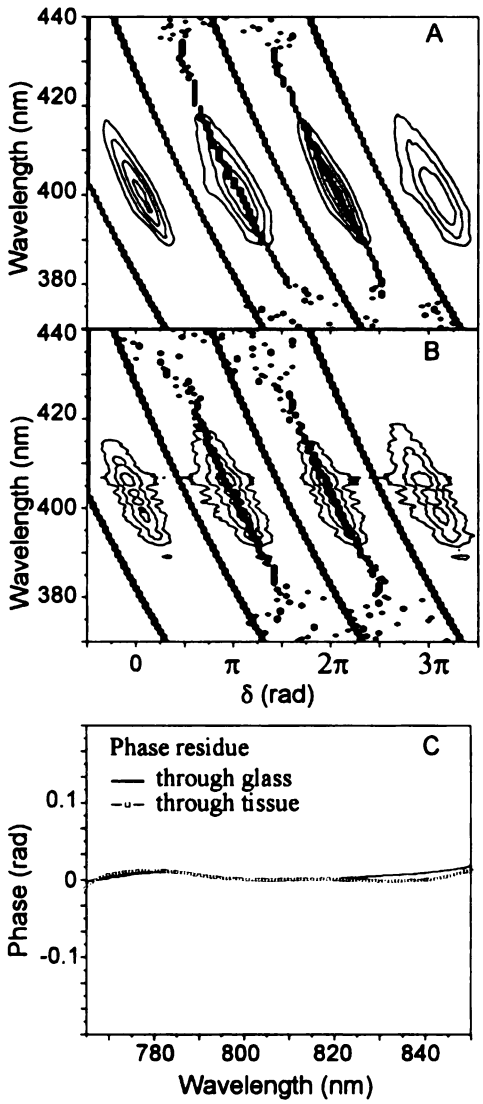

Figure 4.8. MIIPS measurement through scattering biological tissue. Panels A and B show MIIPS traces without and with tissue, respectively. While the overall signal to noise ratio is significantly decreased, similar phase information is obtained (C).

4.4 Functional Imaging with Shaped Laser Pulses[f]

4.4.1 Introduction

Interest in coherent laser control has grown steadily, given its potential for influencing quantum-mechanical laser–molecule interactions.[11, 91, 95, 126-129] With the use of pulse shapers and computer learning algorithms, scientists have controlled the excitation of isolated atoms and molecules[32, 37, 139] and, more recently, large molecules in solution.[12, 45, 51] Population transfer between different electronic states of large organic molecules can be maximized or minimized through manipulation of the spectral phase of ultrashort laser pulses.[65, 66] The benefits of coherent laser control of large organic molecules can be extended to the biological field through selective two-photon chemical microenvironment probing[111] and microscopy.[140] Control of laser-matter interactions could revolutionize biomedical applications. Coherent control schemes, for example, could enhance methods such as two-photon imaging[92, 130] which has provided higher resolution, lower background scattering, and better sample penetration than traditional techniques. Selective two-photon excitation would be desirable for distinguishing healthy from cancerous tissue based on differences in their chemical properties such as pH, or for activating a PDT agent only when it is absorbed by cancer cells by using two-photon activated PDT.[131] These improvements would be possible only if shaped laser pulses maintain their unique properties as they transmit through scattering biological tissue.

Coherent control of laser-induced processes is based on the quantum interference among multiple excitation pathways.[127] Progress in this field has been fueled by advances in pulse shaping technology, allowing control of the phase and amplitude across

[f] Reproduced in part with permission from J.M. Dela Cruz, I. Pastirk, M. Comstock, M. Dantus, Use of coherent control methods through scattering biological tissue to achieve functional imaging. *P. Natl. Acad. Sci. USA* 2004, **101**, 16996-17001. Copyright 2004 by The National Academy of Sciences of the USA.

the bandwidth of ultrashort laser pulses.[90] Control schemes depend on introducing intricate phase structures on the laser pulses that, by means of constructive and/or destructive interference, optimize the desired outcome and minimize other pathways. This dependence on the accurate phase structure of the pulse suggests that these methods may not be applicable to situations involving transmission through scattering biological tissue.

When a laser beam passes through a turbid scattering medium, its coherence (a property of waves defined as the degree with which waves are in step with each other) degrades exponentially as $I_{coherent} = I_0 \exp(-\mu_e x)$, where $1/\mu_e$ is the scattering length of the medium and x is the sample thickness. The transformations of the pulse and the exponential loss of coherence are shown schematically in Figure 4.9. The coherent component of the electric field, which is sometimes referred to as the ballistic photons,[141] propagates through and maintains its directionality. The incoherent component, or diffusive photons (shaded broad region in Figure 4.9), loses its directionality because of scattering and can no longer be used for high-resolution multiphoton imaging.[142] In this context, one can also identify an intermediate component referred to as the snake photons, whose degree of coherence is still debated.[143] Scattering of a laser in biological tissue results from the spatial variations of the sample caused by the different cellular structures and substructures with different indices of refraction, causing changes in the directionality of portions of the beam and introducing various delays.

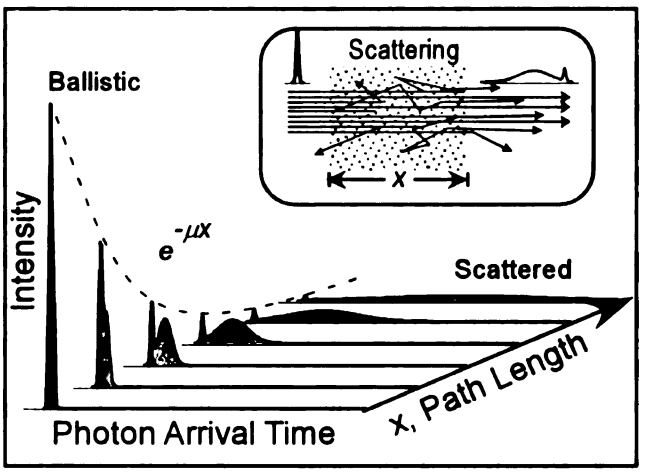

Figure 4.9. Coherence degradation and pulse transformation as a function of scattering path length. As a short pulse of light enters a scattering medium, coherent or ballistic photons (sharp feature) are lost exponentially. The scattered photons (shaded broad feature), which lag in time, lose their coherence and are randomly delayed.

Coherent control of nonlinear optical processes based on phase-only shaping can be achieved in scattering biological tissue. To verify this hypothesis, selective two-photon excitation of a pH-sensitive probe molecule, HPTS, was optimized using phase-shaped femtosecond pulses. Optimization of the laser-pulse phase structure was based on the spectroscopic changes exhibited by HPTS in acidic and alkaline environments. Figure 4.10 shows the spectroscopy and chemical structure of HPTS. The hydroxylic proton has a pKa of ~7.5 and is promptly lost in response to an increase in the pH of its local environment. The absorption maximum of the protonated species changes from 400 to 450 nm upon deprotonation (Figure 4.10). Interestingly, the fluorescence maximum is 515 nm in both acidic and alkaline pH, because the pKa of the excited state molecule is much smaller, leading to fast deprotonation in all but highly acidic environments[99, 100] Laser-pulse optimization depends on the characteristics of the laser pulse (central wavelength, spectral phase, and pulse duration) and on MII[65, 66] which leads to the suppression of two-photon excitation at certain wavelengths. An evolutionary learning

algorithm[129] was used to obtain the greatest excitation selectivity between the two HPTS species (acidic and alkaline). The selectivity achieved by two optimal phases during functional imaging with and without the presence of tissue was tested. These phases, BP06 and BP10, maximize two-photon excitation of pH 6 or 10 solutions, respectively. This section presents results that confirm selective two-photon excitation after a beam propagates through biological tissue. To substantiate these results, we measured the rate of coherence loss with tissue depth, characterized the spectral phase of the pulses after they were transmitted through biological tissue, and characterized the signal intensity as a function of scattering and the resolution expected for possible biomedical applications of laser control.

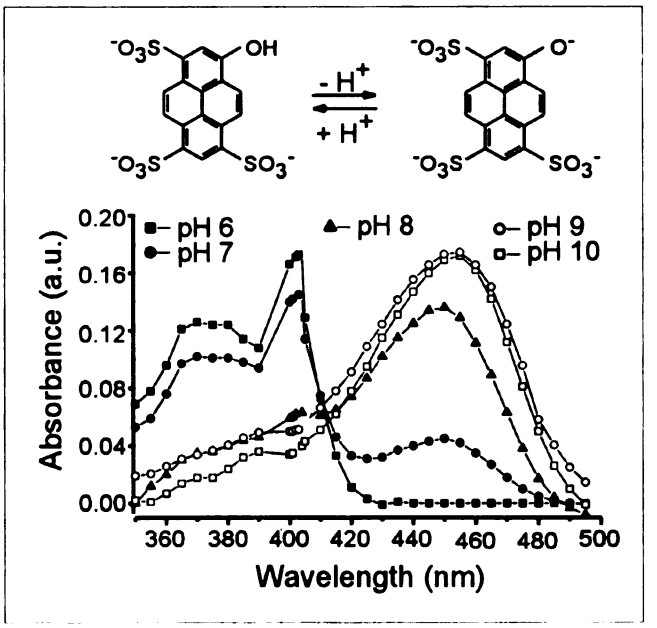

Figure 4.10. Molecular structure and absorption spectra of HPTS in acidic and alkaline pH. Notice that the loss of the hydroxylic proton leads to a large change in the absorption spectrum.

4.4.2 Experimental Section

The sample for the experiment is shown schematically in Figure 4.11. It consists of three capillary tubes (i.d., 1 mm) filled with an acidic solution of HPTS placed in an alkaline solution of HPTS. Frozen raw chicken breast was sliced to a thickness of ~1.5–2.0 mm. The tissue was thawed and placed between the front face of the cell and a glass plate and slightly compressed to a uniform thickness of ~0.5 mm. It was observed that the degree of compression did not affect the nonlinear optical signal. A drop of index matching fluid was used between the tissue and the glass. A transparent mask with the printed letters "MSU" was placed in front of the capillaries and behind the tissue as a reference.

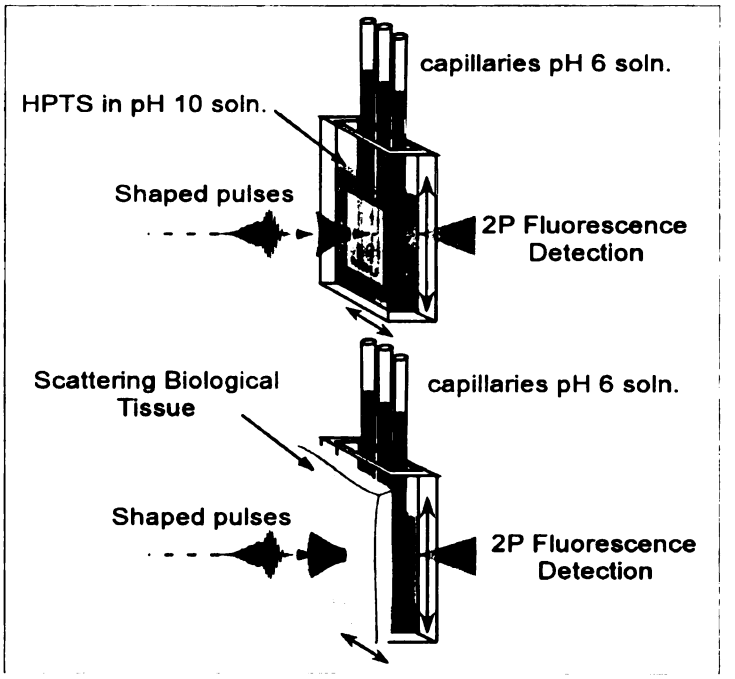

Figure 4.11. Experimental setup used for selective two-photon excitation through scattering tissue. The sample consists of three 1-mm capillaries containing an acidic solution of HPTS submerged in a quartz cell filled with an alkaline solution of HPTS. The sample is raster scanned (without and with scattering tissue) in the focal plane of the beam during data acquisition to obtain the images.

The experiment was carried out with a Ti:S oscillator (K&M Labs) laser system. The laser spectrum was centered at ~830 nm, with a bandwidth of 95 nm (FWHM), corresponding to a 10-fs pulse duration. The large bandwidth is desirable to overlap the absorption of the two HPTS species (see Figure 4.10) by two-photon excitation with the single pulse. The laser was sent to a prism-pair compressor and a broad-bandwidth pulse shaper.[90] The laser pulses were calibrated and compensated to TL pulses at the position of the sample after a microscope objective by using the MIIPS method.[97] This step is critical because it removes unwanted phase deformation introduced by the objective and other optics in the path of the laser beam. Starting from TL pulses, the condition in which all frequency components are in step with each other with a zero phase difference (a blank canvas), ensures reproducible results. The optimized spectral phase functions used for this experiment are based on BPS.[77] By restricting all of the possible values to just two, the search parameter space for the optimum pulses is reduced by ~100 orders of magnitude[77], ensuring a more thorough search by the GA.

Images were obtained by raster scanning the sample at the focal plane of the laser with and without scattering tissue. The laser was focused on the capillaries by a 20x objective (0.45 NA, Plan Fluor extended long working distance, Nikon) (see Figure 4.11). The energy per pulse entering the objective was 1 nJ. The resulting fluorescence from the sample was filtered with a broadband filter (BG40) and a spectrometer with detection wavelength set at 515 nm (24 nm resolution) and averaged point by point using a lock-in amplifier to obtain a two-dimensional (6 x 8 mm) image. Sub-micrometer resolution could be achieved by this method; however, the goal here is mainly to demonstrate that selective excitation is maintained through scattering tissue.

4.4.3 Results and Discussion

4.4.3.1 Functional Imaging

Imaging of the capillary tubes requires laser pulses that selectively excite HPTS in acidic or alkaline solution. Nonselective excitation, as would be obtained from TL pulses, cannot distinguish between the two solutions because HPTS in both environments has an approximately equal integrated cross-section of excitation and fluoresces at 515 nm. The spectral phase for TL pulses (a flat line) and the BP functions that were used to enhance excitation of HPTS in an acidic or an alkaline environment were shown earlier in Figure 4.2. The SHG spectrum obtained from a thin nonlinear optical crystal (Figure 4.2, right) provided a diagnostic test of the effects of phase modulation. SHG has the same square dependence on the intensity of the laser pulses as two-photon excitation. Unlike the TL pulses, the shaped pulses preferentially excite one of the two different pH solutions. The complicated BP introduced in each of the shaped pulses involves several frequencies at which the phase of the light is retarded by π, which is equivalent to 1.3 fs. These seemingly small variations lead to the observed changes in the SHG spectrum. However, the spectrum of the laser pulse does not change upon phase modulation. The potential to cause two-photon excitation or generate second harmonic radiation at specific wavelengths is, however, changed.[65, 66]

Photographs of the sample are shown in Figures 4.12A and B without and with biological tissue, respectively. The capillaries containing HPTS in acidic buffer are barely distinguishable from the alkaline HPTS solution in which they are immersed. Two-photon images obtained with TL pulses without and with biological tissue are displayed in Figures 4.12C and D, respectively. The walls of the capillary tubes (300 μm)

appear black because fluorescent solution is excluded by the wall. This observation confirms the confocal effect gained by two-photon excitation.[92, 130] Note the comparable quality of imaging with and without tissue.

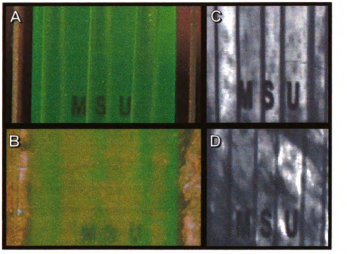

Figure 4.12. *Images A and B are presented in color.* A and B are photographs of the sample obtained under white light illumination in the absence and presence of biological tissue. In both of these photographs, the three capillaries in the sample are difficult to distinguish. C and D are two-photon excitation images obtained by raster scanning the sample without and with scattering tissue, respectively. The walls of the capillary tubes, which look like vertical lines, are approximately 300 μm thick and are clearly visible in both images. Notice that comparable image quality is obtained in the presence and absence of biological tissue. Images C and D were obtained with TL pulses which are not capable of discriminating between the two different pH solutions.

The full effect of coherent control when using BPS is shown in Figure 4.13. The image obtained with phase BP06 enhances the signal from the capillaries (Figure 4.13A), whereas the image obtained with phase BP10 enhances the signal from the surrounding solution (Figure 4.13B). The functional image shown in Figure 4.13C was obtained by dividing the data from Figure 4.13A by the data from Figure 4.13B. The image in Figure 4.13D corresponds to the functional image obtained in the presence of biological tissue. The very high contrast between the three capillaries containing acidic solution and the surrounding alkaline solution is accented by false coloring in the top half of the images

(Figures 4.13C and D). The contrast between the two solutions is very clear even when the laser has transmitted through the tissue.

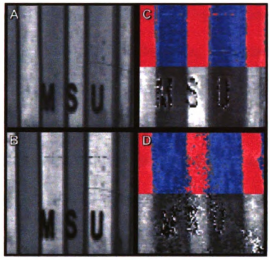

Figure 4.13. Coherent control is used here to obtain pH sensitive functional imaging. Panels A and B show images obtained by two-photon excitation using the optimized phases BP06 and BP10, respectively. Notice that the signal from the 1 mm capillary tubes is enhanced for BP06 (A) and suppressed for BP10 (B). *The top half of images C and D are presented in color.* Panel C shows a functional image highlighting the contrast possible using coherent control. This image was obtained by taking the ratio of the data obtained by BP06/BP10. Panel D shows the functional image obtained when a 1 mm thick slice of biological tissue was placed in front of the sample. Notice that the presence of the tissue reduces the overall signal to noise ratio, but the discrimination between acidic and alkaline HPTS is conserved. The contrast in the functional images can be further enhanced using false color (top half of Figures C and D). Higher values are shaded red, while lower values are shaded blue.

4.4.3.2 Loss of Coherence as a Function of Scattering.

The striking functional images shown in Figure 4.13 raise questions regarding the propagation of shaped and unshaped pulses through scattering media. The experiments described below are aimed at establishing the general physics responsible for the observation and at estimating the limits to future applications.

First, the loss of ballistic photons was measured as a function of scattering. For this experiment, the microscope objective focused the beam onto a 25-μm diameter

pinhole after transmission through a variable scattering medium consisting of a solution of skim milk in water in a 1-cm path-length cell. A 20% increase in the concentration of milk decreased the intensity of the transmitted light by 1 order of magnitude. The light emerging from the pinhole was measured by using a photomultiplier and a lock-in amplifier. The loss of unscattered photons from TL pulses was compared with that from shaped pulses. For this experiment, a phase mask that did not favor two-photon excitation at a particular wavelength was used to demonstrate that there is nothing unique about the rate of coherence loss for shaped or unshaped pulses. The results from these measurements are plotted in Figure 4.14. The scattering of photons from both TL (filled squares) and phase-shaped (filled circles) pulses was found to increase exponentially as the percentage of skim milk in the solution was increased.

Phase shaping does not affect the rate of decoherence, which is caused by the spatial inhomogeneities in the scattering medium. The loss of photons arises from their random collision with particles in the scattering medium, and phase shaping does not alter the scattering probability. Because the scattering of photons is caused by spatial inhomogeneities in the sample, it cannot be corrected or prevented by spectral phase shaping. Replacing the pinhole with an SHG crystal (20 μm β-BaB_2O_4 type I crystal) confirmed that only the ballistic photons participate in generating second harmonic light.[144] The SHG spectra of the TL and shaped pulses are shown in Figure 4.14 Lower Inset. Note that the shaped pulses generate a weak, evenly distributed spectrum. The intensity dependence of the integrated second harmonic light from TL and shaped pulses was found to decay exponentially with a slope that is a factor of 2 greater than that obtained for the fundamental wavelength. This result is consistent with the expected

dependence for two-photon response of $I_{SHG} = I_0 \exp(-2\mu_e x)$. These measurements, which range over more than 5 orders of magnitude in intensity, establish that only the ballistic photons are coherent and are responsible for SHG, that they are lost exponentially, and that spectral phase shaping does not affect this fundamental property. The data in Figure 4.14 show that it is possible to transmit ballistic photons with spectral phase information to depths at which SHG intensity has dropped by 6 orders of magnitude. Additional efforts in noise suppression would allow us to go even deeper, or to collect back-scattered signal.

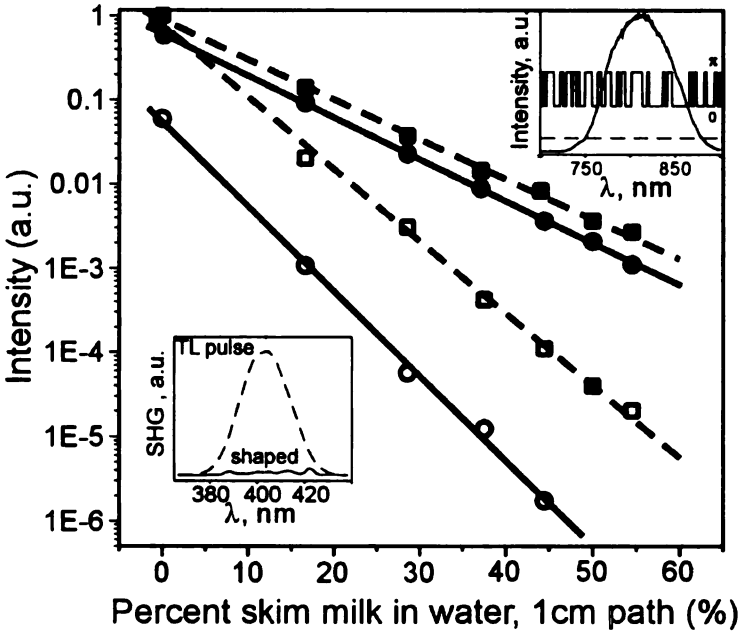

Figure 4.14. Loss of coherent photons as a function of scattering. The transmitted ballistic photons from TL (squares) and shaped (circles) pulses were measured as a function of scattering. The phase shape for these measurements was chosen to suppress SHG generation evenly through the entire spectrum. The intensity of the ballistic photons measured at 800 nm (solid markers) was found to decay exponentially for both TL and shaped pulses. The intensity of the ballistic photons was also measured after SHG from a thin SHG crystal (open markers). A factor of two higher scattering was recorded in this case given the square dependence of SHG, confirming that only ballistic photons generate the second harmonic light. The spectrum and phase for the TL and shaped pulses used in this measurement are shown in the upper inset. The spectra of the SHG output from TL and shaped pulses are shown in the lower inset. Since both TL and shaped pulses have similar slopes, they experience the same rate of scattering.

Figure 4.15 depicts the SHG spectrum generated with TL pulses and the spectrum generated by using BP10 shaped pulses without a scattering medium and with a solution of 15% of skim milk in water in a 1-cm path length cell. Note that the frequency-doubled spectrum of the shaped pulses is unaffected (except in overall intensity) by scattering. There is a slight change that arises from the wavelength dependence of Rayleigh scattering after four scattering lengths, which results in a slight attenuation at shorter (~750 nm) compared with longer (~850 nm) wavelengths. In addition to the retention of phase information, the modulation of phase does not lead to a loss of optical resolution. Figure 4.15 Inset, shows the image of 15 μm diameter microspheres (FluoSpheres:450-480, Molecular Probes). The fluorescent probes were deposited on a microscope slide, covered with a 1-mm-thick slice of biological tissue and topped off with a second microscope slide.

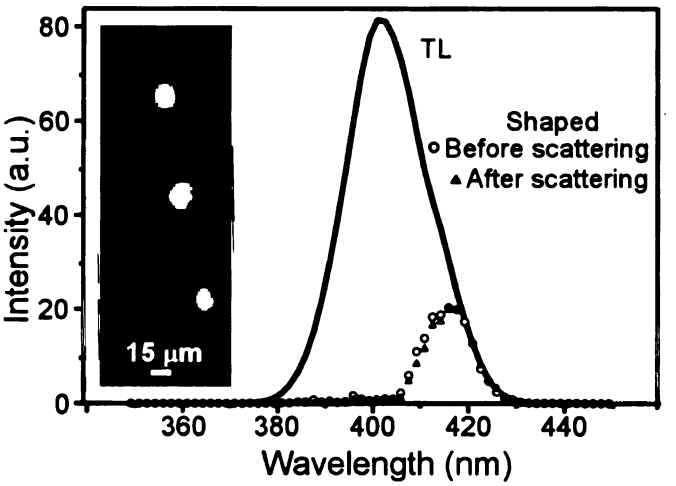

Figure 4.15. SHG spectra generated for TL pulses and shaped pulses optimized for pH10 without a scattering medium and after propagating through a 15% skim milk in water solution (equivalent to 2.1 scattering lengths). All the spectra were normalized to the intensity they had in the absence of scattering. Scattering does not change the observed SHG spectrum. The inset image on the left corresponds to three 15 μm diameter FluoSpheres^{TM} behind a 1 mm thick slice of biological tissue. This image demonstrates that high resolution (micron) can be achieved by the shaped pulses after they transmit through biological tissue.

The sample was raster scanned in front of the laser, which impinged first on the tissue and then on the spheres. The image, obtained by using BP10, showed no loss of resolution when compared with that obtained by using TL pulses. The coherent control method presented for functional imaging is less expensive and simpler to carry out than current methods of multiphoton imaging. The pulse shaper compensates the pulses automatically by using MIIPS and introduces the optimum phases required for selective excitation. This method should be contrasted to an effort in which two expensive 100-fs pulsed lasers tuned to 800 and 900 nm and aligned to focus at the exact same spot would be used to reproduce the observed results. Alternatively, the use of an expensive tunable 100-fs laser would require tuning, alignment, and compression after the objective – procedures that are typically time-consuming and require a certain degree of expertise. Therefore, the ultrashort laser oscillator with a pulse shaper provides a more powerful and flexible platform.

4.4.5 Conclusion

The successful use of coherent control to demonstrate functional imaging through a scattering medium (Figure 4.13) leads us to expect that selective two-photon excitation and imaging could be achieved at greater depths of tissue (3–4 mm).[144, 145] By using amplified laser pulses, measuring two-photon fluorescence through greater scattering lengths (~4 mm) of tissue is possible. For medical applications, endoscopes can be used to deliver the laser pulses to some of the internal organs, allowing therapeutic treatment of internal organs. The maximum amount of laser light that can be used on living tissue is regulated by safety concerns (American National Standards Institute Z163.1) and

ultimately limits the maximum depth that could be achieved by the method described here. Three-photon-induced laser damage, which could result from the use of intense ultrashort pulses,[146, 147] can be suppressed by orders of magnitude by using BPS, while preserving the large two-photon excitation yield obtained by these pulses. This suppression results from lengthening of the pulse due to the phase structure and from the destructive interference for three-photon excitation pathways.[66] The purpose of our experiment was to determine whether coherent control methods based on spectral phase modulation and MII could be used under typical scattering conditions encountered in biological imaging to provide discrimination for laser-based imaging or therapeutic purposes. Given that an affirmative answer to this question is found, possibilities afforded by coherent control could be exploited. In the experiment presented here, functional imaging (as shown here with pH, but also possible with Ca^{2+}, Na^{2+}, biomarkers, and drug gradients) was demonstrated by optimizing the spectral phase of the laser pulses by using a pulse shaper, without laser tuning or fluorescence filters. These advances could enhance noninvasive two-photon imaging methods[104, 148] by providing contrast mechanisms based on selective-probe excitation while minimizing the risk of damaging healthy tissue. Our findings should inspire new possibilities for the use of shaped pulse lasers in the biomedical field.

4.5 Minimizing Multiphoton Excitation Damage with Shaped Pulses

4.5.1 Introduction

Reduced photodamage is widely acknowledged as one of the main advantages of two-photon excitation microscopy on biological specimens.[92] However, for femtosecond pulses, it has also been noted repeatedly that cells are prone to massive damage[149] particularly when excitation intensity at the specimen plane is increased above 10 mW.[146] When laser power is increased above this threshold, nonlinear photodamage sets in. Nondestructive multiphoton imaging of living specimens is restricted to a certain optical window contingent on the molecular multiphoton cross section and fluorescence quantum yield of the fluorophore, the detector sensitivity, and the onset of cell damage. Although photothermal damage appears unlikely in most cells in which water is the major near IR absorber, destructive nonlinear photochemical effects and severe cell damage by optical breakdown effects are nonetheless imminent. Since nonlinear excitation scales linearly (for two-photon) or quadratically (for three-photon) with the inverse of the pulse duration, the availability of picosecond and femtosecond lasers has accelerated the development of multiphoton microscopy. Femtosecond lasers, especially, have been promising excitation sources for nonlinear optical imaging because of their high peak power and greater penetration ability when compared to lasers required for linear excitation. However, the expectation that a factor of ten reduction in pulse duration would lead to one order of magnitude greater signal for two-photon excitation was not realized, and shorter pulses were actually observed to cause greater laser induced damage.[115] Two-photon excitation of endogenous cellular absorbers can result in the formation of destructive oxygen radicals and singlet oxygen and can lead to indirect

DNA damage.[150] Three-photon absorption can result in DNA and protein excitation. A major absorption band of nucleic acids is at 260 nm, which corresponds to three-photon excitation from a Ti:S femtosecond laser, the most common excitation source in multiphoton imaging. Excitation of this band results in direct DNA damage. Although three-photon-absorption should not occur frequently considering the laser parameters used in our experiments, the realization of its high damaging potential in biological imaging, should instigate further developments in multiphoton microscopy in as far as femtosecond irradiation is concerned.

Since selective excitation by phase modulation is a potentially viable tool for multiphoton biomedical imaging, its usefulness can be further expanded to the possibility of suppressing damage brought about by three-photon excitation. Preserving the integrity of biological specimens and ensuring that no damage is being caused by femtosecond illumination is one of the aspects that need to be addressed in phase modulation.

4.5.2 Experimental Section

The efficacy of phase modulation for maximizing two-photon excitation while minimizing three-photon transitions was demonstrated by imaging a 30x30 μm section of a slide containing the chromophores HPTS and L-tryptophan (L-trp) mixed with an aqueous polyvinyl alcohol (4%) solution on glass cover slips. The laser (12 fs pulses centered near 800 nm, 97 MHz, 250 mW average power) was brought in the rear of a Nikon TE2000-U inverted microscope, and focused on the sample with a 60x/1.45 NA objective. The emission was imaged onto a CCD camera (Andor, iXon DV887). To generate the final image, the sample was raster scanned in 0.3 μm steps with a digital

piezo controller (PI, E-710.3CD). Sinusoidal phase functions were used for the selective imaging in this experiment.

4.5.3 Results and Discussion

The role of three-photon absorption in photodamage seems to be particularly relevant when the corresponding one-photon wavelength range for three-photon absorption with our laser system is considered. Three-photon absorption can result in the excitation of DNA and amino acids in proteins and this can lead to cell death. With phase modulation, however, three-photon induced laser damage[146, 147] can be suppressed by several orders of magnitude. This suppression results from lengthening of the pulse due to the phase structure and the destructive interference of three-photon excitation pathways.[66] In addition, the large two-photon excitation yield obtained by these pulses is preserved.

Figure 4.16 shows how phase modulation can be used to achieve selective suppression of three photon excitation while maintaining the efficiency for two-photon excitation. In this case three-photon excitation from L-trp, an amino acid with absorbance maximum at 280 nm and fluorescence at 350 nm is suppressed by almost 90%. The two-photon dye (HPTS), on the other hand, maintains its intensity at the same phase where three-photon excitation is decreased. The effect of phase modulation on these two fluorescent molecules is clear when comparing them with the intensities obtained with TL pulses. Although phase modulation slightly decreases two-photon fluorescence intensity, its effect on three-photon excitation is significant.

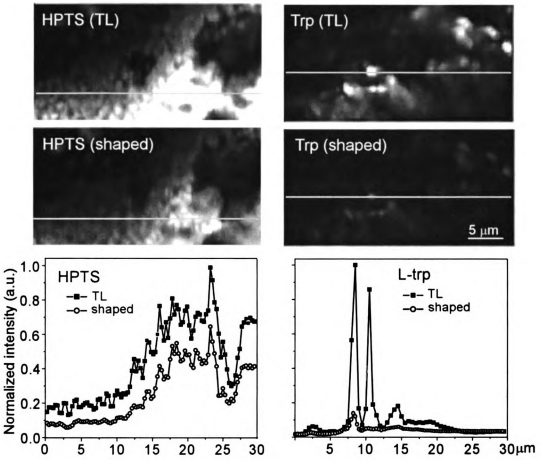

Figure 4.16. Suppression of three-photon excitation by phase modulation. Top: fluorescence image of HPTS and L-trp deposited on a quartz cover slip and imaged with TL 800 nm pulses. Middle: fluorescence from the same samples when laser pulses are shaped with a sinusoidal phase function crossing zero at 0.25 π. Bottom: Cross-section of the fluorescence intensities of both dyes highlights the effect of phase modulation in minimizing three-photon excitation (right) while essentially maintaining intensity of two-photon fluorescence (left). These intensities (normalized) are compared with those obtained using TL pulses. Each image size is 30 μm (width) x 15 μm (height).

The results presented here were generated using pulses that were modulated by sinusoidal phase functions. The greater contrast that is achievable using binary phase modulation urges us to explore the possibility of yet enhancing the contrast achievable with two- and three-photon excitation. The search for these optimal phase functions requires phases that would theoretically lengthen the excitation pulse and consequently

focus two-photon excitation on desired frequency regions while defocusing three-photon excitation away from regions that can cause biological damage.[138]

4.5.4 Conclusion

Multiphoton fluorescence microscopy is becoming one of the methods of choice for dynamic imaging of living cells and tissues. The technique is particularly useful in biological systems where UV excitation would not otherwise be possible due to the light transmission characteristics of optical systems. In addition, side effects such as photobleaching and photodamage are minimized in multiphoton excitation, and occur only in the immediate region surrounding the focal volume. Although these capabilities have been advancing at a rapid pace, a significant amount of work, especially in the area of completely eradicating damage caused by higher order fluorescence excitation, needs to be completed.

With phase modulation of femtosecond laser excitation, the selective suppression of three-photon processes can be achieved while maintaining the efficiency of two-photon excitation. It is worth noting that it is possible to deliver the accurately shaped pluses that are required for selective two-photon activation through thick scattering biological tissue. Selective two-photon excitation and suppression of multiphoton induced damage are two capabilities that will enhance the potential applications of two-photon imaging for cancer detection and two-photon PDT.

CHAPTER 5

ISOMERIC IDENTIFICATION

Multiphoton ionization with a femtosecond laser exhibits a number of specific features that make it a unique ionization technique for analytical and scientific mass spectrometry (MS). Among these is the possibility of highly efficient selective ionization of certain compounds out of complex mixtures while ionization of unwanted substances is suppressed, a feature that can be used to distinguish between isomers. Other interesting aspects include the ability to control the degree of fragmentation even for large molecules[151, 152]. In this chapter, the femtosecond laser is used as the ionization source for MS experiments involving isomeric compounds.

MS, in all its many variants, is an enormously important analytical tool which makes possible the identification of the chemical compounds present in a sample, and in many cases enables assurance of the absence of certain compounds in that sample. It has developed rapidly from being a research tool used primarily in physical organic chemistry to the point where biochemical and medical research applications not only account for a high proportion of its usage but also direct much of the effort concerned with technique development. Recent major developments have increased and continue to expand its scope of application in medical research and other areas. These include the effective use of high mass spectrometric sensitivity and the development of techniques for the analysis of compounds of high mass and low volatility which were previously impossible to analyze.

In most standard implementations of MS, fragmented mass spectra are typically obtained from the energetic ionization process involving collision between neutral gas molecules and free electrons that are typically accelerated to energies between 50 to 150 eV. For most organic compounds, electron ionization (EI) has its highest cross section in the region of 70 eV, where enough excess energy is transferred to the molecule to generate fragmentation of the ion. Such fragmentation can be very useful in providing structural information. For this reason, there exist extensive libraries of mass spectral data at the standard ionization condition of 70-eV EI.[153] There are, however, disadvantages to this approach. First, the analysis can become very difficult in the case of complex mixtures. Moreover, it is often the case that different species of the same basic molecular type yield practically identical fragmentation patterns. Many isomeric compounds yield virtually indistinguishable mass spectra. In such a case, positive identification of an isomeric molecule requires a technique by which one can measure the parent molecular mass and distinguish the molecule from its isomers through its fragmentation pattern. This is even more important when one wants to analyze a mixture of such compounds.

The premise of this study is that certain phase-shaped laser pulses could control the ionization and fragmentation of isomeric molecules so that positive identification of isomers could be accomplished. Shaped femtosecond laser pulses are explored as an unconventional ionization technique to improve isomer specificity in MS. Qualitative discrimination of structural and geometric isomeric compounds, including the potential for quantitative analysis of mixtures of isomers are investigated in this chapter.

5.1 Isomerism

The mass spectra of certain isomeric compounds have barely enough information that helps to ascertain the identity of such molecules. While close examination of certain minor peaks in the spectrum could possibly help identify one isomer from the other, small changes in instrumental parameters could mask these effects, and the value of this practice with real samples is doubtful.

Isomers are molecules with the same molecular formula, but different arrangements of atoms. There are different types of isomers, as shown in Figure 5.1.

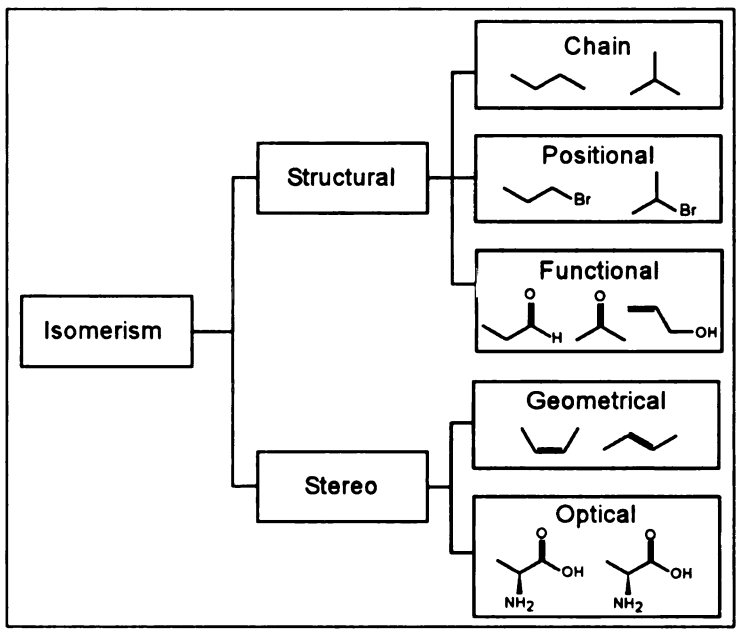

Figure 5.1. Classification scheme of isomers (with examples).

5.1.1 Structural Isomerism

Structural isomerism occurs when two or more compounds have the same molecular formula, but different structures, which tend to give the molecules different chemical and physical properties. Structural isomerism can either be chain, positional or functional.

The possibility of branching in carbon chains leads to chain isomerism. The molecule butane, C_4H_{10}, for instance, has two isomers - one where all carbon atoms lie in a straight chain and the other where the chain is branched. In position isomerism, the basic carbon skeleton remains unchanged, but important groups are moved around on that skeleton. For example, the structural isomers of C_3H_7Br include one where the bromine atom is on the end of the chain, and one where Br is attached to the middle carbon. Position isomers also occur on benzene rings, as in ortho-, para-, or meta-nitrotoluene. In functional group isomerism, the isomers contain different functional groups - that is, they belong to different families of compounds. For example, the molecular formula C_3H_6O could be either propanal (an aldehyde) or propanone (a ketone). There are other possibilities as well for this same molecular formula, including a carbon-carbon double bond (an alkene) and an -OH group (an alcohol) in the same molecule (see Figure 5.1).

5.1.2 Stereoisomerism

Stereoisomerism occurs when the atoms in a molecule can have different arrangements in space. The bond structure of stereoisomers is the same, but the geometrical positioning of atoms and functional groups in space differs. This class includes optical isomerism where different isomers are mirror images of each other, and geometric isomerism where functional groups at the end of a chain can be twisted in different ways. Geometric isomerism or cis-trans isomerism describes the orientation of functional groups at the ends of a bond around which no rotation is possible. Such bonds are typically double bonds, but they can also be part of a ring structure which prevents rotation. Cis isomers and trans isomers of a substance have different physical properties.

Trans isomers generally have higher boiling points and higher densities. This is because the molecules of trans isomers can line up and fit together better than the cis form. Optical isomers of a given compound are often identical in all physical properties except the direction in which they rotate light. The molecules of optical isomers are asymmetrical and are mirror images of each other, as signified by L-alanine and D-alanine (see Figure 5.1). Molecules like these are said to be chiral and the different forms are called enantiomers. The concept of optical isomerism, which in itself constitutes a field of chemistry (chiral chemistry), will be discussed further in the next chapter.

5.2 Isomeric Identification by Laser Control and MS[g]

5.2.1 Introduction

While it is true that several analytical techniques, including MS, are widely used for molecular identification, the possibility of utilizing quantum-mechanical laser-matter interactions to selectively discriminate molecules, in particular, isomers, could enhance the utility of MS. This chapter introduces a coherent laser control technique that is coupled with MS to distinguish between pairs of isomers, which by standard MS alone, are difficult to discern.

Knowledge of the exact isomeric configuration of a molecule can be important since different isomers can have widely varying toxicological properties and environmental impacts. Analysis of extremely toxic environmental pollutants requires high sensitivity, typically in the parts-per-billion range. MS, being the most sensitive of analytical methods, has been used for all kinds of chemical analyses, from detection of

[g] Reproduced in part with permission from J.M. Dela Cruz, V.V. Lozovoy, M. Dantus, "Isomer identification by mass spectrometry with shaped femtosecond laser excitation," *J. Phys. Chem. A* **109**, 2005, 8447-8450. Copyright 2005 American Chemical Society.

pollutants like dioxin[154] to finding high-grade petroleum in sludge.[155] It is also used to detect steroids in the urine of athletes[156] and contaminants in herbal supplements. However, conventional MS alone cannot be used for isomer-specific analysis of certain toxic chemicals. This method of ionization falters in showing reproducible differences between isomers. The ability of spectroscopic analytical methods such as IR, Raman and nuclear magnetic resonance spectroscopy to distinguish between pairs or sets of isomers is indisputable. Nevertheless, the orders of magnitude lower detection limit of MS, with the possibility for achieving single ion sensitivity, should give MS an added advantage over these methods. Another significant asset of MS is its capability of handling complex mixtures in tandem with GC.[157, 158]

Although GC/MS is widely used for a variety of environmental, biological, and other applications, the interpretation of the resulting data can be complex and time consuming.[159] While many laboratories have such instrumentation, its use for isomeric identification is not trivial. Significant time and effort must be put into configuring the instrument for analysis; standards must be prepared for each target compound; and the GC temperature program must be optimized to provide efficient separation of compounds. The response function must be determined from the analysis of the standards. The entire process is prone to numerous pitfalls such as contamination, carryover, and misinterpretation of the data.

Isomeric differentiation has been achieved via selective self-ion/molecule reactions and tandem MS in ion trap mass spectrometers, but the whole process takes several minutes.[160, 161] Isomeric compounds of pentane have, for instance, been distinguished by monitoring the products of their reactions with mass-selected ions

generated from the individual isomers in an ion-trap.[162] Resonance enhanced multiphoton ionization employing molecular cooling in a supersonic beam has also been used to separate isomers, although, a tunable UV laser source and a special coupling of a GC column and a supersonic beam valve are necessary.[163] Chemical reactivity has been coupled with MS for identification,[164, 165] though the universality of this approach is uncertain.

Femtosecond lasers have long been used as a source of ions in MS; in most cases these studies were aimed at measuring ultrafast photo-dissociation dynamics.[166, 167] The energy deposited by the laser pulse on the molecules sets off a number of competing processes, primarily ionization, fragmentation, and redistribution of the energy among the different degrees of freedom in the molecule. It has recently been shown that the relative yield of the resulting fragment ions can be controlled to some extent by shaping the femtosecond laser pulses.[32] Specific phase functions that determine the relative phase of different frequency components in the pulse can be introduced using a pulse shaper.[90] At present, there is no theoretical model that provides a link between pulse shaping and its effects on molecular ionization and fragmentation. While such a model is still to be developed, empirical searches guided by computer learning algorithms, as suggested by Judson and Rabitz,[11] had been used to explore the extent of selectivity.[37, 167, 168]

The Dantus group has developed a method based on a 15-minute (typically) exhaustive evaluation of an entire subset of phase functions which introduces a varying degree of MII[65, 66] occurring among excitation pathways during laser-induced ionization and fragmentation. To facilitate the search and increase its efficiency, BP functions are used. Only a small number of frequency regions (pixels) are modified in this case. In fact,

as few as 8-bit BP functions have been shown to effect changes (two orders of magnitude) on the relative yield of particular fragment ions. With pulse shaping, the sensitivity of laser-molecule interactions to differences in electronic and molecular structures of compounds can be amplified.[169] This method of laser control, which is coupled with the detection sensitivity of MS, can be used to identify isomers and quantify their relative concentration in isomeric mixtures. The structural isomers (ortho and para) of xylene, one of the high production volume chemicals produced in the United States, were evaluated with this method. A quantitative assessment of the relative concentrations of these isomers in mixtures also demonstrates the analytical ability of this method.

5.2.2 Experimental Section

Prior research from the Dantus group which involved femtosecond pulse shaping and MS, established the multidimensional capability of femtosecond laser control in identifying a number of chemical compounds based on the unique spectral fingerprints generated from different BP-shaped pulses.[169] In this chapter, sub-second and reproducible isomer identification is achieved with the experimental setup shown in Figure 5.2.

An amplified 800 μJ/pulse femtosecond laser (35 fs) is sent to a pulse shaper programmed to measure and characterize the laser pulses and to correct unwanted phase distortions on the laser pulses using the MIIPS method.[97, 170] The correction of phase distortions to generate TL pulses is critical for experimental precision and reproducibility because the nonlinear interaction between the laser pulses and the molecules is very

sensitive to phase variations in the laser pulse. It is this nonlinear interaction that leads to ionization and fragmentation.

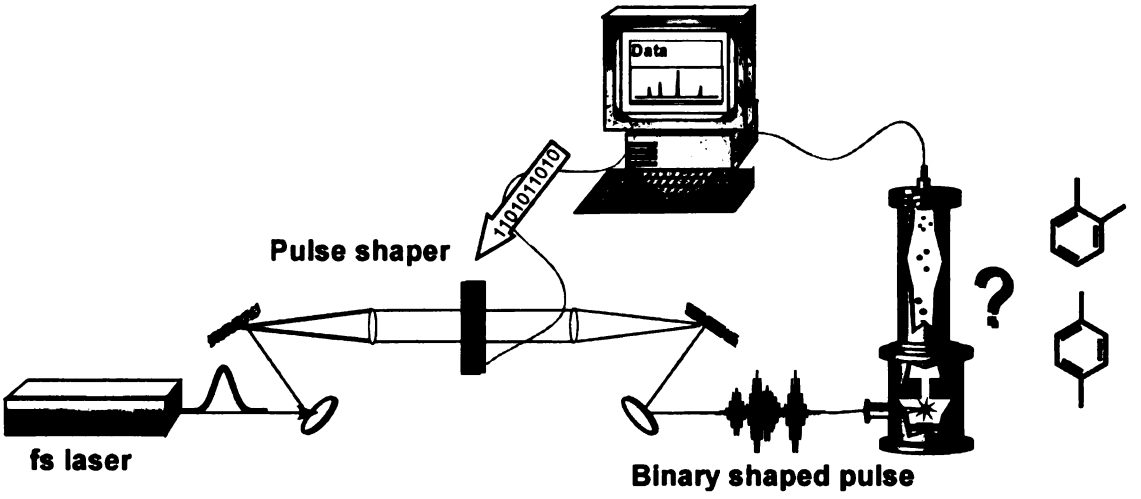

Figure 5.2. Schematic experimental setup for laser control MS for the identification of isomers. The amplified femtosecond laser is sent to a pulse shaper that is programmed to measure and compensate any phase distortions present on the laser pulse. BP functions are introduced at the Fourier plane, where the spectrum of the pulse is fully dispersed. The phase-shaped laser pulses are focused inside a low pressure gas chamber where they interact with the sample molecules, causing fragmentation and ionization. A TOF mass spectrometer is used to record the arrival of the ions according to their mass-to-charge ratio. Some BP functions cause large enough differences in the fragmentation and ionization patterns that can be used to identify isomers and even quantify their concentration in a mixture.

BP functions are introduced at the Fourier plane of the pulse shaper, where the spectrum of the pulse is fully dispersed. Each phase function contains ten groups of ten pixels. A phase retardation equal to 0 or π is assigned to the ten corresponding regions in the spectrum of the pulse. Because only the phase of the pulse is modulated, the energy and the spectrum of the excitation laser field stay unaltered throughout the experiment. The phase-shaped laser pulses are then focused inside a low pressure gas chamber where they interact with gaseous sample molecules causing ionization and fragmentation.

The experimental data were obtained using a vacuum system (see Appendix B) equipped with a time-of-flight (TOF) mass spectrometer. Several samples, which included the ortho and para isomers of cresol and the cis/trans isomers of the alkenes 3-heptene and 4-methyl-2-pentene (MP) (Sigma Aldrich) were tested. Preliminary test runs were performed on these isomers before the main samples, ortho- and para-xylene, were tested. These compounds were used without further purification. The molecules were leaked into a high-vacuum chamber by a precision valve (Pressure ~ $8x10^{-6}$ Torr) and interacted with the femtosecond laser beam in the focal volume. The chamber was pumped by a 220 L/s turbomolecular vacuum pump where fast flow prevents the accumulation of fragments. The voltages on the extractor and repeller plates were kept at 1600 and 2500 V, respectively. The ions were allowed to travel in a drift-free zone of about 24 inches before being detected by a microchannel plate. Each mass spectrum obtained represents the signal average resulting from 128 laser shots. The laser was attenuated to 130 μJ/pulse at the TOF chamber entrance.

A total of 1024 different phases representing all possible 10-bit BP functions were evaluated. The phases are referred to in the text as BP*X*, where *X* corresponds to the decimal value of the binary number; i.e., the phase function 0000000000 corresponds to BP0 and 1101011010 corresponds to BP858, where 1 is replaced by π retardation at the corresponding position in the spectrum. Some BP functions cause large enough differences in the fragmentation and ionization patterns that can be used to identify isomers and even quantify their concentration in a mixture. The mass spectral responses of the xylene isomeric pair to a number of phase functions were observed. The BP

functions which provided either minimum or maximum ion ratio differences between the isomers were further analyzed.

5.2.3 Results

For the pairs of isomers tested, the standard 70-eV EI mass spectra[171] show significant differences in terms of relative abundances of the molecular ion and its fragments. Based on existing mass spectral libraries (NIST), these isomeric compounds did show considerable (~10.5% to 30%) differences in certain ion yields. Among the samples studied, xylene gave the smallest difference (<3% for all peaks), making it virtually impossible to differentiate between its ortho and para isomers using standard MS. Figure 5.3 shows the differences in relative abundances of each fragment ion between the pairs of isomers studied. The plots shown were derived from standard NIST data[171] and were obtained by subtracting the 70-eV EI mass spectrum of one compound from that of its isomer. Before these difference spectra were obtained, all peaks in the original mass spectra were normalized to the highest mass ion peak for each isomeric sample. The statistical reliability of the mass spectral data used, specifically in terms of the peak intensities, were not provided. However, mass accuracies of 5 ppm or less for small organic molecules and 0.01% for large samples are typical for most MS measurements.

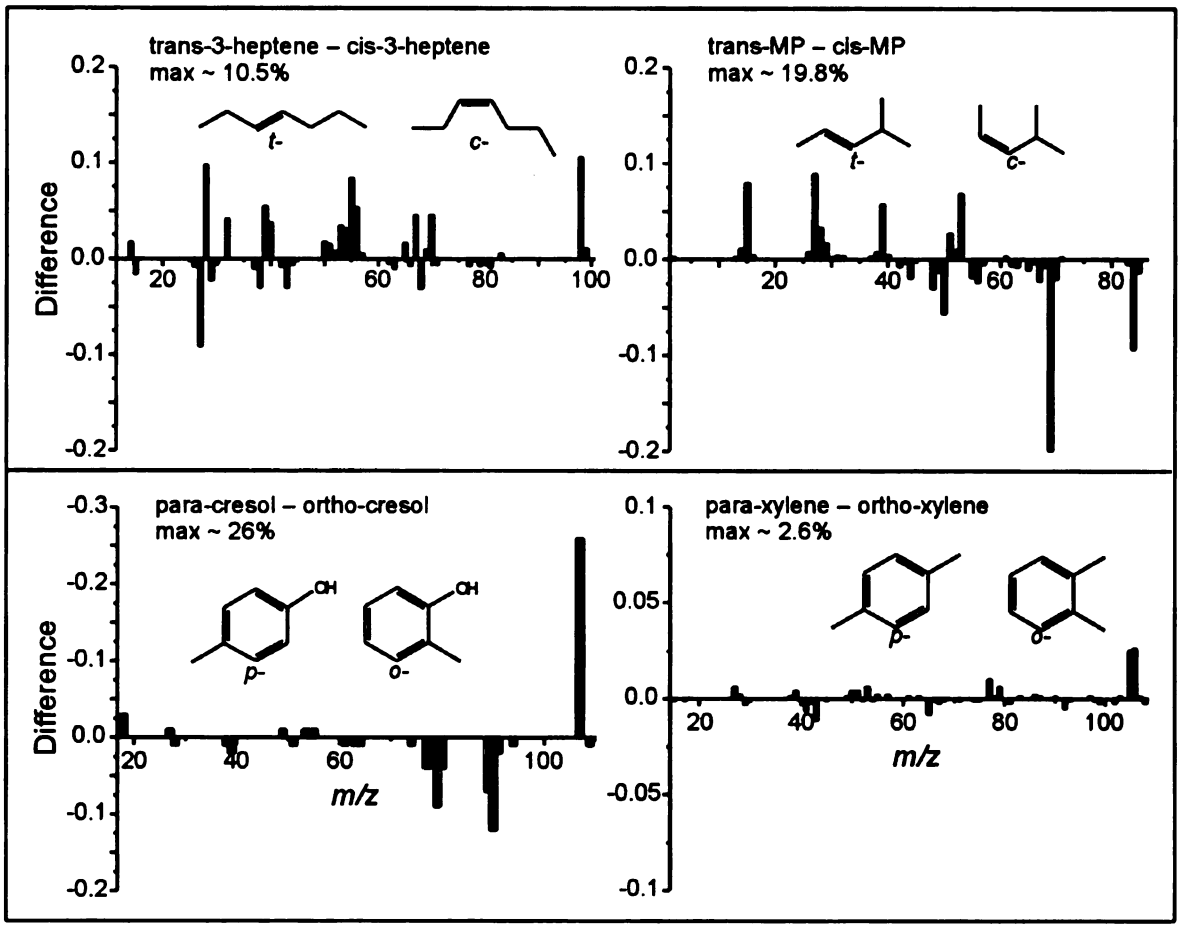

Figure 5.3. Difference mass spectra of the various sample isomeric pairs tested: 3-heptene, 4-methyl-2pentene (MP), cresol, and xylene. The maximum differences obtained from the standard mass spectra (NIST) of isomeric compounds, particularly ortho and para-xylene, make differentiation by conventional MS difficult. Note the difference observed in xylene (2.6%) compared to the rest of the compounds tested. The structures of the compounds are also shown.

Since the error associated with the intensity of a single fragment ion peak can sometimes be unpredictable, analysis of data obtained with the femtosecond laser was focused on deciphering mass spectral differences of isomeric pairs of molecules based on ratios of intensities between two fragment ion peaks. Such peaks were chosen on the basis of maximum ion ratio differences obtained between the isomers.

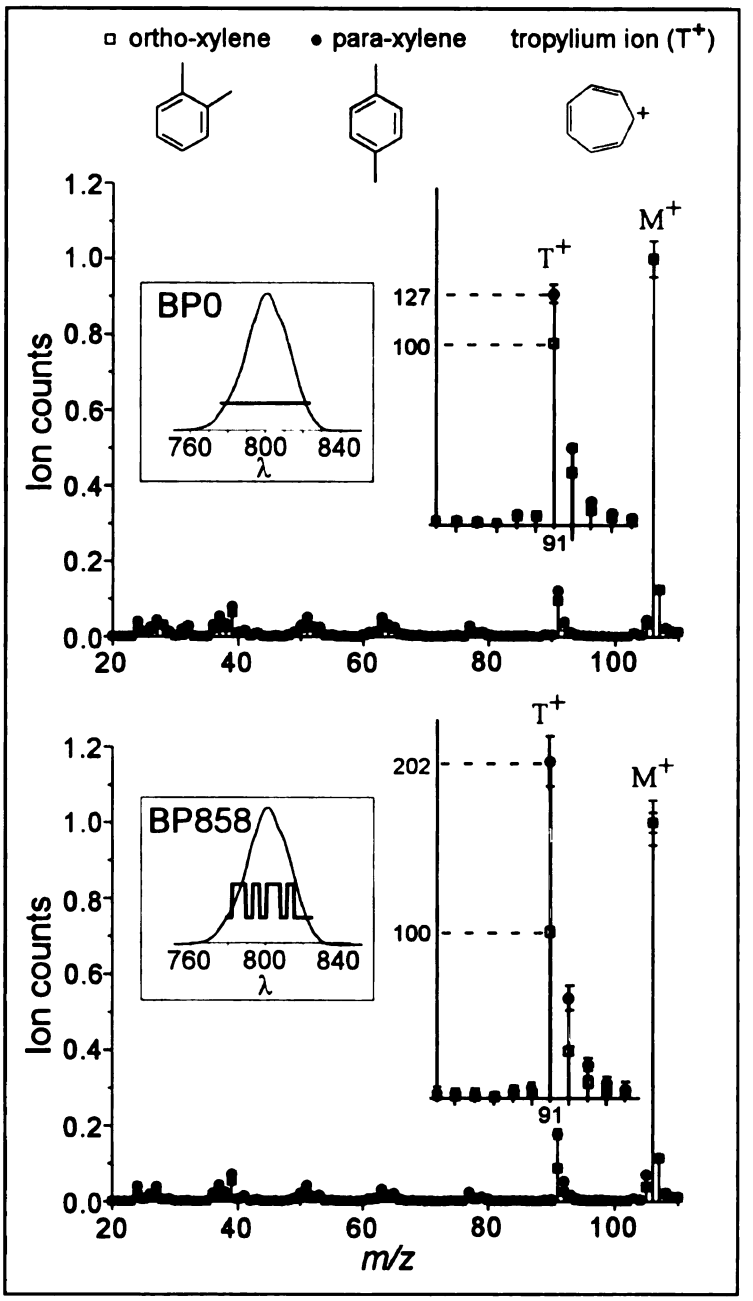

Figure 5.4. Laser control mass spectra obtained for ortho- and para-xylene. The top panel shows results obtained with BP0 corresponding to TL laser pulses; the flat phase across the spectrum of the laser pulse is shown in the inset. The bottom panel shows data obtained with laser pulses with phase BP858, which is shown together with the spectrum of the pulse in the bottom inset. The mass spectra were normalized so that the molecular ion (M^+) intensity equals unity. In the top and bottom panels, the region for *m/z* near 91, corresponding to the tropylium ion (T^+), was amplified to highlight the observed differences. For the BP858 shaped pulses, the relative yield of T^+ for p-xylene is 2 times greater than that observed for o-xylene.

The mass spectra obtained by femtosecond laser phase control for the xylene isomers were analyzed based on the ratio between the peak value obtained for the molecular ion (M^+, m/z=106) and the tropylium ion[172] (T^+, m/z=91). All peaks were normalized to the molecular ion peak. Figure 5.4 shows that the application of a complex BP-shaped pulse resembling BP858 results in a greater relative yield of the tropylium ion for para-xylene compared to that of ortho-xylene. The differences observed for the other major fragment ions were not as significant, and were not further analyzed.

Figure 5.5 shows the statistical distribution of the ratios between the molecular ion and the tropylium ion obtained for each isomer, highlighting the contrast achieved using binary shaped pulses. The ratios are represented by histograms of 100 independent measurements for each sample and for each phase. For TL pulses, a difference between the two isomers is clear. However, the difference observed for BP858 is much greater.

The ratio between ionic fragments at m/z 106 and 91 (106/91) for ortho-xylene (11.21 ± 0.40) is about a factor of 2 greater than para-xylene (5.62 ± 0.17). When compared to TL pulses, the shaped pulse enhanced fragmentation leading to a lower M^+/T^+ ratio for para-xylene. Interestingly, the opposite trend was observed for ortho-xylene. TL pulses also gave relatively greater ion ratios for ortho-xylene (10.53 ± 0.17) than for para-xylene (8.18 ± 0.14), but the difference between the isomeric ratios is less.

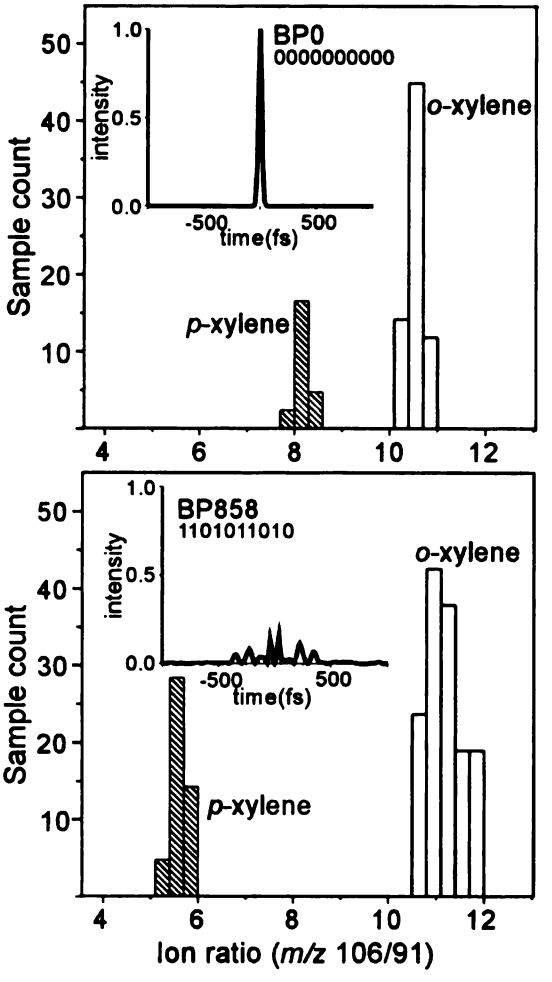

Figure 5.5. Histograms showing the statistical distribution of the experimentally measured ratio (M^+/T^+) obtained for 100 independent measurements each for o- and for p-xylene. The top graphic shows the histograms obtained using laser pulses with phase BP0; the bottom graphic shows the histograms obtained using laser pulses with phase BP858. The insets show the temporal profiles of the two different laser pulses. The histograms obtained for BP858 show a greater (~2x) molecular-ion-to-tropylium-ion ratio. Note that in most cases the distribution of measured values is compact, indicating good reproducibility of the results. The observed differences can be used for fast and reliable identification between these two isomers.

The quantitative performance of our method was assessed by the analysis of six different mixtures of the two xylene isomers. The mixtures were probed by the phase-shaped pulses, and the ratio of the molecular ion to tropylium ion peaks was recorded. The average of two independent sets of measurements plotted as a function of concentration are shown in Figure 5.6. The linear behavior of the data agrees with the

analytical formula $(M^+/T^+)_{normalized} = [(M^+/T^+)_{experimental} - (M^+/T^+)_0] / [(M^+/T^+)_1 - (M^+/T^+)_0]$, where $(M^+/T^+)_{experimental}$ is the measured peak ratio for each sample mixture. $(M^+/T^+)_0$ is the peak ratio measured for a pure para-xylene sample, and $(M^+/T^+)_1$ is the measured peak ratio for pure ortho-xylene. The normalized molecular ion to tropylium ratios directly provide the relative concentration of the ortho isomer in the mixture.

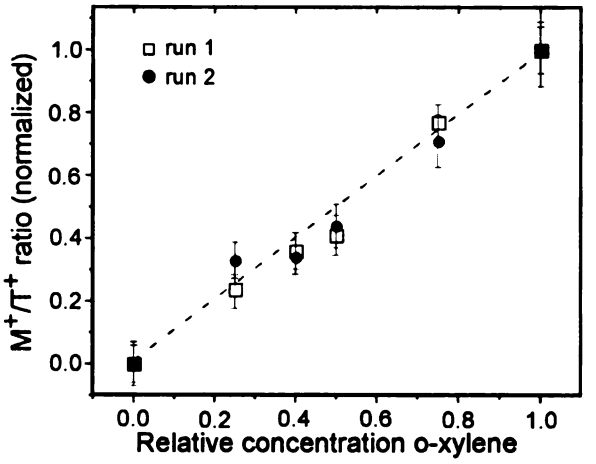

Figure 5.6. Quantitative concentration measurements of isomeric mixtures using laser control MS. Each data point represents an average of 100 measurements (0.1 s total) obtained for each of six different mixtures. The horizontal axis corresponds to the known concentration of each of the mixtures. The vertical axis corresponds to the normalized M^+/T^+ ratio, which increases linearly with the relative concentration of o-xylene. This linear relationship provides a quantitative method to determine the concentration of each of the isomers (o- and p-xylene) in a mixture. Two sets of data obtained in two different days are shown to illustrate the robustness of this method.

The maximum peak ratios obtained for the isomeric pairs of 3-heptene, cresol, xylene, and MP are shown in Figure 5.7. The reported ratios were derived from selected major fragment-ion peaks observed for each isomeric pair, thus ensuring statistically acceptable standard deviations. Although minor peaks provided sizeable ion ratios, their usefulness for quantitative work is diminished by their greater susceptibility to noise.

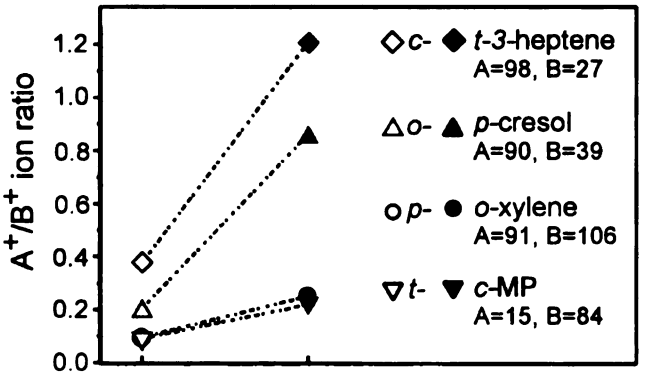

Figure 5.7. Ion peak ratios (A^+/B^+) obtained for several isomeric pairs using binary shaped pulses. The legend indicates the *m/z* values (A and B) of the fragments chosen.

The maximum ratio difference observed for xylene in particular, as seen in the figure above, ranged from 0.09 for the ortho isomer to about 0.20 for para-xylene. This corresponds to a difference of roughly 50%, which, when compared to the NIST difference (~3-4%) (see Figure 5.3), makes an amazingly straightforward distinction between the two isomers. Although the rest of the isomers already showed disparities in their NIST spectra, these differences were enhanced several times more with shaped femtosecond laser irradiation.

5.2.3 Discussion

5.2.3.1 Photoionization and fragmentation of xylene

As a consequence of multiphoton absorption, the fragmentation of molecules can be effected by two distinct mechanisms- the process of dissociation followed by ionization (DI, ladder switching) or ionization followed by dissociation (ID, ladder climbing).[173, 174] Based on the mass spectra obtained and because of the short pulse duration of the laser[174], the xylene molecules fragment by the ID route: the molecules absorb a number of photons to reach a dissociative state below the ionization level. If the

laser pulse length is longer than the lifetime of the state, then the molecular fragments form neutral moieties. Depending on the laser intensity, these fragments may absorb additional photons within the initial laser pulse to ionize or further fragment. For xylene and most organic compounds, ionization energies range from 8 to 9 eV. The absorption of six photons of energy $h\nu$ of 1.55 eV each should be sufficient to induce ionization. As shown by measurements of photoelectron energies,[175] molecules ionize as soon as the sum of absorbed photon energies exceeds the lowest ionization potential. Subsequent absorption by the ion results in extensive fragmentation.[176-179]

Structure evaluation of xylene using laser control mass spectrometry is anticipated, owing to the fact that an appreciable population of the molecular ion survived to give an indication of the molecular weight of the compound. Parent ion dominance (electron is predominantly emitted from the phenyl ring) and limited dissociation in the mass spectra of the xylene isomers are attributed to the slow dissociative state of the compound, highlighting its thermodynamic stability. Even the tropylium ion, which in EI MS is the most abundant ion (even greater than the molecular ion itself), was particularly low in yield. Fragment ions with m/z <91 also produced rather low yields. The ionization process is presumably completed within the duration of the laser pulse, leaving very little time for the molecule to fragment to any significant extent. An observed power dependence of the ion peaks suggests that molecular fragmentation of xylene follows the ID mechanism, as suggested by Kosmidis et. al. in their study of the nitrotoluene isomers.[180]

5.2.3.2 Laser-based isomer recognition

It is interesting to understand the mechanism responsible for the observed laser-based recognition. The nonlinear optical polarizability of molecules is highly dependent on molecular structure.[181] Strong laser fields have been found to cause charge buildup at the ends of extended conjugated systems resulting in ionization by tunneling or barrier suppression.[182] A greater nonlinear optical polarizability increases a molecule's susceptibility to undergo fragmentation. This is consistent with our results for xylene, and with the slightly lower ionization energy of para-xylene (8.44 ± 0.05 eV) compared to that of ortho-xylene (8.56 ± 0.04 eV). This observation was also evident in the other isomeric samples, where the structures of trans-3-heptene and trans-MP make them more polarizable than their isomeric partners. Consequently, the yield of most of their ion peaks is relatively greater than those of their isomeric counterparts.

The close correlation between SHG intensity and peak ion intensity gives the impression that the effects observed are intensity dependent. Figure 5.8A shows a plot of SHG intensity vs. BP function. The phases were sorted according to decreasing SHG intensity, highlighting the exponential decay of intensity with complexity of phase function. Figures 5.8 B and C show a corresponding relationship between ion peak intensities (*m/z* 91 and 106) and the sorted phase functions. Regardless of the suggested similarities, differences between ortho- and para-xylene were still apparent.

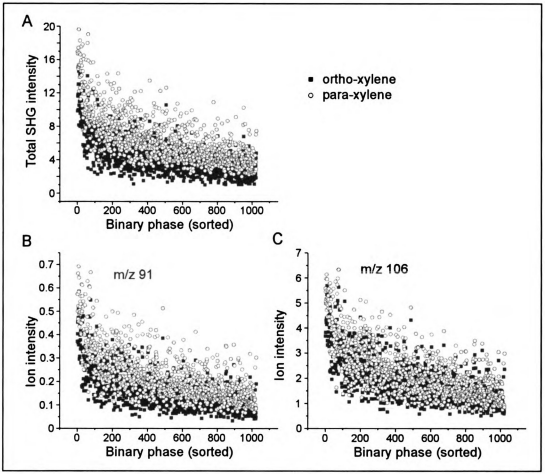

Figure 5.8. Correlation between SHG or ion intensity and complexity of BP function. A. General exponential decay of SHG intensity as phases are sorted based on the average SHG intensities recorded during data acquisition of ortho- (black squares) and para-xylene (open circles). B. Relation between ion intensity of mass peak at *m/z* 91 and sorted BP function. C. Relation between ion intensity of mass peak at *m/z* 106 and sorted BP function.

The temporal profiles for the different laser pulses used here are quite diverse, as represented by TL and BP 858 laser pulses. (see insets of Figure 5.5). The observed outcome of the reaction could be attributed to the time-frequency structure of the pulse Although the total ion yield was about 6 times lower for shaped pulses than for TL pulses, the differences observed between the isomers appear to have increased with pulse shaping.

Figure 5.9 indicates how ortho- and para-xylene can be distinguished based on the phase structure of the laser pulse. The ion ratios (*m/z* 91/106) for the isomers are clearly different when all 1024 phases are considered. The complexity of the structures of the BP functions that provided maximum contrast between isomeric pairs may have a temporal effect on the responses of the molecules. When the sorted phase functions are grouped to provide a statistical indication of peak intensity vs. phase complexity, the ion ratios obtained clearly distinguish one isomer from the other (Figure 5.9, right). Although a direct link between the BP modulation of the pulse and the selective molecular response has yet to be established, the observed differences allowed us to devise a quantitative measurement of the relative concentration in a mixture of these isomers.

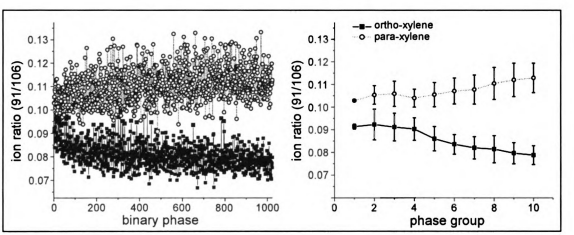

Figure 5.9. Left: Correlation of ion ratio intensity (*m/z* 91/106) and sorted phase function for ortho- and para-xylene. Ortho-xylene is clearly distinguishable form para-xylene. The difference is observable for most of the phase functions used. Right: Grouping the sorted phases according to complexity shows maximum contrast (*m/z* 91/106) between the isomers for more complex phase structures. Phase group 1 consists of 2 phases, group 2 contains 4, group 3 has 8, group 4 has 16, group 5 has 32, group 6 has 64, group 7 has 128, group 8 has 256, group 9 has 256, and group 10 consists of 258 BP functions. The phases were sorted based on their effect on SHG intensity.

One of the major objectives of our work is the extension of MS to problems in biomedical chemistry. A future research effort is directed towards developing laser control methods for elucidating the structure of peptides and proteins. In metabolomics, the coupling of the high sensitivity of femtosecond laser control with the high resolution of MS could provide a method for determining a rough estimate of the number of metabolites present. MS could offer a valuable first indication of the identities of molecules, while laser control contends with its inability to separate molecules of the same molecular mass. Even as emerging MS technologies continue to cope with the expanding demand for applications in a wide range of areas, the complexity associated with these techniques is a drawback. Controlled fragmentation with femtosecond laser pulses is a viable alternative to most existing hyphenated (e.g. GC/MS, LC/MS, IMS/MS) and tandem MS methods, in terms of its ability to rapidly discriminate between structural isomeric compounds.

5.2.5 Conclusion

The principle of molecular control by pulse shaping with BP functions expands the capabilities of conventional MS to include fast, accurate, and reproducible qualitative and quantitative isomeric identification. This approach provides a new dimension in MS that is highly sensitive to molecular structure, as required by current biological and environmental applications. While there are a number of technological platforms available for chemical, including isomeric identification, none are perfect, with each method providing different merits. Although the perceived notion is that coherent control using femtosecond lasers is too complicated and too expensive to be useful to biologists

and environmental scientists, awareness of its potential capabilities for analytical work and its eventual applications in the biomedical field substantiate further investigation of this technology. The accessibility of one-box "no-expert-required" femtosecond lasers and the imminent development of laser systems with integrated pulse shapers should further reinforce the usefulness of laser control in MS. The question remains as to whether shaped femtosecond laser technology could address isomeric identification and quantification issues that cannot be answered by any other existing analytical method. Perhaps the next real challenge is whether this technology could pave the way for the resolution of optical isomers through laser control.

CHAPTER 6

CHIRAL PULSES AND CHIRAL RECOGNITION

The idea that something seemingly so simple such as optical isomerism can have such far-reaching ramifications is amazing. To think that the simple rotation around a carbon bond could determine whether or not something was going to be recognized, the affinity with which it would be bound, and the efficiency of the attached complex is truly astounding. With optical isomerism, there is no difference in connectivity. The isomerism has to do with the arrangement of the atoms in space. It arises from the handedness property (chirality) of molecules through the presence of a chiral center. Optical isomers are non-superimposable mirror images of each other; a set of optical isomers are called enantiomers.

The recognition of chiral compounds is a fundamental phenomenon that is observed in all biological systems, ranging from single cell organisms to the most complex of animals. In nature, only the L form (left-handed) of amino acids are used to make peptides or proteins, and only the D form (right-handed) of sugars exist, but there are no such constraints in the laboratory. The specificity and efficacy of many biologically important reactions are based on chiral interactions. The biological activity of chiral substances often depends upon their stereochemistry, since the living body is a highly chiral environment. A large percentage of commercial and investigational pharmaceutical compounds are enantiomers, and many of them show significant enantioselective differences in their pharmacokinetics and pharmacodynamics. The importance of chirality of drugs has been increasingly recognized, and the consequences

of using them as racemates (equal amounts of left- and right- handed stereoisomers of a chiral molecule) or as pure enantiomers have been frequently discussed in the pharmaceutical literature during recent years. With increasing evidence of problems related to stereoselectivity in drug action, enantioselective analysis requires intensive research. Producers of pharmaceuticals are required to evaluate the effects of individual enantiomers and to verify the enantiomeric purity of chiral drugs that are produced. The pharmaceutical properties and toxicity must be established independently for both enantiomers even if the drug is to be marketed as a single enantiomer. As a result, chiral recognition has been an area of intense interest, especially in the past decade. Significant progress has been made in understanding chiral recognition from both fundamental and application oriented perspectives, yet a complete understanding of chiral recognition has yet to materialize.

Most of the pharmaceutical and pharmacological studies of stereoselectivity of chiral drugs before the mid-eighties involved pre-column derivatization of the enantiomers with chiral reagents, forming diastereomers. The diastereomers were subsequently separated in the normal or reversed phase mode of chromatography.

Great efforts have been devoted to the development of better methodology for enantioselective chromatography during the past decade, and have resulted in new chiral stationary phases, pioneered by Pirkle[183]. Chiral agents were derivatized and immobilized on the surface of the support (silica gel mostly), and served as the in situ chiral discriminators during the chromatographic process. The preference of chiral stationary phases lies in the inherent advantages of any chromatographic separation, such as the speed of the analysis, the possibility to analyze or purify the enantiomers in complex

mixtures, the reproducibility of the analysis and its flexibility. Moreover, analytical chromatographic systems can be adapted to preparative separations, in which pure enantiomers can be collected.

In addition to their distinct practical applicability, chiral stationary phases can uniquely contribute to studies of the nature of molecular recognition. Since the differential retention of enantiomers in the chromatographic system employing chiral stationary phases can be attributed only to chiral discrimination by the chiral sites, these interactions can be isolated and explored. It has been shown that chromatographic parameters obtained by chiral stationary phases can be sensitive to very subtle differences between the enantiomers. Chiral stationary phases can be tailor-made to accommodate specific studies of chiral recognition between molecules. A review by Taylor and Maher[184] describes in detail the principles underlying chiral discrimination by the various chiral chromatographic systems, utilizing chiral agents either in the mobile or the stationary phase. Another review by Gubitz[185] describes the application of chiral stationary phases to chiral drugs, emphasizing the main principles of chiral discrimination of the various categories of stationary phases known so far.

In addition to its use in the analysis and detection of illicit drugs, the versatility and simplicity of capillary electrophoresis is leading to its increasing application in the pharmaceutical industry.[186, 187] Of particular relevance is the ability to develop methods which are capable of resolving optical isomers. In some respects the limiting factor is more on the detection side of the technique and the advances in capillary electrophoresis over the next few years will probably be in this area. The range of detection techniques commonly employed at present, UV absorption, fluorescence, electrochemical detection

and MS, is being extended and expanded by the application of such techniques as LIF and luminescence-energy transfer using lanthanide ions.[188]

It is well-established that in order to obtain a chiral result from any reaction, it has to contain a chiral component or it has to be subjected to some external chiral influence. A well-known example of this principle is the use of circularly polarized light (CPL) as a chiral agent in certain photochemical reactions, where the handedness of the light determines the handedness of the reaction product. Enantiomers were first distinguished by their optical activity. This observation can be traced back to the early (circa 1815) observations of Biot regarding the ability of optically active samples to rotate the plane of polarization of light. Louis Pasteur deduced in 1848 that the handedness of molecular structure is responsible for optical activity. There are two optical manifestations of molecular chirality that can be studied using modern-day polarimetric instruments. The first is optical rotatory dispersion (ORD), which is the differential retardation of right-circularly (RCPL) versus left-circularly polarized light (LCPL) as it traverses a medium. The other, circular dichroism (CD), is the differential attenuation (absorbance) of RCPL versus LCPL. CD measurements are simpler because they require only the detection of intensity variations. ORD manifests itself primarily far off resonance from any absorption bands while CD dominates near an absorption band. To be CD active, a molecule must be structurally asymmetric and exhibit absorbance. Increased relative absorption of LCPL results in a positive CD signal, while a negative signal is the result of RCPL being more highly absorbed. The most commonly studied molecules are proteins where CD signals are sensitive to protein secondary and tertiary structure. CD is measured with a CD spectropolarimeter, which is able to measure accurately in the far UV at wavelengths

down to 190-170nm. The difference in the left and right handed absorbance is very small (usually in the range of 0.0001 absorbance units). Although CD can monitor quite accurately relative changes due to influence of environment on sample (pH, denaturants, temperature etc.) and is non-destructive, the amount of sample necessary for analysis (200μL of 0.5 mg/mL solution in standard cells) is a limitation of the method in terms of its sensitivity. Another consideration is that oxygen absorbs strongly below about 200 nm, so very extensive purging with pure (oxygen-free) nitrogen (>16 L/min) is necessary for these measurements. The requirement for very dilute, non-absorbing buffers to allow measurements below 200 nm is an added drawback to this procedure. As a consequence of these limitations, enantiomeric resolution with the use of chiral light still requires extensive exploration.

The use of CPL for the preferential production of a chiral compound was proposed in the 19th century by Le Bel and by van't Hoff.[189, 190]. This idea was confirmed in the early 1900's, initiating the field of asymmetric photochemistry, which has been a subject of extensive reviews.[191, 192] Photochemistry with CPL[193, 194] led to the partial destruction or the optical activation[195] of racemic mixtures as well as asymmetric syntheses.[196, 197] Our vision of enantiomeric resolution can be considered in the context of asymmetric photodestruction, as reported by Kagan,[198] who achieved 20% optical purity by carrying out photolysis of racemic camphor to 99% completion.

The sections that follow describe the concept of polarization control to produce chiral pulses and our attempts to generate such pulses with the intention of triggering differences in the photoionization and fragmentation of enantiomeric molecules.

6.1 Polarization Control

The electric field vector of a plane wave propagating in the positive z direction may be resolved into two orthogonal components, Ex and Ey. Depending on the relative amplitude and phase (ϕ) of Ex and Ey, the plane wave may be linearly, circularly or elliptically polarized. The magnitudes and phases of field components can be described by the equation,

$$E = [xE_x \exp(i\phi_x) + yE_y \exp(i\phi_y)]\exp[i(kz - \omega t)] \qquad 6.1$$

When Ex and Ey are in phase, their strengths are always equal or related by a constant ratio, so the direction of the electric vector will always fall on a single line in the plane. This is linear polarization. The direction of this line will depend on the relative amplitude of the two components. This direction can be in any angle in the plane, but the direction never varies. When the two orthogonal components have exactly the same amplitude and are exactly 90° out of phase, the light generated is circularly polarized. In this case one component is zero when the other component is at maximum or minimum amplitude. The direction of rotation is dependent on which of the two phase relationships exists. Figures 6.1 and 6.2 depict linear and circular polarization.

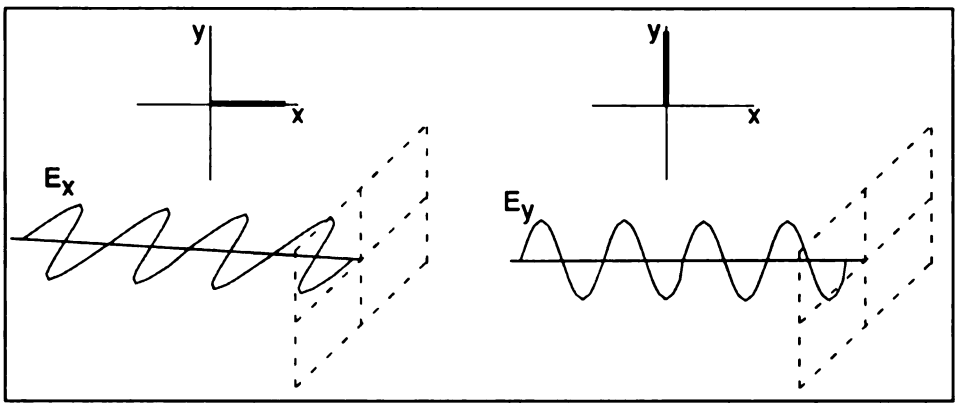

Figure 6.1. Linear polarization. If the vector of the electric field (measured at a fixed point of space) oscillates along a straight line then the waves are called plane polarized or linearly polarized waves. Here, a wave is polarized in a horizontal (left) or vertical plane (right).

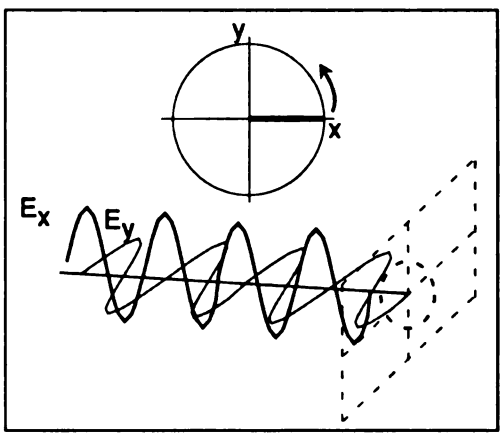

Figure 6.2. Circular polarization. The superposition of two waves that have the same amplitude and wavelength and are polarized in two perpendicular planes with a phase difference of 90° between them generates circularly polarized light. A phase difference of 90° means that when one wave is at its peak, the other one is just crossing the zero line. At any fixed point in space that is in the line of propagation of this wave, the electric field vector rotates in a circle while its length remains constant. In this cartoon, the electric field vector rotates counter-clockwise when looked at from the direction of propagation. The light generated in this case is left circularly polarized. Clockwise rotation of the field vector generates right circularly polarized light.

When the two components are not in phase and either do not have the same amplitude and/or are not 90° out of phase are elliptically polarized because the sum electric vector in the plane will trace out an ellipse.

The generation of circularly polarized femtosecond pulses at the sample position called for tests on two different techniques for delivering polarized laser pulses. The first technique employs the conventional method of using a quarter waveplate (QWP) to convert linearly polarized light (LPL) to CPL. The second technique takes advantage of the SLM to introduce phase functions that could produce either LPL (horizontal or vertical) or CPL (LCPL or RCPL).

6.1.1 QWP Technique

When light propagates through a medium such as glass its speed is reduced by the ratio v/c = 1/n, where c is the speed of light in vacuum and n is the index of refraction of the medium. In uniaxial birefringent materials such as crystal quartz, there are two indices n_o and n_e ("ordinary" and "extraordinary"). n_o applies to light polarized perpendicular to the optic axis of the crystal while n_e applies to light polarized along the optic axis. These indices are a function of wavelength and temperature. n_o and n_e differ by an amount sufficient to produce phase shifts between polarization components, as utilized in waveplates. Passing plane polarized light (or LPL) through a birefringent plate (in the z-direction) splits the light into two plane polarized beams oscillating along different axes (fast along x, slow along y). When one of these beams is retarded by 90°, the two beams, which become 90° out of phase are added together, and result in CPL in one direction. By inverting the two axes such that the alternate beam is retarded, CPL in the other direction is generated. A QWP (see Figure 6.3) consists of a carefully adjusted thickness of a birefringent material such that the light associated with the larger index of refraction (n_e, slow axis) is retarded by a quarter wavelength with respect to that

associated with the smaller index (n_o, fast axis). The material is cut so that the optic axis is parallel to the front and back plates of the plate. Adjusting the plane of the incident light so that it makes a 45° angle with the optic axis gives equal amplitude to waves propagating in the fast and slow axes. Any LPL which strikes the plate will consequently produce CPL.

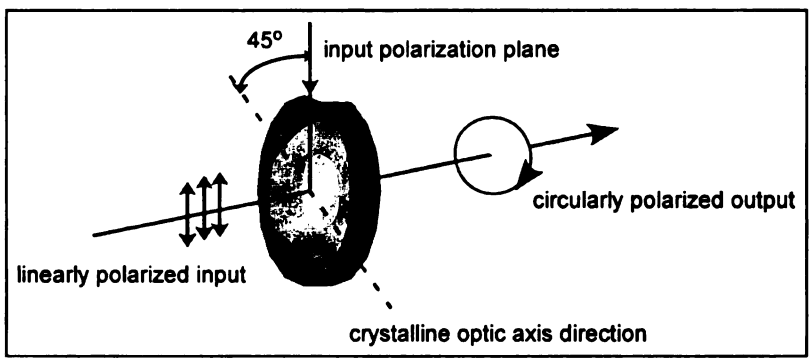

Figure 6.3. Polarization conversion by a quarter waveplate.

To maintain linear polarization with a QWP in place, the slow axis is oriented at a zero degree angle with the optic axis. This condition generates horizontal LPL. When the slow axis is oriented at 90° relative to the optic axis, the light produced is vertical LPL.

Defects in a QWP can alter the intended state of polarization of light. Small fabrication errors can lead to some deviation from a quarter wave retardance. Polarization properties of this optical element can vary with the angle of incidence, temperature, or with the wavelength of light. The narrow free spectral range of QWPs restricts their operational usage. Misalignment of this polarization element would also lead to defects in the polarization condition of the emerging light.

6.1.1.1 Experimental Validation of Polarization Condition

In order to test the polarization condition of a laser beam going through a QWP, measurements of the intensity of the fundamental laser wavelength were taken. A QWP was mounted a few inches from the last component of the pulse shaper. A polarizer was then placed after the QWP. A spectrometer was used to measure the laser intensity. Two different phase functions were introduced to the SLM – one where all phase values (128 pixels) corresponded to zero (designated as BP-0), and the other where all phase values were equal to π (designated as BP-π). In our femtosecond laser system, the input to the pulse shaper has a stable, well-characterized linear polarization. Light that enters the SLM is horizontally polarized. The output polarizer of the SLM was purposely removed with the intention of synthesizing shaped pulses with frequency-dependent polarization. The introduction of a flat phase function (BP-0) to the SLM allows only horizontal LPL to go through and exit the pulse shaper. On the other hand, when BP-π is etched onto the SLM, only the vertical component of light is allowed to leave the shaper.

Figure 6.4 illustrates polar plots of the measurements made when the polarizer was rotated in increments of 20 degrees. When the QWP was oriented at 0°, the results were as expected for LPL (left). BP-0 delivered horizontal LPL and BP-π generated vertical LPL. The imperfection in the measurements obtained in terms of non-symmetrical intensities may be attributed to the not nearly perfect alignment of the optics leading to the detector. The results for CPL were a cause for concern. When the QWP was rotated to 45°, the light generated was clearly not circularly polarized (Figure 6.4, right). Although BP-0, which contributes to the horizontal component of the light,

seemed to produce elliptical polarization, the contribution made by the vertical component (BP-π) drastically affected the polarization condition of the outgoing light. Moreover, the output spectral polarization was distorted by elements with spectrally dependent transmission or reflection, such as the diffraction grating component of the pulse shaper or the dielectric mirrors in the setup. The effect of these elements on polarization cannot be easily compensated for by the use of standard polarization compensators.

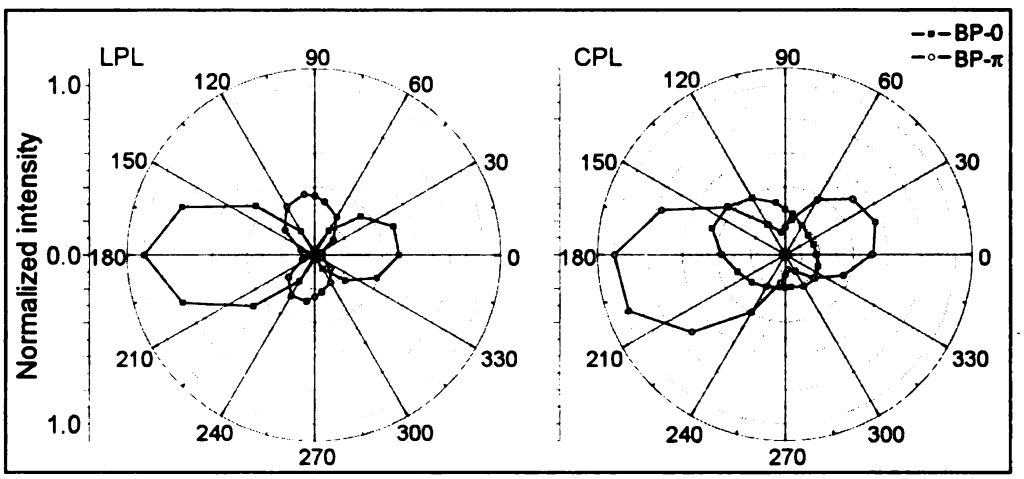

Figure 6.4. Polar plots representing measurements for LPL and CPL generated from a QWP. Left. Horizontal (BP-0) and vertical (BP-π) polarization plots show definite but slightly warped production of LPL. Right. Even when retardance of the QWP is modified to conform to specifications for modifying polarization, the light generated is not circular.

6.1.2 LQ-shaper Technique

The other polarization modification technique used involved the use of the pulse shaper to introduce the retardance corresponding to the production of either LPL or CPL. Computer-controlled femtosecond polarization pulse shaping was first reported by Brixner and Gerber in 2001, where a 256-pixel double mask SLM pulse shaper was used to modulate the degree of ellipticity as well as the orientation of the elliptical principal

axes within a single laser pulse.[199] The light's polarization state reaches different linear and elliptical orientations with varying degrees of ellipticity while keeping intensity levels in the two polarization components equal. As noted by Brixner and Gerber, full control of the temporal polarization of ultrashort pulses requires four independent degrees of freedom for each frequency component: total intensity, total phase, ellipticity, and orientation.[199, 200] Silberberg used three shapers to control the polarization state while keeping spectral intensity constant.[201]. The method used in this section, which, in the interim, is named the LQ-shaper technique, utilizes a digital binary approach to manipulate the electric field of the laser. The incident x-polarized light (*Ex*) exits with field components (*Ex'*, *Ey'*) that depend on the phase retardance (ϕ_A and ϕ_B) introduced by the LQ elements whose slow axis is oriented at 45° and -45°. The generation of linearly polarized output along the x (horizontal) or y (vertical) axes is based on the equations: $E_x^{'} = (1/2)E_x(e^{i\phi A} + e^{i\phi B})$ and $E_y^{'} = (1/2)E_x(e^{i\phi A} - e^{i\phi B})$. For LCPL or RCPL, the field components are $E_L^{'} = \sqrt{1/2(E_x - iE_y)}$ and $E_R^{'} = \sqrt{1/2(E_x + iE_y)}$. The binary states that were used to generate the desired phase, amplitude ($T=|E_x|^2$) and polarization are listed in Table 6.1.

Table 6.1. Phase-Amplitude Modulation for LPL and CPL

Binary State	**Phase**	**Amplitude**	**LPL**	**CPL**
0	$\phi = 0$	T = 1	$E'_x = 1, E'_y = 0$	$E'_L = 1, E'_R = 0$
1	$\phi = \pi$	T = 0	$E'_x = 0, E'_y = 1$	$E'_L = 0, E'_R = 1$
$\phi_A^{(0)}, \phi_B^{(0)}$	$\phi = 0, \phi = 0$	T = 0, T = 0	$E'_x = 0, E'_y = 0$	$E'_L = \pi/4, E'_R = -\pi/4$
$\phi_A^{(1)}, \phi_B^{(1)}$	$\phi = \pi/2, \phi = \pi/2$	$T = \pi/2, T = -\pi/2$	$E'_x = 0, E'_y = \pi$	$E'_L = -\pi/4, E'_R = \pi/4$

6.1.2.1 Experimental Validation of Polarization Condition

The measurements made using the LQ-shaper technique indicated much better control over the outgoing polarization condition of the laser. For this exercise, a polarizer was placed in the beam's path after the pulse shaper, and the laser intensity was recorded with a spectrometer. The polarizer was yet again rotated in 20° increments while running the phases BP-0 or BP-π. The results of the measurements are shown in Figure 6.5.

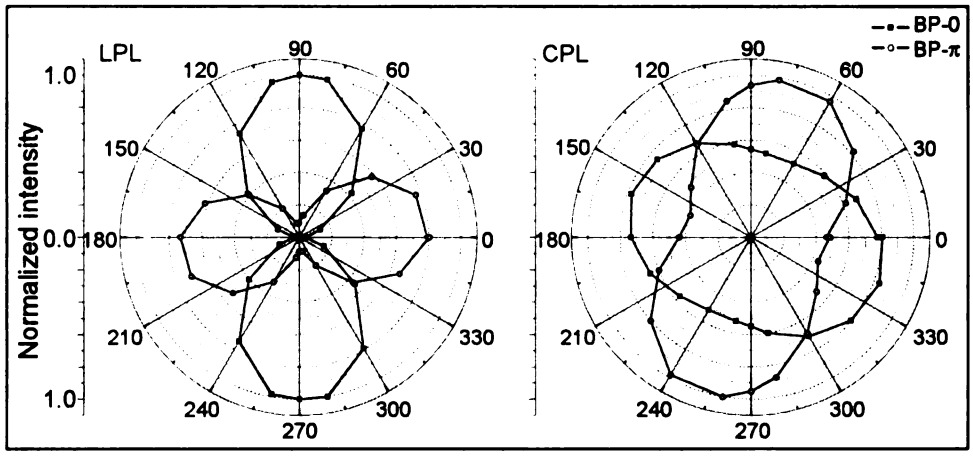

Figure 6.5. Polar plots representing measurements for LPL and CPL generated from the LQ-pulse shaper technique. Left. Horizontal (BP-0) and vertical (BP-π) polarization plots show definite production of LPL. Right. When the program is modified to produce circular polarization, the light generated is elliptical.

Compared to the QWP measurements, the plots show more accurate and symmetrical production of LPL. Although the results for CPL indicate elliptical polarization, they give the impression that the potential of the LQ-shaper technique to deliver the required polarization is much more reliable than the QWP technique.

6.2 Concept: Chiral Pulses and Binary Polarization

The prospects for a wider range of applications of laser control have increased further due to innovations in pulse shaping technology. Femtosecond polarization pulse shaping[199] allows the manipulation of electromagnetic waves in a fundamentally new way. The polarization state of light, as well as the intensity and oscillation frequency, can be varied as a function of time within a single femtosecond laser pulse. The following sections (6.2 and 6.3) exploit the possibility of experimentally realizing enantiomeric resolution by controlling the polarization state of femtosecond laser pulses while introducing binary functions at the SLM.

A number of theoretical studies have proposed the use of lasers for the resolution and synthesis of optically active compounds. Shapiro and Brumer proposed chirality control based on the quantum coherences between rovibronic states to selectively enhance production of right-handed or left-handed optical isomers.[202-204] These theoretical methods have yet to be accomplished in the laboratory. It was predicted that circular[205, 206] or variable elliptical polarization[207] would be required to control the relative populations of enantiomeric molecular excited states. Fujimura, Gonzalez and Manz considered the use of a sequence of linearly polarized short pulses to resolve a racemic mixture.[208-211] Gonzalez later proposed the use of a linearly polarized IR pulse acting on pre-aligned molecules followed by a UV photolysis pulse to distinguish between enantiomeric compounds using MS. This proposal was based on the observed differences in fragment ions when tailored laser pulses were first used to selectively fragment a complex molecule.[32] On the experimental front, the ability to generate intense short pulses with varying ellipticity was introduced by Wefers and Nelson.[212] The research

groups of Gerber[46, 199, 200, 213], Weiner[214], and Silberberg[215] have explored the preparation of phase- and polarization-shaped pulses. Such laser pulses are expected to generate torques on molecules that could lead to more sophisticated control of chemical reactions, including enantiomeric synthesis. However, these goals have not been demonstrated.

Efforts from the Dantus research group towards the use of tailored laser pulses for molecular identification at low concentration[169] have led to the idea of preparing chiral electric fields to induce differential fragmentation of enantiomeric compounds. These laser pulses hypothetically have an electric field with a time-varying ellipticity. By coupling these intense laser pulses with a mass spectrometer, achieving highly sensitive chiral resolution is sought. Photonic control over optically active samples is a dream that has been considered theoretically for two decades.[202-204]

Conceptually, a chiral pulse causes asymmetric switching between right- and left-elliptically polarized light, supposedly leading to differential laser-induced fragmentation and ionization in enantiomerically different molecules. This perception can be traced back to the optical activity of these molecules. The inference that can be made is that a right-handed enantiomer will couple to the chiral electromagnetic field differently than a left-handed enantiomer. Therefore, an intense pulse with a specific succession of right- and left-optical torques would thereby play the role of a chiral photonic enzyme, preferentially cleaving one of the enantiomers. Based on this physical model, the order of the applied set of torques should determine which of the enantiomers is preferentially cleaved.

6.3 Experimental Implementation

In this section, the initial implementation of chiral resolution with polarization shaped laser pulses is introduced. Although the data obtained could have led us to the conclusion of the efficacy of generating chiral pulses for enantiomeric discrimination, subsequent discouraging experimental results gave us a contradicting message.

6.3.1 Polarization shaping with QWP technique: Initial experiments

Experiments were carried out using a TOF mass spectrometer in which the electron ionization source was replaced by amplified femtosecond-laser pulses that were polarization-shaped using a modified phase-amplitude pulse shaper.[90] The laser pulse was dispersed in the frequency domain. This arrangement allows one to control the phase and ellipticity of the light transmitting through each of the 128 pixels in the dual mask pulse shaper. The number of pixels was reduced to 10 super-pixels (each 10 pixels wide, see Figure 6.6) which limited the shaper to produce LPL (horizontal or vertical). A QWP was then used after the pulse shaper to convert the linear polarization, vertical and horizontal, into circular polarization, right and left, respectively.

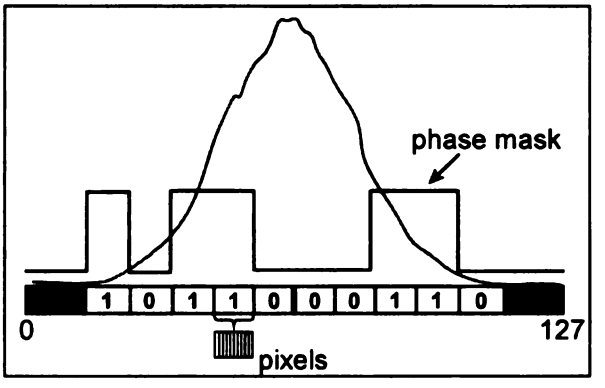

Figure 6.6. Phase mask with 0 or π retardation binned to 10 super pixels, each 10 pixels wide, covering the full spectrum of the fundamental laser pulse. The SLM used has 128 pixels.

The binary polarized shaped pluses were then focused on a small concentration of molecules in the gas phase (approximately 10^4 molecules interact with each laser pulse). The resulting ions and fragment ions were detected and identified by their TOF to the detector. Theoretically, the combination of binary shaping and polarization changes with the QWP results in fields with rapidly switching CPL, as shown in Figure 6.7. The electric fields shown are for the binary polarization pulse BP167, which was used to obtain most of the initial data in this report. When only half of the field is flipped to y polarization, the resulting fields are simpler to visualize. Two such cases (xy and yx) are shown. The prevalent rotation of the field is indicated with arrows.

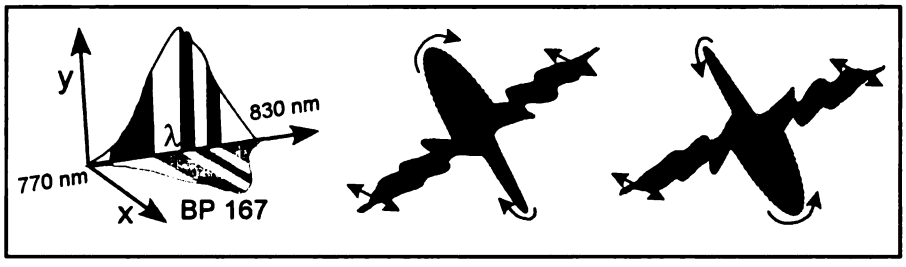

Figure 6.7. Electric fields for binary polarization pulse BP167 for right and left circular polarization.

Rotation of the optical-axis angle of the QWP allowed us to determine the ellipticity of polarization of the pulses used in the experiment. Circular polarization was obtained when the QWP was oriented at 45°. When oriented at 90°, linear polarization was attained. Changing the optical axis angle provided a reliable control for our experiments because it only affected the polarization of the beam, without influencing other variables such as energy or dispersion.

In order to find the greatest enantiomeric specificity, an experimental evaluation of the effect of 512 different circularly polarized shaped pulses on the relative peak ratios of the different fragment ions of our samples was first performed. These pulses correspond to half of all possible 10-bit polarization functions that can be obtained by combining right- and left-circular polarization. From these 512 experiments, the pulses that gave the greatest difference in ion product ratios (one fragment ion peak vs. another peak) between the right-handed (R-) and left-handed (S-) enantiomers were obtained. Mass spectra for both compounds were then generated using these pulses. The binary polarization function BP167 was among those that resulted in the highest contrast between the compounds.

The standard electron ionization mass spectra[171] for the enantiomeric compounds tested, (R)-(+)- and (S)-(−) α-methyl-benzenemethanol (BME) (specific rotation,(R)-(+)-BME = +42°, (S)-(−)-BME = −42°), are shown in the top panel of Figure 6.8, with both enantiomers giving almost identical results. The peaks A and B represent the fragment ions at *m/z* 51 and *m/z* 107, respectively. The mass spectra of the enantiomers obtained using polarization-shaped femtosecond-pulse excitation are shown in the bottom.

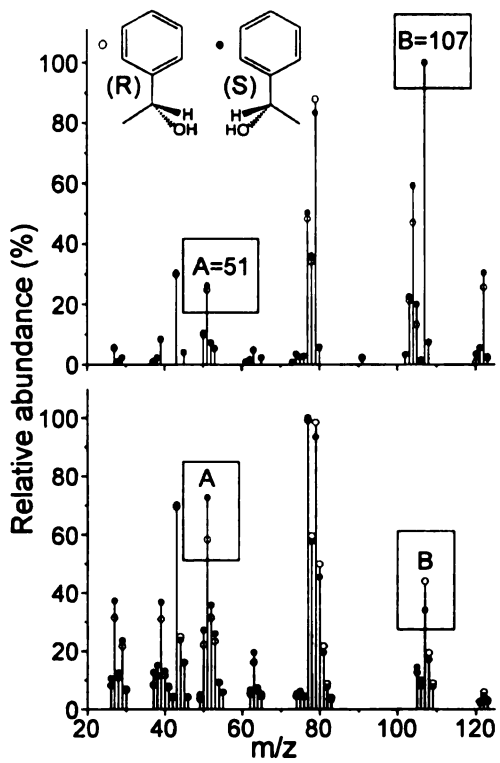

Figure 6.8. Mass spectra of α-methyl-benzenemethanol (BME). Top: electron ionization spectra of R- (open circles) and -S-BME (black circles). Bottom: special fragmentation mass spectra of R- and S-BME using shaped laser pulses with circular binary polarization. Peaks A and B refer to fragment ions at *m/z* 51 and 107, respectively. The ratio of intensities of these peaks was used to differentiate the enantiomers. Inset: structures of the R and S enantiomers of BME.

The chemistry involved in the photoionization and fragmentation of the above molecule is shown in Figure 6.9. The molecular ion peak at *m/z* 122 ($C_8H_9OH^+$) was significantly reduced with laser pulse excitation (~120 μJ/pulse) when compared to electron ionization, leading us to speculate that ionization of the molecule with TL pulses was quite extensive.

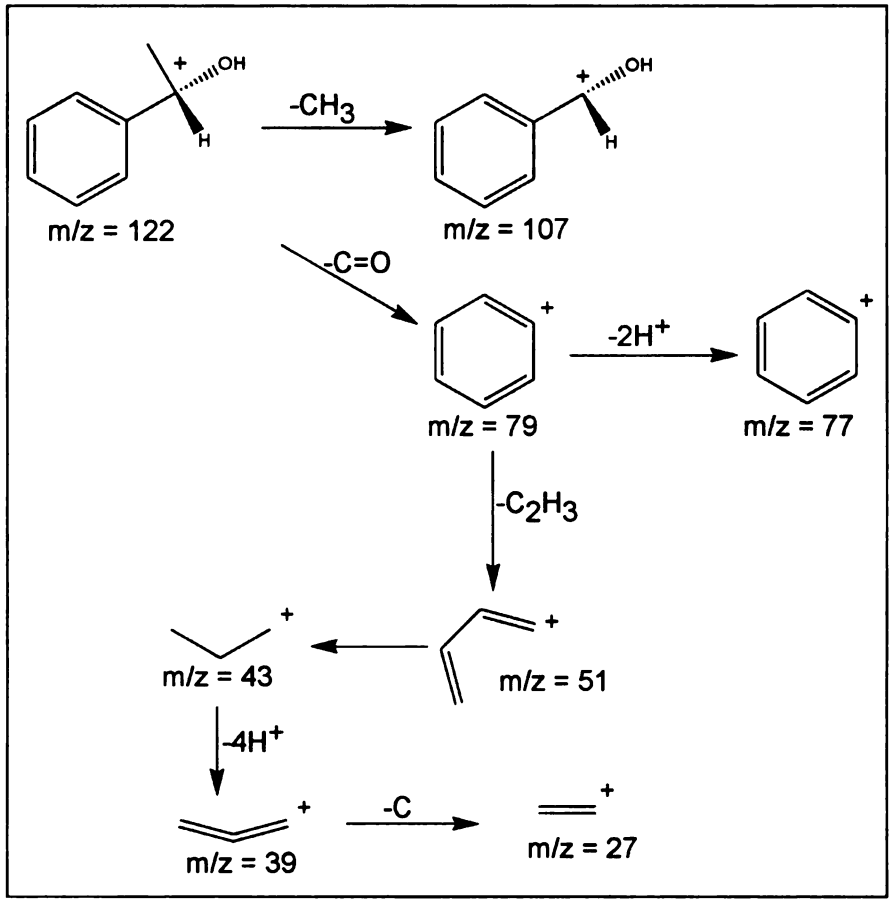

Figure 6.9. Reactions involved in the fragmentation of BME

The dominant fragments were at *m/z* 77 ($C_6H_5^+$) and 79 ($C_6H_7^+$), which are also substantial fragments in the electron ionization mass spectrum. The abundances of the smaller fragments with peaks at *m/z* 27($C_2H_3^+$), 43 ($C_3H_7^+$) and 51($C_4H_3^+$) were enhanced by femtosecond-laser laser excitation. The analysis in this section concentrates on two of the peaks, a small molecular weight fragment at *m/z* 51 (designated here as A) and a large fragment ion corresponding to loss of a methyl fragment with *m/z* 107 ($C_7OH_7^+$, designated as B). Figure 6.8 highlights the substantial difference in the intensities of peaks A and B between R- and S-BME when circularly polarized BP167 pulses are applied. The A/B ratio obtained for R-BME was about 1.3. A significant increase (~2.2)

in the A/B peak ratio was obtained when measurements were made on S-BME. These values correspond to a 60% difference in A/B ratios between the two enantiomers.

The statistical significance of these initial results is apparent in Figure 6.10 where one hundred mass spectral measurements are made for each enantiomer using BP167. The histogram representation of these measurements shows that the S enantiomer undergoes greater fragmentation than its right-handed counterpart. This difference vanished, as expected, when the optical axis of the QWP was rotated to yield linear polarization-shaped pulses (BP167) (Figure 6.10, bottom).

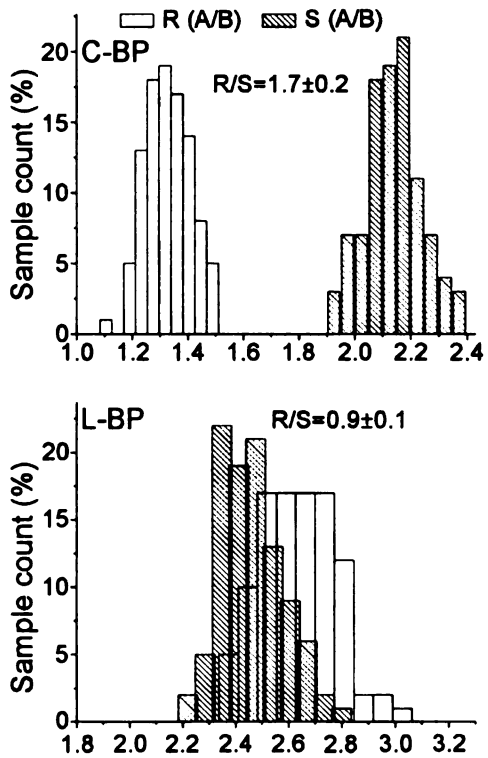

Figure 6.10. Statistical evaluation of phase and polarization shaping for enantiomeric selectivity. Top: histograms representing 100 measurements for each enantiomer using circularly polarized (BP167) laser pulses. Bottom: histograms representing 100 measurements for each enantiomer using linearly polarized (BP167) femtosecond laser pulses.

Analysis of the initial experiments showed that the fragment ion at *m/z* 107 in BME, corresponding to the loss of a methyl group, exhibited the greatest sensitivity to the chiral laser pulses. Pure RCPL or LCPL did not achieve a significant level of asymmetric photodestruction, this being consistent with previous attempts.[216] It was also observed that the number of polarization flips introduced by the shaper correlated with the degree of contrast observed. This indicates the possibility of higher levels of discrimination if polarization phase functions with higher bit-resolution are used. Assessment of a number of electric fields that were found capable of enantiomeric resolution showed a linear polarization component that preceded the large rotating component, analogous to a propeller. The direction and curvature of the propeller component were believed to influence enantio-selective photochemistry. The high selectivity shown in these asymmetric photodestruction experiments cannot be explained based on the circular dichroism of the sample. The use of intense laser fields inducing multiphoton excitation has been shown to increase the anisotropy factor by two orders of magnitude.[217]

6.3.2 Problems encountered with QWP technique

Although this technique initially indicated the potential to indicate differences between two enantiomers that are large enough to be able to distinguish between them, the question regarding the possibility of preparing laser pulses capable of resolving enantiomeric pairs remains unanswered. The lack of experimental reproducibility has been the most frustrating obstacle to ascertaining the feasibility of this method for resolving chiral substances. The success of our earlier observations and the ensuing attempts to replicate the results is, for the most part, puzzling. The possibility of an

unmonitored modification in the characteristics of the laser pulse during experimentation may be a contributing factor to the results obtained. Although experimental parameters such as sample pressure, room temperature and laser intensity were closely monitored before the actual data acquisition, the probability that small changes in these parameters could have significantly affected molecular fragmentation is uncertain. The use of a QWP to deliver the desired polarized pulses may have introduced an electric field that affected the molecules significantly. The optic was tilted slightly (angle unmeasured) from its orthogonal (to beam) position to introduce the assumed circular polarization. Very slight deviations from this particular angle may have significantly impacted the results of subsequent experiments.

6.3.3 Polarization shaping with LQ-shaper technique

Due to the nature of the polarized light generated by the QWP technique and the fact that precision was at such an uncompromising standpoint, our next task was to test whether the LQ-shaper technique would be a more feasible and reproducible way to attain enantiomeric discrimination. The experimental implementation was similar to what was done earlier using the former technique, except that the QWP was taken out of the setup, and binary functions were imprinted onto the LQ arrays of the SLM to generate either LPL or CPL. A number of phase functions, including chirp masks were tested.

6.3.3.1 Simple Linear and Circular Polarization

The response of the sample enantiomers to simple pulses tailored to produce combinations of LPL and CPL was first tested. The polarization masks were generated

based on 128-pixel 2-bin resolution binary functions. Sixteen masks were introduced into the SLM. These masks are shown in Table 6.2.

Table 6.2. Two-bin binary polarization masks

SLM pixel 1 to 64	SLM pixel 65 to 128
Linear horizontal	Linear horizontal
Linear horizontal	Linear vertical
Linear vertical	Linear horizontal
Linear vertical	Linear vertical
Left circular	Left circular
Left circular	Right circular
Right circular	Left circular
Right circular	Right circular
Linear horizontal	Left circular
Left circular	Linear horizontal
Linear horizontal	Right circular
Right circular	Linear horizontal
Linear vertical	Left circular
Left circular	Linear vertical
Linear vertical	Right circular
Right circular	Linear vertical

Figure 6.11 shows mass spectra collected when the mask right circular-left circular was applied on R- and S-BME. The differences in relative yields for both enantiomers appear significant, especially the absence of the peak at *m/z* 91 (tropylium ion) in the R- enantiomer. There may be a slight effect of background on the heights of each fragment ion in the plot below; however, it is very clear that the tropylium ion is

present in the S- enantiomer. Although this could be an indication of successful chiral recognition, the reproducibility factor is still a main constraint. A major dilemma occurs when the set of 16 masks are run several times more. Based on the data gathered, it seems that as the S- enantiomer vapor is irradiated longer with the laser, the tropylium ion peak diminishes in yield. This occurrence may be a major factor in elucidating the lack of reproducibility in the data. Why this phenomenon occurs is an issue that needs further contemplation.

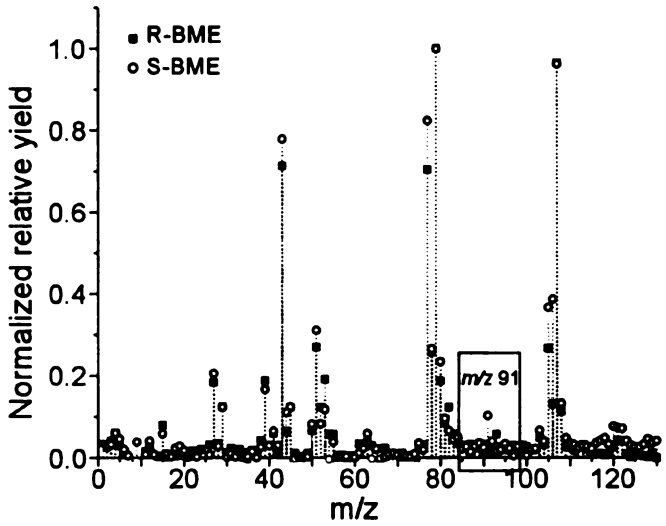

Figure 6.11. Collected mass spectra of R- and S-BME with right circular and left circular polarization combination. The spectra were normalized to the highest fragment ion peak at *m/z* 79. Note the presence of the peak at *m/z* 91 (encased) for S-BME.

6.3.3.2 10-bit Binary Linear and Circular Polarization

The next task was to test more complicated 10-bit BP functions generated to produce either LPL or CPL. The phases were prepared from a set of 1024 10-bit binary functions, where the first 64 and the last 64 phases from this original set were picked to create a new phase list – a set consisting of 128 phase functions repeated ten times. This time, no tropylium ion was observed in either of the enantiomers. However, with all ion

peaks normalized to the *m/z*107 fragment ion peak intensity, the S-enantiomer seemed to be generating higher yields of the lower-mass major fragment ion peaks (*m/z* 43, 51, 77 and 79). Figure 6.12 shows the fragmentation patterns observed when left circularly polarized TL pulses (left) and circularly polarized binary (right, phase shown in inset) shaped pulses were used. Once again, although there is a clear distinction between the two samples tested, the experiment lacked reproducibility. It is interesting to note that the intensity of the 107 peak decreases significantly from TL to shaped pulses. In addition, while this decrease is observed, increases in the yields of the lower-mass fragment ions are also apparent with the polarization shaped pulses.

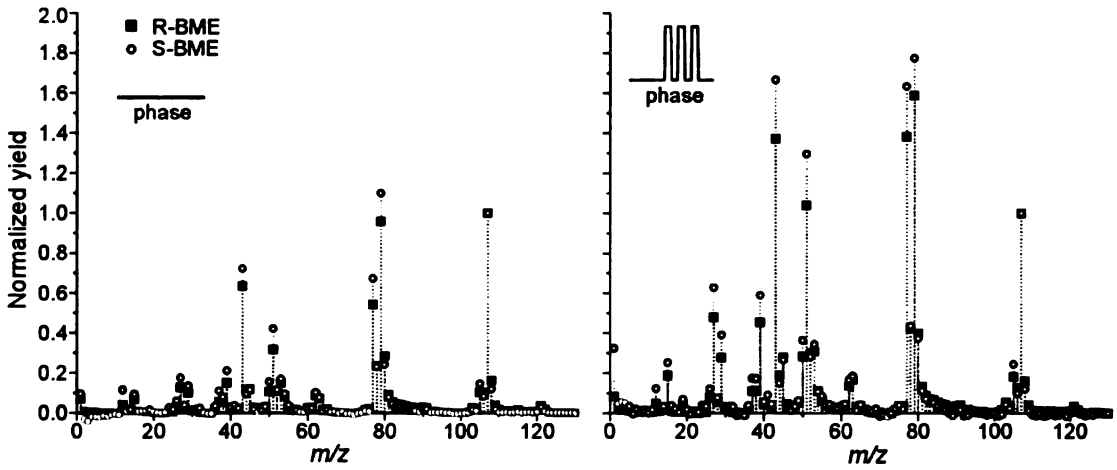

Figure 6.12. Mass spectra of R- and S-BME using 10-bit polarization shaping. Left: observed mass spectra of the enantiomers as a consequence of TL LCPL. Right: observed mass spectra of the same compounds when a more complicated circularly polarized binary function is applied. The structures of the binary functions used are also shown (phase).

When the intensities of the fragment ions are plotted against the BP functions tested, the differences between R-BME and S-BME are more apparent. Figure 6.13 shows three such plots. Based on the observed data, differences in intensities of peak 107

(A) occur in the middle section of the set of 128 phase functions. In the case of peak 51 (B), the bigger differences lie primarily at the edges (first and last) of the set of functions. The ratios between the peaks at *m/z* 51 to those at *m/z* 107 are shown in Figure 6.13C.

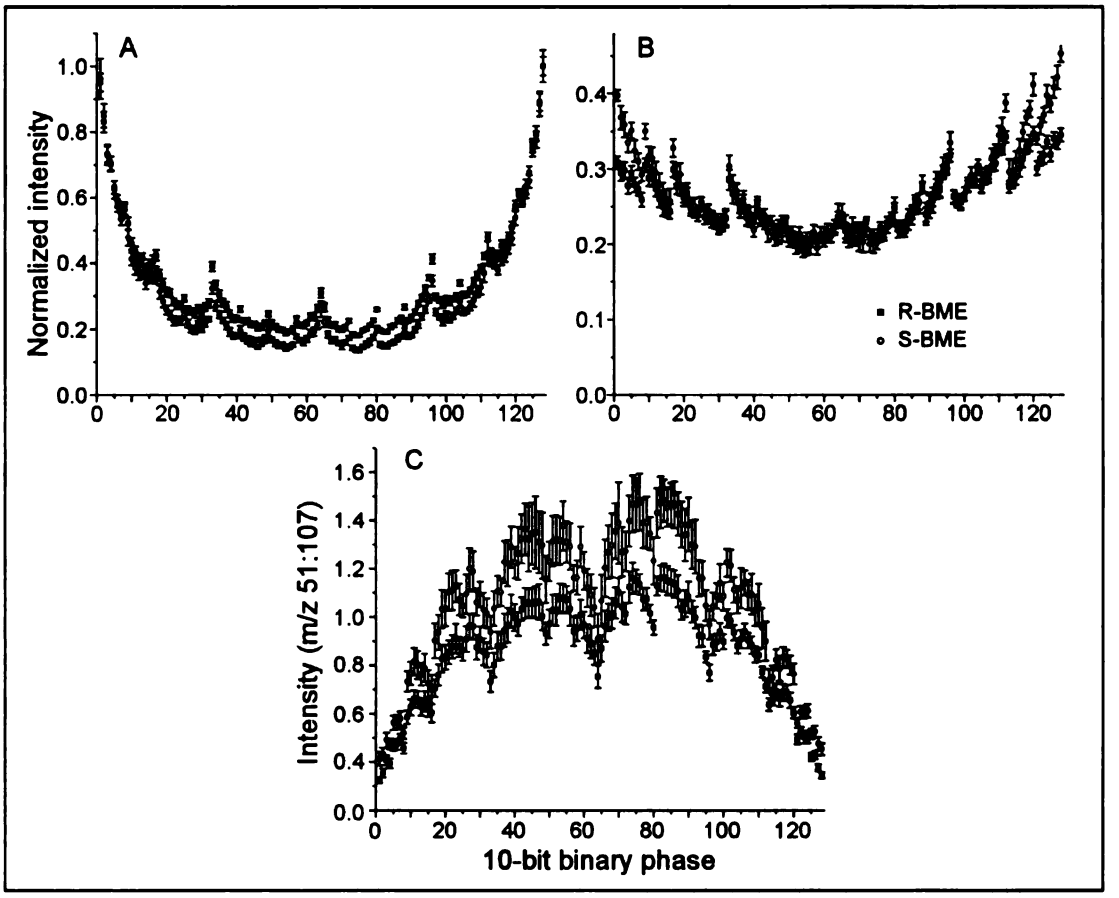

Figure 6.13. Changes in intensity of fragment ion peaks at *m/z* 107 (A) and *m/z* 51 (B) as 128 circularly polarized binary functions are scanned across the SLM. The intensities were normalized to that of *m/z* 107. C. Plot of the ratios between *m/z* 51 and 107 for the 128 polarization shaped pulses. Error bars indicate standard deviation of data (n=10).

These ratio differences (R/S) range from 1.13 ± 0.04 to 1.34 ± 0.06. It is also apparent from Figure 6.13 that as the binary function increases in complexity (middle section of phase set), the ratio differences between the enantiomers also increase; however, the problems of noise and baseline measurement inaccuracies become more well-defined and the issue of reproducibility is again a matter of concern.

The symmetrical parabolic traces observed in the same figure show that the intensity of fragmentation is independent of the direction of polarization of the pulses (LCPL to RCPL). Although the expected reversal in fragment ion peak intensities as the polarization direction was flipped from left to right circular was not observed, the capability of the LQ-shaper method to produce the intended polarization pulses was undeniable.

The experiment was repeated, this time, with a modification in the path length of the beam going towards the entrance of the mass spectrometer. The optical path length was shortened by about 10 feet. The results of this experiment showed that R- and S-BME had no significant differences in fragment ion yields except for the peaks at *m/z* 105 and 106. Figure 6.14 shows the TOF spectra obtained for the samples. Notice the difference in intensities of the fragment ions at *m/z* 105 and 106. It is logical to think that these differences should be expected, especially when the structures of these compounds are considered. Once the hydroxyl group and the hydrogen, which are both attached to the chiral carbon, are removed, the resulting fragments are those with *m/z* 105 and 106. Further fragmentation of the molecular ion eliminates its chiral nature, and thus no differences in the relative yields of the other fragment ions are observed. Unfortunately, a closer look at the standard EI mass spectra of the sample compounds also shows slight differences in abundances of these two fragment ion peaks.

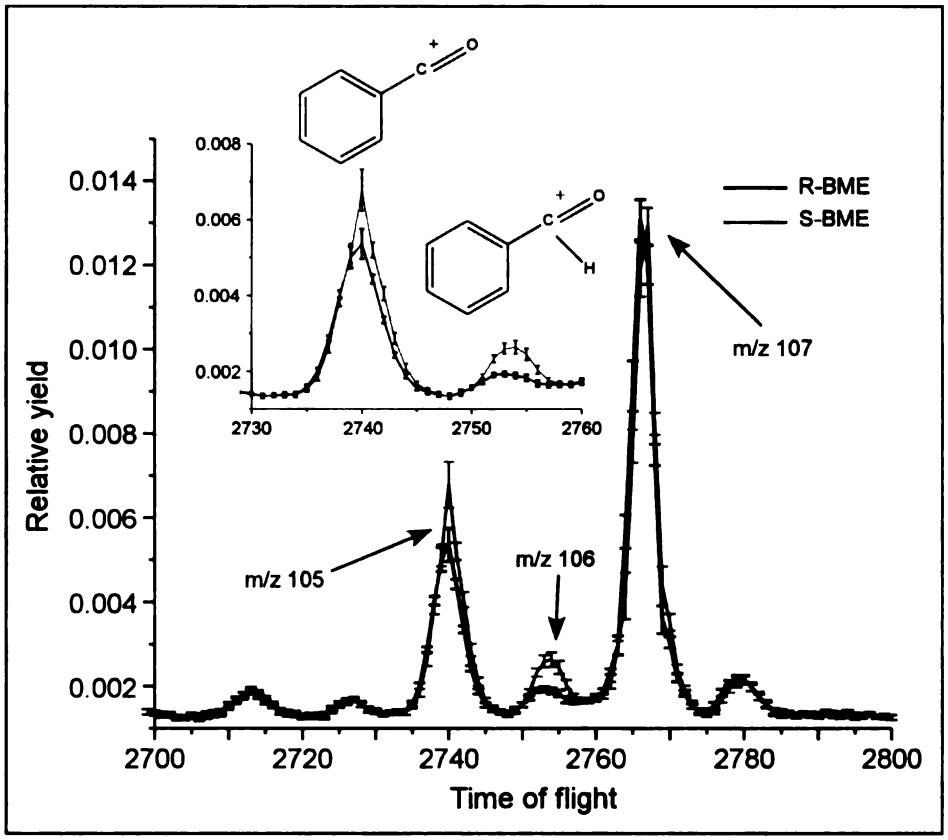

Figure 6.14. Raw TOF data for R- and S-BME showing peaks with intensity differences. The peaks shown represent fragments at *m/z* 105, 106 and 107. The inset zooms in on peaks 105 and 106, highlighting the difference between the two enantiomers.

6.3.3.3 Chirp Combined with CPL

When the order of the different frequency components of the pulse is reversed, a reversal of fragmentation yields of the enantiomers is expected. This hypothesis was tested by introducing circularly polarized chirped laser pulses, including both positive and negative chirp. Mass spectra were collected using the same 10-bit binary polarization functions used in Section 6.3.3.2, with the addition of positive or negative chirp masks.

Much to our disappointment, there didn't seem to be any reversal in the intensities of the fragment ions. Figure 6.15 shows data collected when CPL pulses were chirped to

either +900 or −900 fs^2. The negatively chirped circularly polarized pulses indicated greater fragmentation, with the R enantiomer fragmenting at a slightly higher yield than S-BME. In terms of positively chirped pulses, the S enantiomer appears to have a generally higher yield than R-BME, but this difference is trivial when the noise level of the data is factored in.

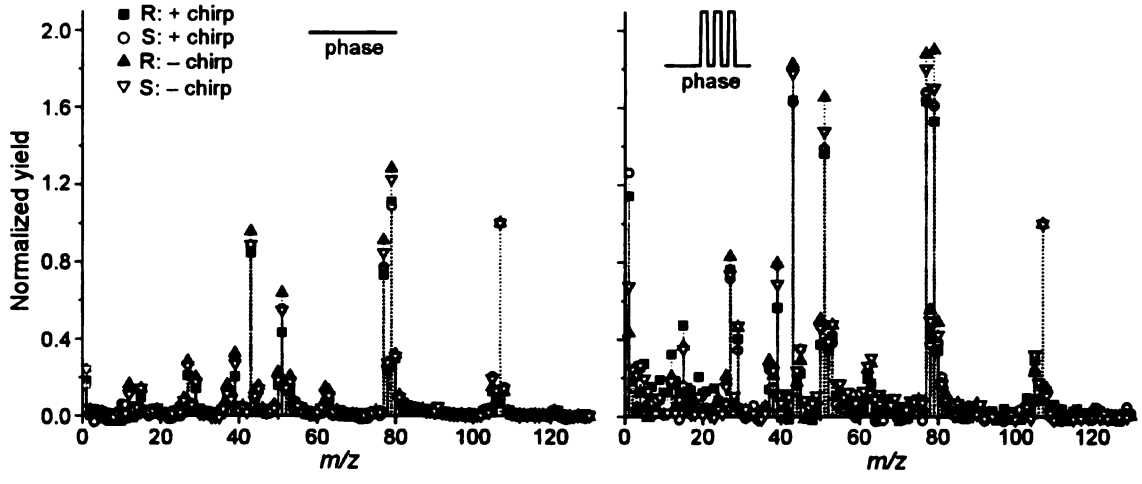

Figure 6.15. Mass spectra of R- and S-BME using chirped 10-bit polarization shaping. Left: observed mass spectra of the enantiomers for positively and negatively chirped left circularly polarized pulses. Right: observed mass spectra of the same compounds when positive and negative chirp are applied in addition to a complicated circularly polarized binary pulse. The structures of the binary functions used are also shown (phase).

Analysis of all data sets recorded showed no significant statistical differences between the enantiomers and between positive and negative chirp effects. While one run of the different polarization masks could highlight differences between R- and S-BME, these differences are reduced considerably when error plots of the mass spectra are constructed. Interestingly, the effect of binary polarization shaping on the increase in yield of the lower-mass fragment ions and the decrease in the *m/z*107 peak, which were also observed in earlier experiments where chirp was not an experimental parameter,

does insinuate that some control over the fragmentation patterns of the molecules studied is possible. The issue of reproducibility is, regrettably, the major obstacle to the success of these experiments. The main source of error in the experiments could be attributed to laser intensity fluctuations which are amplified by about an order of magnitude when taking into account the 6- to 8-photon process initiating ionization and fragmentation. Pulse-to-pulse stability limits the precision with which one can estimate the effect of a particular control experiment. Intensity variations have critical consequence on the statistical evaluation of an experiment. For an *n*th order nonlinear optical experiment, the average value obtained after N measurements on a signal, where fluctuations are of magnitude $\pm\sigma$ is determined by $\pm n\sigma N^{(-0.5)}$.[91]

6.4 Inferences and Future Possibilities for Chiral Pulses

The reliable identification of a large number of enantiomeric species by coherent control calls for further studies. The fact that initial experiments were not completely reproducible requires extensive improvement in the technique and considerable adjustment of experimental parameters. The positive results gleaned from early tests are nonetheless encouraging. The task of distinguishing between enantiomers and the overall intention behind chiral recognition by coherent control are, without any doubt, worth advocating.

CONCLUSIONS

Controlling laser-molecule interactions has become an integral part of developing the future of devices and applications in spectroscopy, microscopy, optical switching, and photochemistry. A number of applications are dependent on multiphoton transitions. Coherent control of multiphoton transitions could bring about a significant improvement of these methods. In microscopy, multiphoton transitions are used to activate different contrast agents and suppress background fluorescence; with coherent control, the potential for selective probe excitation could ascertain its valuability. The potential for two-photon excitation in PDT has been demonstrated by researchers to result in two key benefits: deeper penetration depth of light and new PDT treatments of skin melanoma without the addition of a drug or dye. The successful demonstration of selective two-photon excitation as a tool for molecular recognition is, in my mind, a major accomplishment of coherent control in terms of making an impact in fields other than physical chemistry. With the first few steps towards our vision for biomedical applications accomplished, future endeavors of coherent control research towards selective activation of PDT drugs and noninvasive detection and therapy of cancerous cells should be imminent.

In photochemistry, different dissociative states are accessed through multiphoton transitions. Coherent control could be used to select the reaction pathway and consequently yield specific products. Multiphoton excitation of molecules to highly excited electronic states, each with a different decay pathway, makes laser control of molecular reactivity possible, provided selectivity, combined with the sensitivity of

analytical methods such as MS, can be achieved. The combination of the physical principles of coherent control and the analytical merits of MS could prove useful for future applications in chemical detection.

The prospect of using femtosecond laser control as a means for molecular recognition in the biomedical and analytical fields has been elucidated in this dissertation. Although our objective for enantiomeric resolution has not been realized, the potentially huge impact of successful chiral recognition by coherent control, especially in the biomedical, pharmaceutical and environmental areas, merits anticipation.

APPENDICES

APPENDIX A

Group Velocity Dispersion

When short laser pulses propagate through absorptive or dispersive media, the possibility for dispersion is high. Different frequency components propagate with different velocities in all materials. GVD takes place because the index of refraction of light increases with increasing frequency for most materials in the visible region of the spectrum. This causes the low frequency components in a pulse envelope to propagate faster than the higher frequency components. The pulse envelope is temporally broadened and develops a positive chirp. Conversely, if a pulse travels through an anomalously dispersive medium, high frequency components travel faster than the lower ones, and the pulse becomes negatively chirped, decreasing in frequency with time. The majority of pulse broadening in ultrashort pulse lasers is caused by the positive GVD of the gain medium. The consequence is that a short pulse consisting of many wavelengths is stretched in time. In order to compensate for this effect, negative GVD, where short wavelengths propagate more rapidly than longer wavelengths, is needed. A practical method for doing this is to introduce pairs of prisms into the cavity.[218] Although the prism material will itself contribute positive dispersion, it is possible to configure the prism pairs so that the overall contribution is negative. The figure below illustrates this configuration using four prisms.

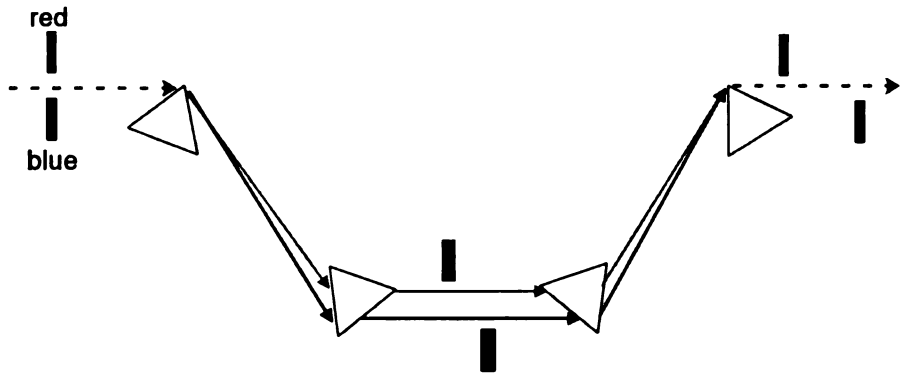

Figure A-1. Prism arrangement to compensate for positive GVD

The arrangement of the prisms in Figure A-1 permits negative GVD to be achieved using materials with positive GVD. Light is spectrally dispersed by the first prism. The lower frequency components of the light must travel through more glass in the second prism and are delayed relative to the high frequency components resulting in negative chirp. A second pair of prisms is needed to spatially recombine the beam. The layout of the four prisms allows the GVD to be adjusted from positive to negative by translating the prisms so that the beam must travel through less glass. The prisms are cut and orientated so that the rays are incident at minimum deviation and Brewster's angle to minimize losses. The total dispersion of the prism sequence is calculated as $D = \frac{\lambda}{cL}\frac{d^2P}{d\lambda^2}$, where L is the physical length of the light path, P is the optical path length. The derivative $d^2P/d\lambda^2$ is a function of the angular divergence, the refractive index of the prism material and the apex separation, l, of the prisms. Provided the prism separation is sufficiently large, the positive dispersion of the material can be balanced. Therefore, by changing the prism positions it is possible to vary the total dispersion of the cavity from positive to negative.

Another way of controlling GVD, without the need of introducing intracavity glass, is by using chirped dielectric mirrors as the source of broadband negative GVD.[219, 220] Chirped mirrors reflect each wavelength from a different depth through the dielectric coating, which is made up of multiple stacks of varying thickness. Such mirrors have facilitated the generation of sub-5 fs laser pulses.[221]

APPENDIX B

Description of components of vacuum system – TOF assembly used for mass spectrometry experiments

A.1. Vacuum System

After a molecule is introduced into the mass spectrometer, the molecule is first ionized and then fragmented. Following this, the ions can be selected and counted. However, for proper operation, the interior of the mass spectrometer must be evacuated. The ion source, mass analyzer (TOF), and detector all are under vacuum. The vacuum system makes it possible for ions to move from the ion source to the detector without colliding with other ions and molecules.

Achieving a vacuum sufficient for the effective operation of our mass spectrometer system requires a multi-step pumping scheme with a rotary mechanical roughing pump followed by a high vacuum diffusion pump and turbomolecular pump (TMP)..

The roughing pump in our TOF-MS system is a mechanical vacuum pump that works in collaboration with the high vacuum diffusion pump in the preliminary stage of the pumping process. The roughing pump is connected to the main chamber of the diffusion pump through a separate pumping line and valve. The chamber is pumped down to a pressure of about 10^{-2} to 10^{-3} torr , at which point the valve to the roughing pump is closed. Then a second valve that connects the diffusion pump to the chamber is opened, at which point the diffusion pump takes over.

The diffusion pump is necessary to attain pressures below 10^{-3} to 10^{-4} Torr. The vacuum diffusion pump in our setup is a stainless steel chamber containing vertically stacked cone-shaped jet assemblies. It works by capturing gas molecules by vaporizing and condensing a pool of low vapor pressure silicone oil located at the base of the chamber. The oil is heated to boiling by an electric heater located beneath the floor of the chamber. The vaporized oil is forced up through a central column in the pump and is vented downward through jets in conical sheets against the inner sides of the pump chamber. As the vapor jet impacts the outer cooled shell of the diffusion pump the gas entrained in the jet flow coalesces, carrying the entrained pumped gases into the base of the pump where the gas pressure is increased and pumped by the rough pump from the diffusion pump outlet. The coil around the pump is for cooling water. The cooling water is necessary to cool and condense the oil fast enough to prevent thermal runaway and permit operation over longer periods of time. With a diffusion pump, vacuum pressures between 10^{-5} to 10^{-8} Torr can be attained.

The TMP is placed in-line with the roughing pump and is used to obtain and maintain high vacuum. This pump works on the principle that gas molecules can be given momentum in a desired direction by repeated collision with a moving solid surface. The TMP effectively functions as a turbine. It rotates very rapidly (10-20,000 rpm) while the turbine wings mechanically pump the residual gasses from the high vacuum. Gas molecules from the inlet of the pump are hit and brought towards the exhaust in order to create or maintain a vacuum. When switched on, this pump generates a characteristic high pitch humming. The machine can be a very versatile pump able to generate intermediate vacuum (~10^{-4} Torr) up to ultra-high vacuum levels (~10^{-10} Torr). When

switched off, a free flow of air can take place through the device (unless some valve is shut), but unlike the diffusion pump, normally no backflow of dirty pump oil debris can take place. The TMP in our system has a pumping speed of 220 L/s.

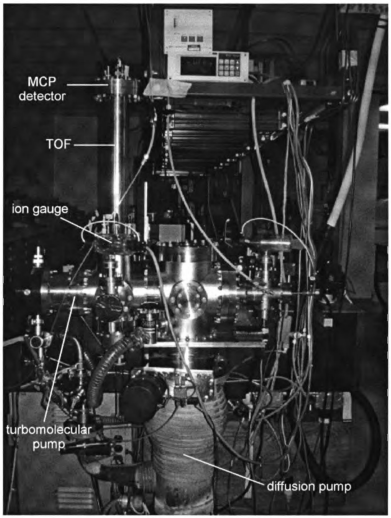

Figure A-2. Major components of TOF mass spectrometry system include the mechanical roughing pump (not shown), diffusion pump, turbomolecular pump, ion gauge, flight tube and the MCP detector.

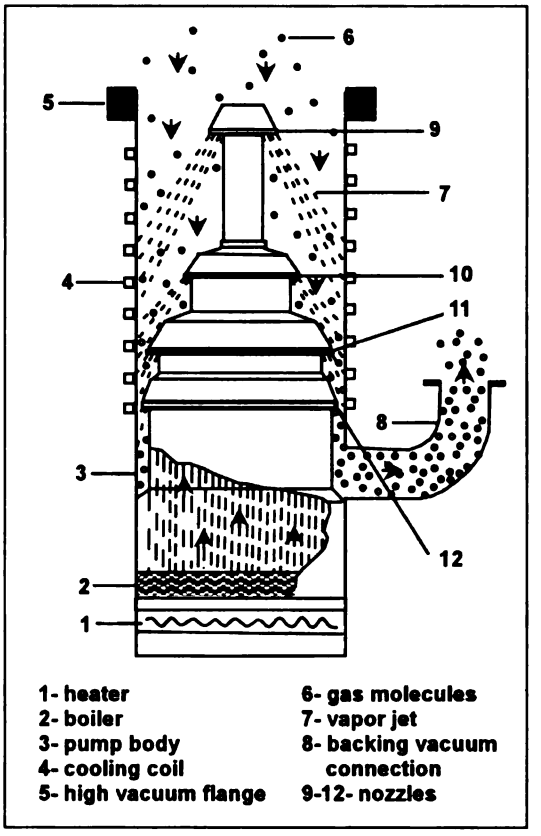

Figure A-3. Diffusion pump mode of operation. A heating coil (1) evaporates the special diffusion pump oil in the boiler (2). The oil vapor then ascends through the centre of the pump and shoots at high speed out of a multi-stage system of concentric ring-shaped nozzles (9-12). The oil vapor shoots out in the shape of a cone (7) and then condensates against the wall of the pump (3), which is cooled by water flowing through the cooling coils (4). The oil then returns into the boiler as a thin film along the wall. The air or other gas in the high vacuum part of the pump (6) is forced to move along with the high speed oil vapor in the different cascade levels and leaves the pump on the low vacuum side of the pump (8).

An Ion Gauge, which is connected to our mass spectrometer assembly, is used to measure pressure. It consists of three distinct parts, the filament, the grid, and the collector. The filament is used for the production of electrons by thermionic emission. A +ve charge on the grid (anode) attracts the electrons away from the filament; they circulate around the grid passing through the fine structure many times until eventually

they collide with the grid. Gas molecules inside the grid may collide with circulating electrons. The collision can result in the gas molecule being ionized. The collector (cathode) inside the grid is -ve charged and attracts these +ve charged ions. Likewise they are repelled away from the +ve grid at the same time. The number of ions collected by the collector is directly proportional to the number of molecules inside the vacuum system. Absolute pressure is determined by the frequency of gas molecules interfering with cathodic electrons attracted to the grid.. The resulting ionization of the gas (collected ion current) is measured to determine the pressure. For most of the MS experiments in this dissertation, the pressure of molecules in the vacuum system ranged from $8x10^{-6}$ to $1x10^{-5}$ torr. The ion gauge was kept on throughout the experiments to allow us to monitor pressure changes.

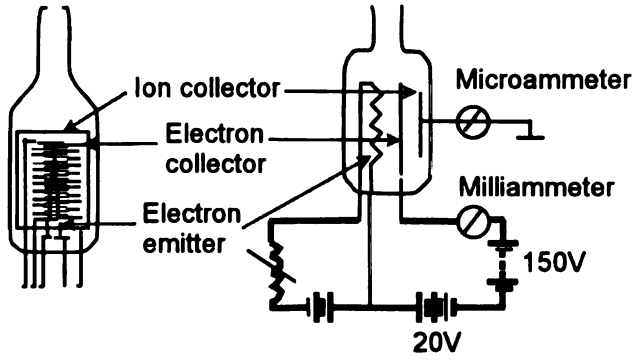

Figure A-4. A typical ion gauge. It has a heated filament biased to give thermionic electrons (70e) energetic enough to ionize any residual gas molecules during collisions. The positive ions formed drift to an ion collector held at about 150V. The current measures gas number density, a direct measure of pressure.

A.2. TOF Assembly (D-677, R.M. Jordan Co., Inc.)

A TOF mass spectrometer uses the differences in transit time through a drift region to separate ions of different masses. It operates in a pulsed mode so ions must be produced or extracted in pulses. An electric field accelerates all ions into a field-free drift

region with a kinetic energy of qV, where q is the ion charge and V is the applied voltage. Since the ion kinetic energy is $0.5mv^2$, lighter ions have a higher velocity than heavier ions and reach the detector at the end of the drift region sooner.

An electric field between the repeller and the extractor electrode accelerates the formed ions past the ground electrode, and through the field-free TOF region (flight tube), and onwards to the detector. The extractor and ground electrodes are thin metal plates with a small opening at the middle. The voltages on the extractor and repeller plates were kept at 1600 and 2500 V, respectively. At the top of the flight tube is a dual plate detector (multichannel plate or MCP) which consists of a material with a very low work function, such that a cascade of electrons is released from the top whenever an ion strikes the lower surface. The subsequent electron pulse from the top of the detector plate strikes an anode, which passes the signal through some amplification electronics to the counting electronics where the pulses are recorded.

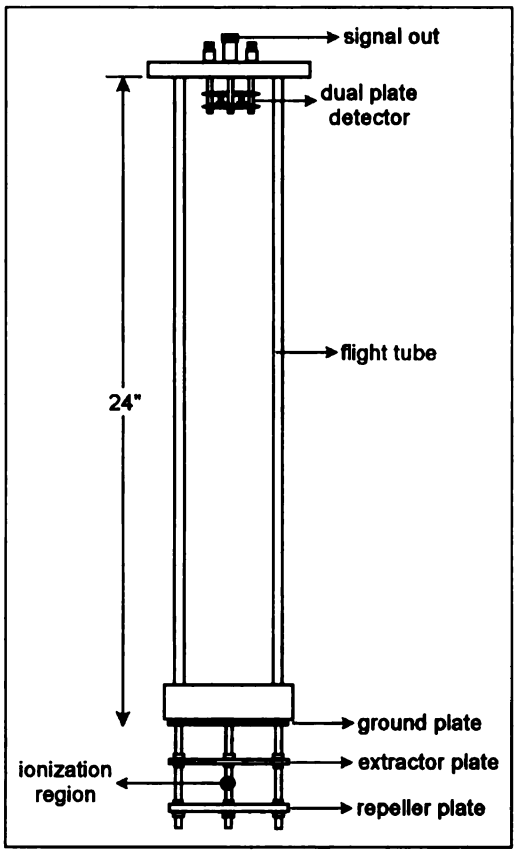

Figure A-5. Lens stack and flight tube assembly. An assembly of grids, steering plates and lens elements mounted on a flange.

The detector used in our mass spectrometry experiments is a C-701 18 mm dual MCP detector (R.M. Jordan Co., Inc.) It has a 50 ohm coaxial output and provides high gain (10^6 to 10^7) with sub-nanosecond rise time. It is fitted with an input grid (90% transparency) wired to an external SHV (standard high volume) coaxial UHV (ultra high voltage) feedthrough that can be operated from external power supplies or voltage dividers. This presents a flat, field free plane to the incoming ions. The maximum voltage across each plate is 1000 Volts (V), with a 1000 minimum gain per plate.

The MCP consists of a two-dimensional periodic array of very-small diameter glass capillaries or channels fused together and sliced in a thin plate. A single incident particle (ion, electron, photon etc.) enters a channel and emits an electron from the

channel wall. Secondary electrons are accelerated by an electric field developed by a voltage applied across both ends of the MCP. They travel along their parabolic trajectories until they in turn strike the channel surface, thus producing more secondary electrons. This process is repeated many times along the channel; as a result, this cascade process yields a cloud of several thousand electrons, which emerge from the rear of the plate. If two or more MCPs are operated in series, a single input event will generate a pulse of 10^8 or more electrons at the output.

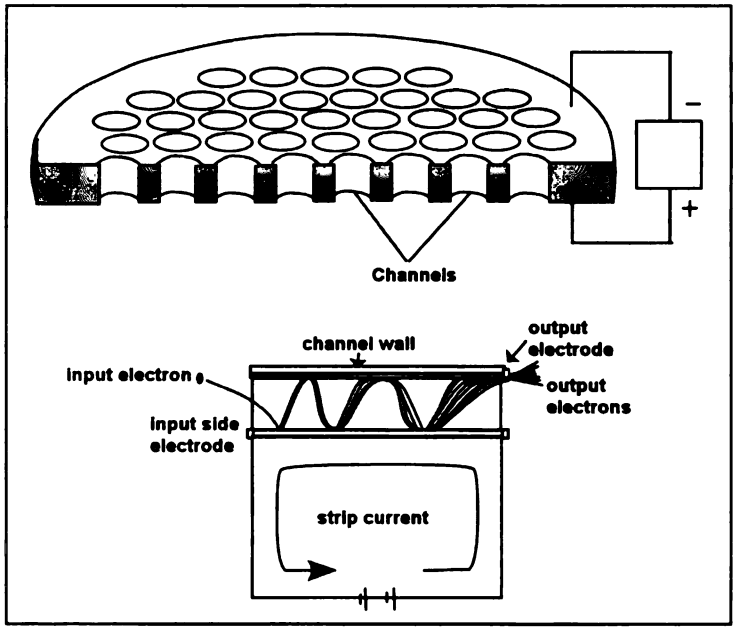

Figure A-6. MCP principle of operation

BIBLIOGRAPHY

BIBLIOGRAPHY

(1) Tannor, D. J.; Rice, S. A. *J. Chem. Phys.* **1985**, *83*, 5013-5018.

(2) Tannor, D. J.; Kosloff, R.; Rice, S. A. *J. Chem. Phys.* **1986**, *85*, 5805-5820.

(3) Baumert, T.; Gerber, G. *Isr. J. Chem* **1994**, *34*, 103-114.

(4) Zewail, A. H.; Casati, G.; Rice, S. A.; Cherqui, M.; Tannor, D. J.; Kobayashi, T.; Rabitz, H. *Adv. Chem. Phys.* **1997**, *101*, 3-45.

(5) Warren, W. S. *J. Chem. Phys.* **1984**, *81*, 5437-5448.

(6) Lin, C. P.; Bates, J.; Mayer, J. T.; Warren, W. S. *J. Chem. Phys.* **1987**, *86*, 3750-3751.

(7) Weiner, A. M.; Leaird, D. E.; Wiederrecht, G. P.; Nelson, K. A. *Science* **1990**, *247*, 1317-1319.

(8) Weiner, A. M.; Leaird, D. E.; Wiederrecht, G. P.; Nelson, K. A. *J. Opt. Soc. Am. B* **1991**, *8*, 1264-1275.

(9) Broers, B.; Noordam, L. D.; Vandenheuvell, H. B. V. *Phys. Rev. A* **1992**, *46*, 2749-2756.

(10) Broers, B.; Vandenheuvell, H. B. V.; Noordam, L. D. *Opt. Commun.* **1992**, *91*, 57-61.

(11) Judson, R. S.; Rabitz, H. *Phys. Rev. Lett.* **1992**, *68*, 1500-1503.

(12) Bardeen, C. J.; Yakovlev, V. V.; Wilson, K. R.; Carpenter, S. D.; Weber, P. M.; Warren, W. S. *Chem. Phys. Lett.* **1997**, *280*, 151-158.

(13) Meshulach, D.; Yelin, D.; Silberberg, Y. *Opt. Commun.* **1997**, *138*, 345-348.

(14) Yelin, D.; Meshulach, D.; Silberberg, Y. *Opt. Lett.* **1997**, *22*, 1793-1795.

(15) Meshulach, D.; Yelin, D.; Silberberg, Y. *J. Opt. Soc. Am. B* **1998**, *15*, 1615-1619.

(16) Baumert, T.; Brixner, T.; Seyfried, V.; Strehle, M.; Gerber, G. *Appl. Phys. B-Lasers O* **1997**, *65*, 779-782.

(17) Brixner, T.; Strehle, M.; Gerber, G. *Appl. Phys. B-Lasers O* **1999**, *68*, 281-284.

(18) Brixner, T.; Oehrlein, A.; Strehle, M.; Gerber, G. *Appl. Phys. B-Lasers O* **2000**, *70*, S119-S124.

(19) Efimov, A.; Moores, M. D.; Beach, N. M.; Krause, J. L.; Reitze, D. H. *Opt. Lett.* **1998**, *23*, 1915-1917.

(20) Efimov, A.; Moores, M. D.; Mei, B.; Krause, J. L.; Siders, C. W.; Reitze, D. H. *Appl. Phys. B-Lasers O* **2000**, *70*, S133-S141.

(21) Takasago, K.; Takekawa, M.; Suzuki, M.; Komori, K.; Kannari, F. *IEEE J. Sel. Top. Quant.* **1998**, *4*, 346-352.

(22) Ohno, K.; Tanabe, T.; Kannari, F. *J. Opt. Soc. Am. B* **2002**, *19*, 2781-2790.

(23) Zeek, E.; Maginnis, K.; Backus, S.; Russek, U.; Murnane, M. M.; Mourou, G.; Kapteyn, H. C.; Vdovin, G. *Opt. Lett.* **1999**, *24*, 493-495.

(24) Zeek, E.; Bartels, R.; Murnane, M. M.; Kapteyn, H. C.; Backus, S.; Vdovin, G. *Opt. Lett.* **2000**, *25*, 587-589.

(25) Zeidler, D.; Hornung, T.; Proch, D.; Motzkus, M. *Appl. Phys. B-Lasers O* **2000**, *70*, S125-S131.

(26) Armstrong, M. R.; Plachta, P.; Ponomarev, E. A.; Miller, R. J. D. *Opt. Lett.* **2001**, *26*, 1152-1154.

(27) Armstrong, M. R.; Plachta, P.; Ponomarev, E. A.; Ogilvie, J. P.; Nagy, A. M.; Miller, R. J. D. *Appl. Phys. B-Lasers O* **2002**, *74*, S127-S132.

(28) Baltuska, A.; Fuji, T.; Kobayashi, T. *Opt. Lett.* **2002**, *27*, 306-308.

(29) Baltuska, A.; Kobayashi, T. *Appl. Phys. B-Lasers O* **2002**, *75*, 427-443.

(30) Legare, F. L.; Fraser, J. M.; Villeneuve, D. M.; Corkum, P. B. *Appl. Phys. B-Lasers O* **2002**, *74*, S279-S282.

(31) Baum, P.; Lochbrunner, S.; Gallmann, L.; Steinmeyer, G.; Keller, U.; Riedle, E. *Appl. Phys. B-Lasers O* **2002**, *74*, S219-S224.

(32) Assion, A.; Baumert, T.; Bergt, M.; Brixner, T.; Kiefer, B.; Seyfried, V.; Strehle, M.; Gerber, G. *Science* **1998**, *282*, 919-922.

(33) Bergt, M.; Brixner, T.; Kiefer, B.; Strehle, M.; Gerber, G. *J. Phys. Chem. A* **1999**, *103*, 10381-10387.

(34) Glass, A.; Rozgonyi, T.; Feurer, T.; Sauerbrey, R.; Szabo, G. *Appl. Phys. B-Lasers O* **2000**, *71*, 267-276.

(35) Daniel, C.; Full, J.; Gonzales, L.; Kaposta, C.; Krenz, M.; Lupulescu, C.; Manz, J.; Minemoto, S.; Oppel, M.; Rosendo-Francisco, P.; Vajda, S.; Woste, L. *Chem. Phys.* **2001**, *267*, 247-260.

(36) Brixner, T.; Kiefer, B.; Gerber, G. *Chem. Phys.* **2001**, *267*, 241-246.

(37) Levis, R. J.; Menkir, G. M.; Rabitz, H. *Science* **2001**, *292*, 709-713.

(38) Levis, R. J.; Rabitz, H. A. *J. Phys. Chem. A* **2002**, *106*, 6427-6444.

(39) Damrauer, N. H.; Dietl, C.; Krampert, G.; Lee, S. H.; Jung, K. H.; Gerber, G. *Eur. Phys. J. D* **2002**, *20*, 71-76.

(40) Bergt, M.; Brixner, T.; Dietl, C.; Kiefer, B.; Gerber, G. *J. Organomet. Chem.* **2002**, *661*, 199-209.

(41) Daniel, C.; Full, J.; Gonzalez, L.; Lupulescu, C.; Manz, J.; Merli, A.; Vajda, S.; Woste, L. *Science* **2003**, *299*, 536-539.

(42) Hornung, T.; Meier, R.; Zeidler, D.; Kompa, K. L.; Proch, D.; Motzkus, M. *Appl. Phys. B-Lasers O* **2000**, *71*, 277-284.

(43) Zeidler, D.; Frey, S.; Kompa, K. L.; Motzkus, M. *Phys. Rev. A* **2001**, *64*, Art. No. 023420.

(44) Ando, T.; Urakami, T.; Itoh, H.; Tsuchiya, Y. *Appl. Phys. Lett.* **2002**, *80*, 4265-4267.

(45) Brixner, T.; Damrauer, N. H.; Niklaus, P.; Gerber, G. *Nature* **2001**, *414*, 57-60.

(46) Brixner, T.; Damrauer, N. H.; Krampert, G.; Niklaus, P.; Gerber, G. *J. Opt. Soc. Am. B* **2003**, *20*, 878-881.

(47) Weinacht, T. C.; White, J. L.; Buckbaum, P. H. *J. Phys. Chem. A* **1999**, *103*, 10166-10168.

(48) Weinacht, T. C.; Bartels, R.; Backus, S.; Buckbaum, P. H.; Pearson, B. J.; Geremia, J. M.; Rabitz, H.; Kapteyn, H. C.; Murnane, M. M. *Chem. Phys. Lett.* **2001**, *344*, 333-338.

(49) Bartels, R. A.; Weinacht, T. C.; Leone, S. R.; Kapteyn, H. C.; Murnane, M. M. *Phys. Rev. Lett.* **2002**, *88*, Art. No. 033001.

(50) Zeidler, D.; Frey, S.; Wohlleben, W.; Motzkus, M.; Busch, F.; Chen, T.; Kiefer, W.; Materny, A. *J. Chem. Phys.* **2002**, *116*, 5231-5235.

(51) Herek, J. L.; Wohlleben, W.; Cogdell, R. J.; Zeidler, D.; Motzkus, M. *Nature* **2002**, *417*, 533-535.

(52) Bartels, R.; Backus, S.; Zeek, E.; Misoquti, L.; Vdovin, G.; Christov, I. P.; Murnane, M. M.; Kapteyn, H. C. *Nature* **2000**, *406*, 164-166.

(53) Vajda, S.; Bartelt, A.; Kaposta, E. C.; Leisner, T.; Lupulescu, C.; Minemoto, S.; Rosendo-Francisco, P.; Woste, L. *Chem. Phys.* **2001**, *267*, 231-239.

(54) Schafer-Bung, B.; Mitric, R.; Bonacic-Koutecky, V.; Bartelt, A.; Lupulescu, C.; Lindinger, A.; Vajda, S.; Weber, S. M.; Woste, L. *J. Phys. Chem. A* **2004**, *108*, 4175-4179.

(55) Pearson, B. J.; White, J. L.; Weinacht, T. C.; Buckbaum, P. H. *Phys. Rev. A* **2001**, *63*, Art. No. 063412.

(56) Omenetto, F. G.; Taylor, A. J.; Moores, M. D.; Reitze, D. H. *Opt. Lett.* **2001**, *26*, 938-940.

(57) Kunde, J.; Baumann, B.; Arlt, S.; Morier-Genoud, F.; Siegner, U.; Keller, U. *Appl. Phys. Lett.* **2000**, *77*, 924-926.

(58) Hornung, T.; Meier, R.; de Vivie-Riedle, R.; Motzkus, M. *Chem. Phys.* **2001**, *267*, 261-276.

(59) Meshulach, D.; Silberberg, Y. *Nature* **1998**, *396*, 239-242.

(60) Meshulach, D.; Silberberg, Y. *Phys. Rev. A* **1999**, *60*, 1287-1292.

(61) Buist, A. H.; Muller, M.; Ghauharali, R. I.; Brakenhoff, G. J.; Squier, J. A.; Bardeen, C. J.; Yakovlev, V. V.; Wilson, K. R. *Opt. Lett.* **1999**, *24*, 244-246.

(62) Dudovich, N.; Dayan, B.; Feaeder, S. M. G.; Silberberg, Y. *Phys. Rev. Lett.* **2001**, *86*, 47-50.

(63) Dudovich, N.; Oron, D.; Silberberg, Y. *Phys. Rev. Lett.* **2002**, *88*, Art. No. 123004.

(64) Ballard, J. B.; Stauffer, H. U.; Amitay, Z.; Leone, S. R. *J. Chem. Phys.* **2002**, *116*, 1350-1360.

(65) Walowicz, K. A.; Pastirk, I.; Lozovoy, V. V.; Dantus, M. *J. Phys. Chem. A* **2002**, *106*, 9369-9373.

(66) Lozovoy, V. V.; Pastirk, I.; Walowicz, K. A.; Dantus, M. *J. Chem. Phys.* **2003**, *118*, 3187-3196.

(67) Bardeen, C. J.; Shank, C. V. *Chem. Phys. Lett.* **1993**, *203*, 535-539.

(68) Antoine, P.; LHuillier, A.; Lewenstein, M. *Phys. Rev. Lett.* **1996**, *77*, 1234-1237.

(69) Antoine, P.; Milosevic, D. B.; LHuillier, A.; Gaarde, M. B.; Salieres, P.; Lewenstein, M. *Phys. Rev. A* **1997**, *56*, 4960-4969.

(70) Agostini, P.; DiMauro, L. F. *Rep. Prog. Phys.* **2004**, *67*, 813-855.

(71) Trebino, R.; Kane, D. J. *J. Opt. Soc. Am. A* **1993**, *10*, 1101-1111.

(72) Trebino, R.; DeLong, K. W.; Fittinghoff, D. N.; Sweetser, J. N.; Krumbugel, M. A.; Richman, B. A.; Kane, D. J. *Rev. Sci. Instrum.* **1997**, *68*, 3277-3295.

(73) Iaconis, C.; Walmsley, I. A. *Opt. Lett.* **1998**, *23*, 792-794.

(74) Iaconis, C.; Walmsley, I. A. *IEEE J. Quantum Elect.* **1999**, *35*, 501-509.

(75) Siegner, U.; Haiml, M.; Kunde, J.; Keller, U. *Opt. Lett.* **2002**, *27*, 315-317.

(76) Monmayrant, A.; Joffre, M.; Oksenhendler, T.; Herzog, R.; Kaplan, D.; Tournois, P. *Opt. Lett.* **2003**, *28*, 278-280.

(77) Comstock, M.; Lozovoy, V. V.; Pastirk, I.; Dantus, M. *Opt. Express* **2004**, *12*, 1061-1066.

(78) Rabitz, H. A.; Hsieh, M. M.; Rosenthal, C. M. *Science* **2004**, *303*, 1998-2001.

(79) Moulton, P. F. *J. Opt. Soc. Am. B* **1986**, *3*, 125-133.

(80) Sanchez, A.; Fahey, R. E.; Strauss, A. J.; Aggarwal, R. L. *Opt. Lett.* **1986**, *11*, 363-364.

(81) Kuizenga, D. J.; Siegman, A. E. *IEEE J. Quantum Elect.* **1970**, *6*, 694-698.

(82) Spence, D. E.; Evans, J. M.; Sleat, W. E.; Sibbett, W. *Opt. Lett.* **1991**, *16*, 1762-1764.

(83) Asaki, M. T.; Huang, C. P.; Garvey, D.; Zhou, J. P.; Kapteyn, H. C.; Murnane, M. M. *Opt. Lett.* **1993**, *18*, 977-979.

(84) Spielmann, C.; Curley, P. F.; Brabec, T.; Krausz, F. *IEEE J. Quantum Elect.* **1994**, *30*, 2431-2431.

(85) Backus, S.; Peatross, J.; Huang, C. P.; Murnane, M. M.; Kapteyn, H. C. *Opt. Lett.* **1995**, *20*, 2000-2002.

(86) Maine, P.; Strickland, D.; Bado, P.; Pessot, M.; Mourou, G. *IEEE J. Quantum Elect.* **1988**, *24*, 398-403.

(87) Backus, S.; Durfee, C. G.; Murnane, M. M.; Kapteyn, H. C. *Rev. Sci. Instrum.* **1998**, *69*, 1207-1223.

(88) Heritage, J. P.; Weiner, A. M.; Thurston, R. N. *Opt. Lett.* **1985**, *10*, 609-611.

(89) Wefers, M. M.; Nelson, K. A. *Opt. Lett.* **1993**, *18*, 2032-2034.

(90) Weiner, A. M. *Rev. Sci. Instrum.* **2000**, *71*, 1929-1960.

(91) Dantus, M.; Lozovoy, V. V. *Chem. Rev.* **2004**, *104*, 1813-1860.

(92) Denk, W.; Strickler, J. H.; Webb, W. W. *Science* **1990**, *248*, 73-76.

(93) Cerullo, G.; Bardeen, C. J.; Wang, Q.; Shank, C. V. *Chem. Phys. Lett.* **1996**, *262*, 362-368.

(94) Bardeen, C. J.; Yakovlev, V. V.; Squier, J. A.; Wilson, K. R. *J. Am. Chem. Soc.* **1998**, *120*, 13023-13027.

(95) Rice, S. A. *Nature* **2001**, *409*, 422-426.

(96) Bardeen, C. J.; Rosenthal, S. J.; Shank, C. V. *J. Phys. Chem. A* **1999**, *103*, 10506-10516.

(97) Lozovoy, V. V.; Pastirk, I.; Dantus, M. *Opt. Lett.* **2004**, *29*, 775-777.

(98) Wolfbeis, O. S.; Furlinger, E.; Kroneis, H.; Marsoner, H. *Fresenius Z. Anal. Chem.* **1983**, *314*, 119-124.

(99) Tran-Thi, T. H.; Gustavsson, T.; Prayer, C.; Pommeret, S.; Hynes, J. T. *Chem. Phys. Lett.* **2000**, *329*, 421-430.

(100) Tran-Thi, T. H.; Prayer, C.; Millie, P.; Uznanski, P.; Hynes, J. T. *J. Phys. Chem. A* **2002**, *106*, 2244-2255.

(101) Schulman, S. G.; Vincent, W. R.; Underberg, W. J. M. *J. Phys. Chem. A* **1981**, *85*, 4068-4071.

(102) Haugland, R. P.; Johnson, I. P. In *Fluorescent and Luminescent Probes,* 2nd ed.; Mason, W. T., Ed.; Academic Press, 1999, pp 647.

(103) Putnam, R. W. In *Cell Physiology Source Book,* 2nd ed.; Sperelakis, N., Ed.; Academic Press, 1996, pp 738.

(104) Konig, K. *J. Microsc. - Oxford* **2000**, *200*, 83-104, Part 102.

(105) So, P. T. C.; Dong, C. Y.; Masters, B. R.; Berland, K. M. *Annu. Rev. Biomed. Eng.* **2000**, *2*, 399-429.

(106) Dunn, K. W.; Sandoval, R. M.; Kelly, K. J.; Dagher, P. C.; Tanner, G. A.; Atkinson, S. J.; Bacallao, R. L.; Molitoris, B. A. *Am. J. Physiol. -Cell Ph.* **2002**, *283*, C905-C916.

(107) Wang, J. W.; Wong, A. M.; Flores, J.; Vosshall, L. B.; Axel, R. *Cell* **2003**, *112*, 271-282.

(108) Oertner, T. G. *Exp. Physiol.* **2002**, *87*.

(109) Kasischke, K. A.; Vishwasrao, H.; Heikal, A. A.; Webb, W. W. *Biophys. J.* **2002**, *82*, 495A-495A 2420 Part 2422.

(110) Rose, C. R.; Kovalchuk, Y.; Eilers, J.; Konnerth, A. *Pflug. Arch. Eur. J. Phy.* **1999**, *439*, 201-207.

(111) Dela Cruz, J. M.; Pastirk, I.; Lozovoy, V. V.; Walowicz, K. A.; Dantus, M. *J. Phys. Chem. A* **2004**, *108*, 53-58.

(112) *C540 is 3-(2'-Benzothiazoyl)-7-diethylaminocoumarin. R6G is a mixture of rhodamine 590 (2-[6-(ethylamino)-3-(ethylimino)-2,7-dimethyl-3H-xanthen-9-yl]-ethylester, monohydrochloride), DOCI (3,3'-Diethyloxacarbocyanine Iodide) and DCM (4-Dicyanmethylene-2-methyl-6-(p-dimethylaminostyryl)-4H-pyran).*

(113) Wolleschensky, R.; Feurer, T.; Sauerbrey, R.; Simon, I. *Appl. Phys. B-Lasers O* **1998**, *67*, 87-94.

(114) Berns, M. W.; Wang, Z.; Dunn, A.; Wallace, V.; Venugopalan, V. *Proc. Natl. Acad. Sci. USA* **2000**, *97*, 9504-9507.

(115) Shafirovich, V.; Dourandin, A.; Luneva, N. P.; Singh, C.; Kirigin, F.; Geacintov, N. E. *Photochem. Photobiol.* **1999**, *69*, 265-274.

(116) Ogilvie, J. P.; Debarre, D.; Solinas, X.; Martin, J.; Beaurepaire, E.; Joffre, M. *Opt. Express* **2006**, *14*, 759-766.

(117) Larson, D. R.; Zipfel, W. R.; Williams, R. M.; Clark, S. W.; Bruchez, M. P.; Wise, F. W.; Webb, W. W. *Science* **2003**, *300*, 1434-1436.

(118) VandenBout, D. A.; Yip, W. T.; Hu, D. H.; Fu, D. K.; Swager, T. M.; Barbara, P. F. *Science* **1997**, *277*, 1074-1077.

(119) Xu, C.; Denk, W. *Appl. Phys. Lett.* **1997**, *71*, 2578-2580.

(120) Osborn, D. L.; Leone, S. R. *J. Appl. Phys.* **2001**, *89*, 626-633.

(121) Maiti, S.; Shear, J. B.; Williams, R. M.; Zipfel, W. R.; Webb, W. W. *Science* **1997**, *275*, 530-532.

(122) Yelin, D.; Oron, D.; Korkotian, E.; Segal, M.; Silberberg, Y. *Appl. Phys. B-Lasers O* **2002**, *74*, S97-S101.

(123) Watanabe, T.; Akiyama, M.; Totani, K.; Kuebler, S. M.; Stellacci, F.; Wenseleers, W.; Braun, K.; Marder, S. R.; Perry, J. W. *Adv. Funct. Mat.* **2002**, *12*, 611-614.

(124) Dyba, M.; Hell, S. W. *Phys. Rev. Lett.* **2002**, *88*, Art. No. 163901.

(125) Huang, D.; Swanson, E. A.; Lin, C. P.; Schuman, J. S.; Stinson, W. G.; Chang, W.; Hee, M. R.; Flotte, T.; Gregory, K.; Puliafito, C. A.; Fujimoto, J. G. *Science* **1991**, *254*, 1178-1181.

(126) Zare, R. N. *Science* **1998**, *279*, 1875-1879.

(127) Gordon, R. J.; Rice, S. A. *Annu. Rev. Phys. Chem.* **1997**, *48*, 601-641.

(128) Rice, S. A.; Shah, S. P. *Phys. Chem. Chem. Phys.* **2002**, *4*, 1683-1700.

(129) Rabitz, H. *Science* **2003**, *299*, 525-527.

(130) Denk, W. *J. Biomed. Opt.* **1996**, *1*, 296-304.

(131) Fisher, W. G.; Partridge, W. P.; Dees, C.; Wachter, E. A. *Photochem. Photobiol.* **1997**, *66*, 141-155.

(132) Jasapara, J.; Rudolph, W. *Opt. Lett.* **1999**, *24*, 777-779.

(133) Amat-Roldan, I.; Cormack, I. G.; Loza-Alvarez, P.; Artigas, D. *Opt. Lett.* **2004**, *29*, 2282-2284.

(134) Fittinghoff, D. N.; Millard, A. C.; Squier, J. A.; Muller, M. *IEEE J. Quantum Elect.* **1999**, *35*, 479-486.

(135) Muller, M.; Squier, J. A.; Wolleschensky, R.; Simon, U.; Brakenhoff, G. J. *J. Microsc. - Oxford* **1998**, *191*, 141-150.

(136) Fittinghoff, D. N.; Squier, J. A.; Barty, C. P. J.; Sweetser, J. N.; Trebino, R.; Muller, M. *Opt. Lett.* **1998**, *23*, 1046-1048.

(137) Dela Cruz, J. M.; Lozovoy, V. V.; Dantus, M. *J. Photochem. Photobiol. A,* **2006** *180,* 307-313.

(138) Lozovoy, V. V.; Dantus, M. *ChemPhysChem* **2005**, *6*, 1970-2000.

(139) Weinacht, T. C.; Buckbaum, P. H. *J. Opt. B-Quantum S. O.* **2002**, *4*, R35-R52.

(140) Pastirk, I.; Dela Cruz, J. M.; Walowicz, K. A.; Lozovoy, V. V.; Dantus, M. *Opt. Express* **2003**, *11*, 1695-1701.

(141) Yoo, K. M.; Alfano, R. R. *Opt. Lett.* **1990**, *15*, 320-322.

(142) Hee, M. T.; Izatt, J. A.; Jacobson, J. M.; Fujimoto, J. G.; Swanson, E. A. *Opt. Lett.* **1993**, *18*, 950-952.

(143) Parys, B.; Allard, J. F.; Desmullier, F.; Houde, D.; Cornet, A. *J. Opt. A-Pure Appl. Op.* **2004**, *6*, L23-L27.

(144) Beaurepaire, E.; Oheim, M.; Mertz, J. *Opt. Commun.* **2001**, *188*, 25-29.

(145) Theer, P.; Hasan, M. T.; Denk, W. *Opt. Lett.* **2003**, *28*, 1022-1024.

(146) Koester, H. J.; Baur, D.; Uhl, R.; Hell, S. W. *Biophys. J.* **1999**, *77*, 2226-2236.

(147) Hopt, A.; Neher, E. *Biophys. J.* **2001**, *80*, 2029-2036.

(148) Szmacinski, H.; Gryczynski, I.; Lakowicz, J. R. *Biospectroscopy* **1998**, *4*, 303-310.

(149) Konig, K.; So, P. T. C.; Mantulin, W. W.; Gratton, E. *Opt. Lett.* **1997**, *22*, 135-136.

(150) Cunningham, M. L.; Johnson, J. S.; Giovanazzi, S. M.; Peak, M. J. *Photochem. Photobiol.* **1985**, *42*, 125-128.

(151) Kilic, H. S.; Ledingham, K. W. D.; Kosmidis, C.; McCanny, T.; Singhal, R. P.; Wang, S. L.; Smith, D. J.; Langley, A. J.; Shaikh, W. *J. Phys. Chem. A* **1997**, *101*, 817-823.

(152) Szaflarski, D. M.; ElSayed, M. A. *J. Phys. Chem.* **1988**, *92*, 2234-2239.

(153) *In most 70 eV EI experiments,approximately 1400 kJ/mole (15 eV) of energy is transferred duringthe ionization process.There is, however, a distribution of energy and as much as 2800 kJ/mole (30 eV) is transferred to some molecules. Since approximately 960 kJ/mole (10 eV) is required to ionize most organic compounds and a typical chemical bond energy is 290 kJ/mole (3 eV), extensive fragmentation is often observed in 70 eV EI mass spectra.*

(154) Harless, R. L.; Oswald, E. O.; Wilkinson, M. K.; Dupuy, A. E.; McDaniel, D. D.; Tai, H. *Anal. Chem.* **1980**, *52*, 1239-1245.

(155) Hawthorne, S. B.; Langenfeld, J. J.; Miller, D. J.; Burford, M. D. *Anal. Chem.* **1992**, *64*, 1614-1622.

(156) Axelson, M.; Sahlberg, B. L.; Sjovall, J. *J. Chromatogr.* **1981**, *224*, 355-370.

(157) Burlingame, A. L.; Shackleton, C. H. L.; Howe, I.; Chizhov, O. S. *Anal. Chem.* **1978**, *50*, R346-R384.

(158) Allison, J.; Holland, J. F.; Enke, C. G.; Watson, J. T. *Anal. Instrum.* **1987**, *16*, 207-224.

(159) Bruckner, C. A.; Prazen, B. J.; Synovec, R. E. *Anal. Chem.* **1998**, *70*, 2796-2804.

(160) Wu, H. F.; Chuan, Y. J. *Rapid Commun. Mass Sp.* **2003**, *17*, 1030-1036.

(161) Wu, H. F.; Wu, W. F. *Rapid Commun. Mass Sp.* **2003**, *17*, 2399-2406.

(162) Kascheres, C.; Cooks, R. G. *Anal. Chimica Acta* **2002**, *215*, 223-232.

(163) Zimmermann, R.; Lerner, C.; Schramm, K.; Kettrup, A.; Boesl, U. *Eur. J. Mass Spectrom.* **1995**, *1*, 341-351.

(164) Brodbelt, J. S.; Liou, C. C.; Donovan, T. *Anal. Chem.* **1991**, *63*, 1205-1209.

(165) Bjarnason, A. *Anal. Chem.* **1996**, *68*, 3882-3883.

(166) Dantus, M.; Jannsen, M. H. M.; Zewail, A. H. *Chem. Phys. Lett.* **1991**, *181*, 281-287.

(167) Baumert, T.; Buhler, B.; Thalweiser, R.; Gerber, G. *Phys. Rev. Lett.* **1990**, *64*, 733-736.

(168) Cardoza, D.; Baertschy, M.; Weinacht, T. C. *Chem. Phys. Lett.* **2005**, *411*, 311-315.

(169) Pastirk, I.; Kangas, M.; Dantus, M. *J. Phys. Chem. A* **2005**, *109*, 2413-2416.

(170) Xu, B.; Gunn, J. M.; Dela Cruz, J. M.; Lozovoy, V. V.; Dantus, M. *J. Opt. Soc. Am. B* **2006**, *23*, 750-759.

(171) Stein, S. E.; NIST Mass Spec Data Center In *NIST Chemistry Web Book, NIST Standard Reference Database Number 69*; Linstrom, P. J., Mallard, W. G., Eds.; National Institute of Standards and Technology: Gaithersburg, MD, 2005.

(172) Malow, M.; Penno, M.; Weitzel, K. M. *J. Phys. Chem. A* **2003**, *107*, 10625-10630.

(173) Gedanken, A.; Robin, M. B.; Kuebler, N. A. *J. Phys. Chem.* **1982**, *86*, 4096-4107.

(174) Yang, J. J.; Gobeli, D. A.; ElSayed, M. A. *J. Phys. Chem.* **1985**, *89*, 3426-3429.

(175) Meek, J. T.; Jones, R. K.; Reilly, J. P. *J. Chem. Phys.* **1980**, *73*, 3503-3505.

(176) Zandee, L.; Bernstein, R. B. *J. Chem. Phys.* **1979**, *70*, 2574-2575.

(177) Rockwood, S.; Reilly, J. P.; Hohla, K.; Kompa, K. L. *Opt. Commun.* **1979**, *28*, 175-178.

(178) Fisanick, G. J.; Eichelberger, T. S.; Heath, B. A.; Robin, M. B. *J. Chem. Phys.* **1980**, *72*, 5571-5580.

(179) Robin, M. B. *Appl. Opt.* **1980**, *19*, 3941-3947.

(180) Kosmidis, C.; Ledingham, K. W. D.; Kilic, H. S.; McCanny, T.; Singhal, R. P.; Langley, A. J.; Shaikh, W. *J. Phys. Chem. A* **1997**, *101*, 2265-2270.

(181) Lezius, M.; Blanchet, V.; Ivanov, M. Y.; Stolow, A. *J. Chem. Phys.* **2002**, *117*, 1575-1588.

(182) Smith, S. M.; Markevitch, A. N.; Romanov, D. A.; Li, X. S.; Levis, R. J.; Schlegel, H. B. *J. Phys. Chem. A* **2004**, *108*, 11063-11072.

(183) Pirkle, W. H.; Pochapsky, T. C.; Giddings, J. C., Grushka, E., Brown, P. R., Eds.; Marcel Dekker, Inc.: New York, 1987; Vol. 27, pp 73-127.

(184) Taylor, D. R.; Maher, K. *J. Chromatogr. Sci.* **1992**, *30*, 67-85.

(185) Gubitz, G. *Chromatographia* **1990**, *30*, 555-564.

(186) Holland, L. A.; Chetwyn, N. P.; Perkins, M. D.; Lunte, S. M. *Pharm. Res.* **1997**, *14*.

(187) Altria, K. D.; Elgey, J.; Lockwood, P.; Moore, D. *Chromatographia* **1996**, *42*, 332-342.

(188) Rieutord, A.; Prognon, P.; Mahuzier, G. *Analusis* **1996**, *24*, 349-360.

(189) Le Bel, J. A. *Bull. Soc. Chim. France* **1874**, *22*, 337.

(190) Van't Hoff, J. H. *Die Lagerung der Atome im Raume*, 2nd ed.; Vieweg: Braunschweig, 1894.

(191) Rau, H. *Chem. Rev.* **1983**, *83*, 535-547.

(192) Inoue, Y. *Chem. Rev.* **1992**, *92*, 741-770.

(193) Mitchell, S. *J. Chem. Soc.* **1930**, *Part 2*, 1829-1834.

(194) Mitchell, S.; Dawson, I. M. *J. Chem. Soc.* **1944**, *Part 2*, 452-454.

(195) Stevenso.K.L.; Verdieck, J. F. *J. Am. Chem. Soc.* **1968**, *90*, 2974-2978.

(196) Nicoud, J. F.; Kagan, H. B. *Israel J. Chem.* **1977**, *15*, 78-81.

(197) Ward, R. S. *Tetrahedron-Asymmetr.* **1995**, *6*, 1475-1490.

(198) Balavoin, G.; Moradpou, A.; Kagan, H. B. *J. Am. Chem. Soc.* **1974**, *96*, 5152-5158.

(199) Brixner, T.; Gerber, G. *Opt. Lett.* **2001**, *26*, 557-559.

(200) Brixner, T.; Krampert, G.; Niklaus, P.; Gerber, G. *Appl. Phys. B-Lasers O* **2002**, *74*, S133-S144.

(201) Polachek, L.; Oron, D.; Silberberg, Y. *Opt. Lett.* **2006**, *31*, 631-633.

(202) Shapiro, M.; Brumer, P. *J. Chem. Phys.* **1991**, *95*, 8658-8661.

(203) Shapiro, M.; Frishman, E.; Brumer, P. *Phys. Rev. Lett.* **2000**, *84*, 1669-1672.

(204) Gerbasi, D.; Shapiro, M.; Brumer, P. *J. Chem. Phys.* **2001**, *115*, 5349-5352.

(205) Salam, A.; Meath, W. J. *J. Chem. Phys.* **1997**, *106*, 7865-7868.

(206) Salam, A.; Meath, W. J. *Chem. Phys.* **1998**, *228*, 115-129.

(207) Asaro, C.; Brumer, P.; Shapiro, M. *Phys. Rev. Lett.* **1988**, *60*, 1634-1637.

(208) Fujimura, Y.; Gonzales, L.; Hoki, K.; Manz, J.; Ohtsuki, Y. *Chem. Phys. Lett.* **1999**, *310*.

(209) Gonzalez, L.; Hoki, K.; Kroner, D.; Leal, A. S.; Manz, J.; Ohtsuki, Y. *J. Chem. Phys.* **2000**, *113*, 11134-11142.

(210) Kroner, D.; Shibl, M. F.; Gonzales, L. *Chem. Phys. Lett.* **2003**, *372*, 242-248.

(211) Kroner, D.; Gonzales, L. *Chem. Phys. Lett.* **2004**, *298*, 55-63.

(212) Wefers, M. M.; Nelson, K. A. *J. Opt. Soc. Am. B* **1995**, *12*, 1343-1362.

(213) Brixner, T.; Krampert, G.; Pfeifer, T.; Selle, R.; Gerber, G.; Wollenhaupt, M.; Graefe, O.; Horn, C.; Liese, D.; Baumert, T. *Phys. Rev. Lett.* **2004**, *92*, Art. No. 208301.

(214) Nelson, R. D.; Leaird, D. E.; Weiner, A. M. *Opt. Express* **2003**, *11*, 1763-1769.

(215) Oron, D.; Dudovich, N.; Silberberg, Y. *Phys. Rev. Lett.* **2003**, *90*, Art. No. 213902.

(216) Krishnamurthy, M.; Mathur, D. *Phys. Rev. A* **2000**, *61*, Art. No. 063404.

(217) Nikogosyan, D. N.; Repeyev, Y. A.; Khoroshilova, E. V.; Kryukov, I. V.; Khoroshilov, E. V.; Sharkov, A. V. *Chem. Phys.* **1990**, *147*, 437-445.

(218) Fork, R. L.; Martinez, O. E.; Gordon, J. P. *Opt. Lett.* **1984**, *9*, 150-152.

(219) Stingl, A.; Spielmann, C.; Krausz, F.; Szipocs, R. *Opt. Lett.* **1994**, *19*, 204-206.

(220) Szipocs, R.; Ferencz, K.; Spielmann, C.; Krausz, F. *Opt. Lett.* **1994**, *19*, 201-203.

(221) Nisoli, M.; DeSilvestri, S.; Svelto, O.; Szipocs, R.; Ferencz, K.; Spielmann, C.; Sartania, S.; Krausz, F. *Opt. Lett.* **1997**, *22*, 522-524.